AD-A228 690

The Control of Human Arm Movement: Models and Mechanical Constraints

DTIC
ELECTE
NOV 06 1990
S E D

David J. Bennett

MIT Artificial Intelligence Laboratory

4

REPORT DOCUMENTATION PAGE		READ INSTRUCTIONS BEFORE COMPLETING FORM
1. REPORT NUMBER AI-TR 1234	2. GOVT ACCESSION NO	3. RECIPIENT'S CATALOG NUMBER
4. TITLE (and Subtitle) The Control of Human Arm Movement: Models and Mechanical Constraints		5. TYPE OF REPORT & PERIOD COVERED technical report
		6. PERFORMING ORG. REPORT NUMBER
7. AUTHOR(s) David J. Bennett		8. CONTRACT OR GRANT NUMBER(s) N00014-86-K-0180 N00014-85-K-0124
9. PERFORMING ORGANIZATION NAME AND ADDRESS Artificial Intelligence Laboratory 545 Technology Square Cambridge, MA 02139		10. PROGRAM ELEMENT PROJECT, TASK AREA & WORK UNIT NUMBERS
11. CONTROLLING OFFICE NAME AND ADDRESS Advanced Research Projects Agency 1400 Wilson Blvd. Arlington, VA 22209		12. REPORT DATE June 1990
		13. NUMBER OF PAGES 201
14. MONITORING AGENCY NAME & ADDRESS(If different from Controlling Office) Office of Naval Research Information Systems Arlington, VA 22217		15. SECURITY CLASS. (of this report) UNCLASSIFIED
		15a. DECLASSIFICATION/DOWNGRADING SCHEDULE

16. DISTRIBUTION STATEMENT (of this Report)

Distribution is unlimited

17. DISTRIBUTION STATEMENT (of the abstract entered in Block 20, if different from Report)

DTIC
ELECTE
NOV 06 1990
S E D

18. SUPPLEMENTARY NOTES

None

19. KEY WORDS (Continue on reverse side if necessary and identify by block number)

kinematic calibration	human motor control
closed-loop constraints	dynamics
model-based learning	compliance control

20. ABSTRACT (Continue on reverse side if necessary and identify by block number)

The first part of this thesis investigates the role of structured models in autonomous motor learning. Any autonomous system, such as the human motor system, has only the internal consistency of its various sensors to rely upon for model building (learning). To study the possibility of learning structured models from internal consistency constraints, the specific problem of learning the kinematic parameters (relative link
(con't on back)

(block 20 con't)

orientations and lengths) of general revolute joint manipulators is explored. First it is noted that a manipulator may form a mobile closed kinematic chain when interacting with the env' ·onment, if it is redundant with respect to the task degrees of freedom (DOFs) at the endpoint. Then it is demonstrated that if the mobile closed chain assumes a number of configurations, then loop consistency equations permit the manipulator and task kinematics to be calibrated simultaneously using only the joint angle readings; endpoint sensing is not required. Example tasks include a fixed endpoint (0 DOF task), the opening of a door (1 DOF task), and a point contact (3 DOF task). Identifiability conditions are derived for these various tasks. The method is demonstrated for calibration of the Utah-MIT Dextrous Hand, and is generalized to hand-eye-calibration.

Part two focuses on the control of mechanical compliance during normal human elbow joint movement. In contrast to the first half of the thesis, this part stresses the experimental validation, rather than the formation, of control theories. Time-varying compliance estimates are made while subjects are executing normal movement. The estimates are made possible by the development of (1) a high performance wrist-mounted airjet thruster and (2) novel time-varying system identification techniques. The results indicate that the stiffness of the arm is low and is modulated during movement. The stiffness drops as soon as the movement starts and rises just before reaching a target. The implications of this and other findings are discussed in the context of feedforward control, compliance control, and equilibrium point control theories. Physiological mechanisms for stiffness modulation are also discussed.

The Control of Human Arm Movement:

Models and Mechanical Constraints

by

David J. Bennett

Abstract

The first part of this thesis investigates the role of structured models in autonomous motor learning. Any autonomous system, such as the human motor system, has only the internal consistency of its various sensors to rely upon for model building (learning). To study the possibility of learning structured models from internal consistency constraints, the specific problem of learning the kinematic parameters (relative link orientations and lengths) of general revolute joint manipulators is explored. First it is noted that a manipulator may form a mobile closed kinematic chain when interacting with the environment, if it is redundant with respect to the task degrees of freedom (DOFs) at the endpoint. Then it is demonstrated that if the mobile closed chain assumes a number of configurations, then loop consistency equations permit the manipulator and task kinematics to be calibrated simultaneously using only the joint angle readings; endpoint sensing is not required. Example tasks include a fixed endpoint (0 DOF task), the opening of a door (I DOF task), and a point contact (3 DOF task). Identifiability conditions are derived for these various tasks. The method is demonstrated for calibration of the Utah-MIT Dextrous Hand, and is generalized to hand-eye calibration.

Part two focuses on the control of mechanical compliance during normal human elbow joint movement. In contrast to the first half of the thesis, this part stresses the experimental validation, rather than the formation, of control theories. Time-varying compliance estimates are made while subjects are executing normal movement. The estimates are made possible by the development of (1) a high performance wrist-mounted airjet thruster and (2) novel time-varying system identification techniques. The results indicate that the stiffness of the arm is low and is modulated during movement. The stiffness drops as soon as the movement starts and rises just before reaching a target. The implications of this and other findings are discussed in the context of feedforward control, compliance control, and equilibrium point control theories. Physiological mechanisms for stiffness modulation are also discussed.

Thesis Supervisor: Professor John M. Hollerbach

Acknowledgments

I wish to thank the many people who have helped me along the way.

4

Contents

Chapter 1

Introduction

The goal of this research is to understand the control of human arm movement. The view taken is that there are common problems involved in controlling any general purpose arm, whether it is biological or artificial. The intention is to uncover some of these problems, develop general methods for solving them, and infer the particular solutions taken by the human system. Ultimately, such solutions should reflect our motor competence, while adhering to the inherent mechanical and neural constraints.

The investigation focuses on two aspects of the human movement control problem: (1) learning kinematic sensorimotor transformations, and (2) controlling rapid arm movements. The first is investigated by implementing and evaluating calibration methods on robot manipulators. The goal is not so much to determine the details of human calibration, but instead, to gain an appreciation for the difficulties involved, and ultimately to derive appropriate experimental questions for future human studies. The second topic is investigated by experimentally determining the elbow joint mechanical properties during rapid movement. These time-varying mechanical properties are used to assess current theories of arm control.

1.1 Background and Significance

The control of arm movements is a deceptively difficult problem. Over the years researchers have come up with various ideas that are likely to be relevant to an
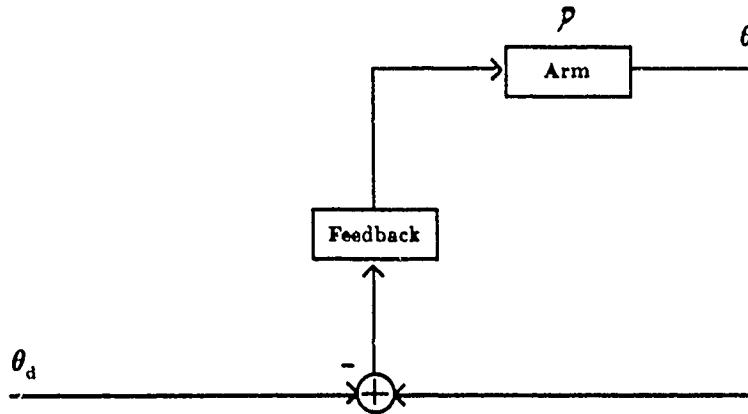
Figure 1-1: Feedback control of a joint angle trajectory θ.

eventual theory of human motor control. A synopsis of some of these ideas provides
a good starting point for the work contained in this thesis. The reader familiar with
the context of this research may skip this section. It is intended to tie together the
two loosely related parts of the thesis, and follows along the lines of [1][2][3].

1.1.1 Feedback Control

Given the complexity of both our motor system and the environment, it is reasonable
to speculate that arm movements are made under strict feedback control (Figure 1-
1). Take the simple task of extending the elbow joint. Muscle spindles, Golgi tendon
organs, and joint receptors all contribute information about the actual trajectory of
the elbow joint. Under linear feedback control the torque applied by muscle activation
is made proportional (by a proportionality factor called the *gain*) to the difference
between the actual and desired arm trajectory. Historically, Merton proposed the
use of feedback control in controlling limb movements; he hypothesized that the
gamma motor neurons are controlled and the main alpha motor neurons are driven
from spindle feedback alone (see review [4]). Subsequent deafferentation studies and
fusimotor neuron recordings proved him wrong, although some form of feedback is
definitely present [4]. Before discussing the alternatives to feedback control, it is worth
considering why feedback control alone cannot suffice to explain human performance.

Any feedback control scheme is by definition *error driven.* Thus, there are two ways to apply a greater force to speed up a movement: (1) tolerate greater errors, and (2) increase the feedback gains.

Errors depend on the control variable

The errors that are tolerated are task specific and depend upon the choice of the control variables. For example, in hammering in a nail the hand paths may be variable, while the impact location must be precisely controlled. In contrast, visually-guided pursuit requires continuous control of the hand trajectory (Sheridan [5] provides a good summary of this literature). Compromises between these two extremes have been observed for difficult pursuit-tracking tasks. For instance, Novas [6] found that when he tricked subjects by partially locking the target position to their hand movements (i.e., a "carrot on a stick" set-up) then movements were made intermittently. Bekey [7] also noticed evidence for discrete movements in pursuit tracking. He speculated that a visually-guided operator may be modeled as a sampled-data control system, sampling at 2-3 Hz (see also Crossman and Goodeve [8]).

Stability, gain and phase

As the loop gain of the feedback system exceeds unity instability may result. For example, consider the effect of the large neuronal propagation delays (spinal feedback delay exceeds 25 ms, and visual feedback delay exceeds 100 ms [9]). For a linear feedback control system pure delays can lead to instability as follows: if a frequency component of the input signal (e.g., desired position) has a period of twice the duration of the pure delay then the feedback will be 180 degrees out of phase – effectively providing positive feedback. Such oscillations will grow if the loop gain at that frequency is greater than one.

Linear stability ideas generalize to non-linear systems such as the motor system. One approach is to generalize the notion of gain (using extended spaces [10]). Stability is guaranteed if the product of the loop "gains" is less than unity (small gains theorem) [10]. Loop transformations make this theorem less conservative. A second approach is to generalize the linear systems result that keeping the open-loop phase shift between ±180 degrees ensures stability [11]. Stability is guaranteed for

14

the closed-loop system if both the forward path (e.g., the manipulator structure) and the reverse path (e.g., the feed-back controller, or the environment) are dissipative (strictly passive) [10]. This passivity theorem explains why simple proportional-plus-derivative feedback control of manipulators works at all (without gravity).

Compliance is important

High feedback gains also compromise the need for compliance. In the event that a manipulator runs into an unexpected object, the more compliant the manipulator is the less likely it is to break the object (or itself). The use of force feedback from the hand can improve the compliance of a high gain position controlled manipulator, but force sensor delays and non-colocated actuators lead to acute stability problems.

In summary, using strict feedback control forces difficult trade-offs: speed, accuracy and high gains versus stability, compliance (low gains), and energy dissipation (re passivity theorem). This is not to say that feedback control is not used by the motor system. On the contrary, reflexes are used, and in fact can be driven to instability (for example, with 8-12 Hz elbow joint perturbations; see Joyce and Rack [12][13]). The point is that the performance humans exhibit should be a result of more than feedback control alone.

1.1.2 Pre-Planned Movements

The problems with feedback control are countered by using pre-programmed (feedforward) movements. See Figure 1-2. This was realized early on with the "motor tape" idea, and has taken on various theoretical forms in robotics [14][15][16][17]. The cost of such an approach is the need for complex internal models. That is, the motor system and the environment must be represented, knowledge of the parameters of this representation must be learned, and appropriate feedforward trajectories must be computed.

Of course, both feedback control and knowledge intensive planning can be combined. One method is to put knowledge of the non-linear arm dynamics into the feedback controller — as in model-referenced adaptive control [18]. Adaptive control has been used to model the details of the vestibular-ocular reflex (VOR) [19] (for a

Figure 1-2: Feedforward control of a joint angle trajectory θ. The feedforward control attempts to invert the arm dynamics $\mathcal{P}$.
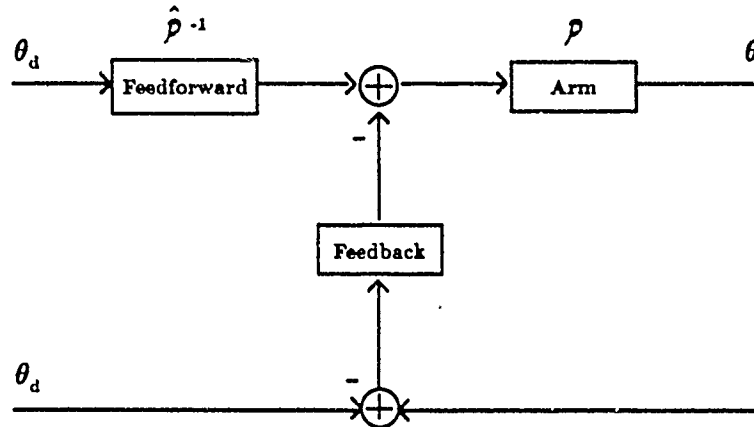
Figure 1-3: Feedforward + feedback control of a joint angle trajectory θ.

review of the various oculomotor control models see [20]). A feedback controller may also be used in cascade with a feedforward controller to reject unmodeled dynamics (e.g., [16]). See Figure 1-3. Owing to the non-linear inertial and gravitational link interactions – even at low speeds [21] – it is probable that some knowledge of the inertial properties of the arm are used for control. In human arm movements there is reason to believe that feedback is only used intermittently — to set-up successive ballistic movements, and avoid instability [8].

1.1.3 Mechanical Constraints Augment Active Control

Another emerging theme in motor control research is an idea mechanical engineers sometimes use: it is advantageous to design a mechanical device such that its uncontrolled passive behavior is close to the desired behavior. For example, consider McGeer's [22] passive walking machine. Inspired by a child's toy, McGeer noticed

16

that walking resembles the movement of a wheel, and thus designed a 2-legged device that emulates a wheel. Of course, actuators were needed to make the machine more versatile, but these actuators augmented, rather than ignored, the inherently stable passive walking behavior of the machine. In a similar manner, evolution of the the human motor system may have simplified the required control effort with mechanical design.

In motor control and robotics numerous mechanical simplifications have been noticed: the human's spherical wrist and shoulder joints allow potentially simple closed form inverse kinematic solutions [1]; the redundant arm geometry aids in singularity avoidance [23]; the use of contact friction helps in manipulation [24]; symmetry can simplify legged locomotion [25]; and finally, the mechanical properties of the muscles provide passive feedback control [8][26][27][28].

1.2   Scope of Thesis

The thesis concentrates on two specific problems, through which the above control issues are investigated. The first is the control of statically positioning the hand in space without visual guidance. This kinematic task is the most clear example of the use of feedforward control in the motor system. There must be some internal model (kinematic transformation) that maps hand locations into joint angles (or muscle lengths). A major issue and the focus of this thesis is the representation and learning of this kinematic transformation.

The investigation of kinematic learning is organized as follows: Chapter 2 discusses the problem constraints and possible solutions. Chapter 3 presents a novel approach to learning the kinematics of the arm. Chapter 4 presents an implementation for calibration of the Utah-MIT Dextrous Hand. Chapter 5 generalizes Chapter 4 to calibration of a hand-eye system. Chapter 6 discusses the relevance of the methods presented in the previous chapters to human motor control.

The second problem investigated is the control of rapid arm movement. This dynamic control problem has received considerable attention in both motor control

and robotics research; thus there are ample theories of arm control. What is missing is experimental evidence to distinguish theories of feedforward versus feedback control, and to understand the role of intrinsic muscle properties. Thus, the second part of the thesis focuses on measuring the mechanical properties of the human elbow joint during movement. These properties are used to assess current theories of arm control.

This study represents the beginning of a series of planned experiments that will eventually investigate whole arm movements. An important contribution is the development and verification of instrumentation and system identification methods required for these future studies.

Chapter 7 discusses the various movement control hypotheses and how mechanical impedance estimates may distinguish these hypotheses. Chapter 8 discusses the previous research with an emphasis on instrumentation methods. Chapter 9 discusses the methodology for the present studies. Chapter 10 presents the results from elbow joint movements. Chapter 11 assesses theories of motor control in light of Chapter 10.

Part I

Autonomous Kinematic Calibration

Chapter 2

Learning Sensorimotor Transformations

The human motor control system is distinguished from current robotic control systems by its remarkable ability to calibrate itself and adapt. Starting from clumsy infant movements, it is able to gradually develop itself to the point where walking, reaching, writing, playing tennis, etc., are all effortless. This adaptability entails autonomously acquiring knowledge (internal models) of the mechanical properties of the links, actuators, sensors, and environment. While current robotics systems may rely on an engineer to provide such knowledge, robotics systems are fast becoming sufficiently complex that human-like autonomous learning will soon be essential. Thus, both from the point of view of understanding the human motor control system, and of designing advanced robotic systems, it has become necessary to investigate autonomous learning.

Any autonomous system, such as the human motor control system, has only the internal consistency of its various sensors to rely upon for model building (learning). To develop the notion of learning from internal consistency constraints, the problem of learning the kinematic parameters (relative link orientations and lengths) of general revolute joint manipulators is focused on. It is demonstrated that, provided the manipulator has sufficient redundancy, the kinematic parameters may be estimated using only the consistency constraints among the joint angle sensors. These consis-

tency constraints are generated by having the manipulator form a mobile closed-loop kinematic chain (e.g., as may be done by opposing one's thumb to fore finger). The method has been implemented for calibrating the Utah-MIT Dextrous Hand, and as well extended to include autonomous camera calibration for hand-eye coordination.

2.1 Terminology

It is convenient to identify each joint sensor reading (e.g., joint angle, or muscle length) with a distance along a separate coordinate axis in a multi-dimensional space. Such an intrinsically defined space is referred to as a *joint space*. Likewise, the visual system has a intrinsic coordinate system that is referred to as *retinotopic space*. More generally, the term *sensor space* refers to other sensory modalities. We will also use the term to refer to the It is also useful to speak of a set of three-dimensional (3-D) world coordinates (e.g., Cartesian coordinates) that are fixed to the body, head or world. Such coordinates are often defined by the natural constraints of a task. This 3-D coordinate system is variably referred to as *task space, hand space, or world-based coordinates*. See Figure 2-1.

The transformations between the various sensory modalities considered in this part of the thesis are static, and are thus referred to as *kinematic* transformations – as opposed to *dynamic* transformations that convert muscle forces into joint angle trajectories.

2.2 Problem Statement

The relationship between our many sensors and muscles is non-linear and non-unique, yet we are able to utilize information gathered from one sensory modality (e.g., vision) to coordinate and control another (e.g., an arm) without continuous feedback. Our ability to make transformations between sensors is what underlies observed motor equivalence, such as our being able to write comparably with any appendage. As Held [29] points out, this ability to transform sensory information cannot be hard-

(x, y)

θ_3

T

θ_3

y

Arm

$(\theta_1, \theta_2, \theta_3)$

θ_2

θ_1

θ_1

θ_2

x

(a)

(b)
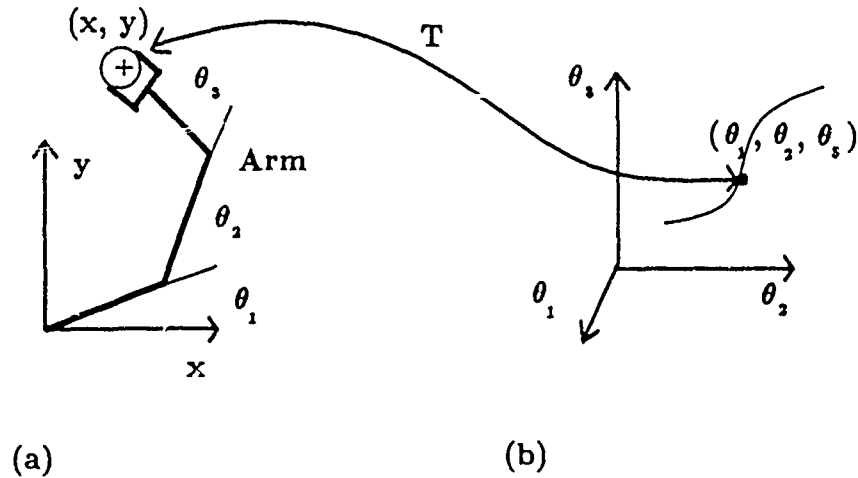
Figure 2-1: (a) Task space and (b) joint space.

wired at birth: the transformations must adapt (calibrate) whenever growth, injury, or artificial manipulations occur. The central problem is to determine how calibration of these transformations is achieved.

2.3 Representation

The answer to the question of how calibration occurs depends on the representation of the transformations to be calibrated. The simplest representation is that of a large memory (look-up table) that relates the sensor_ in a discretized form (e.g., see [30]). For example, the transformation that maps joint angles of my left arm into joint angles of my right arm (when the hands are in the same location) can be represented by remembering all points in the right arm joint space that correspond to each point in the left arm joint space. This map is not one-to-one and requires substantial memory — perhaps even too much for our highly parallel brain architecture. On the related problem of determining the appropriate torques for moving the arm along a specified trajectory, there have been numerous proposals to reduce the memory size: hash tables [14], variable density table filling [17], and state-space methods [15].

On the other extreme, the transformation may be represented by structured models with parameters that reflect the mechanical constraints of the sensorimotor system

(e.g., see [16]). This is the representation developed in this thesis. The hypothesis is that we have a priori knowledge of the structure of our limbs and sensors. For example, it is useful to assume:

- rigid limbs

- revolute joints

- linear joint angle sensors

These assumptions may be refined as needed (e.g., muscle geometry may be included), but such additional complexity would obscure, rather than clarify, the calibration problem and so is not introduced here.

The above structural assumptions allow the development of parametric equations representing the sensory transformations. Calibration then proceeds by adjusting the parameters in the model (e.g., link lengths, and orientations) until the desired transform between any two sensory modalities is achieved.

The benefits of this approach are that less memory is needed, and more generality and abstraction (see Section 3.4) is possible after calibration. This is because the structure of the model itself constrains the class of possible transformations a priori.

A model-based approach also has a cost: (1) the kinematic parameter estimation usually involves a difficult non-linear search and (2) the structures of the models of our sensors and limbs are necessarily approximate; thus, accuracy is compromised. These two points are not separate; model accuracy may be exchanged for complexity of parameter estimation. For example, in camera calibration Direct Linear Transforms (DLT's) [31] are used extensively for their ease of parameter estimation, yet the DLT method implicitly approximates the camera model with ideal projection properties, and it over-parameterizes the equations to make them linear.

Finally, the use of structured models does not preclude memory-based representations. Memory-based methods may be used locally to improve a structured model's accuracy (trajectory learning) [16]; or even more extreme, they may be used to obviate the need to calculate inverse-kinematics. These issues are tangent to the main

23

topic of calibration. In calibrating sensor transformations there is still a more subtle problem that must now be addressed

2.4   Learning Transformations to a 3-D World

Learning transformations to task space is more difficult than learning transformations between sensors. The difficulty is that there are not sensors that directly provide 3-D coordinate information (or some metrical equivalent). It is not sufficient to assume that the visual system provides task-space coordinates, for the visual system must itself be calibrated. Thus, the methods of learning by association of input-output pairs must be re-thought – regardless of how the transformations are represented.

2.4.1   Is there a Task Space?

The problem of learning to transform sensor data into a common abstract reference frame (e.g., task space) is so serious that it is tempting to think that we might *not* maintain such a 3-D world representation. As discussed in Chapter 6 this thought is probably wrong. It would be hard to imagine doing the type of reasoning that we are capable of without an internal 3-D representation of the world; without it, we would have to reason in joint space (or retinotopic space) where distances in the world are not preserved, rigid objects distort as they are sensed in different locations, and kinematic redundancy turns points in the world into surfaces. Thus, short of claiming that we do not maintain a metrical representation of the world (instead using only topological properties that are preserved by the sensory transformations [32, page 49]), it must be concluded that we somehow learn transformations from our sensor spaces to a 3-D task space.

2.4.2   Teacher Based Methods Do Not Suffice

Assuming that we do learn transformations to a 3-D task space, and assuming that task space is distinct from joint space or retinotopic space, it is possible to re-assess

the old dispute between memory-based and structured model-based learning – at least for kinematics.

To learn the transformations from task space to joint space some external agent (teacher) must provide the task-space coordinates of the hand location corresponding to a given arm configuration (point in joint space). This requires the equivalent of the construction of a measurement machine against which to calibrate our sensors. Although this is a standard approach in robotics, it is an unreasonable proposition to explain how an infant learns to transform sensory data into a common task-space coordinate frame. Thus, black-box learning methods, such as unstructured neural networks or memory look-up tables, do not suffice for learning to transform data to an abstract task space.

2.4.3 A Priori Knowledge of Physical Structure Enables Abstraction

The situation is more promising for structured models. As mentioned, structured models have a representation of the 3-D world built into them. They provide the necessary constraints by which to compare disparate sensory information. Calibration may proceed by adjusting the parameters of the transformation models so as to maximize the consistency among the sensors. Once the parameters are estimated, transformations to an abstract task space can be computed analytically. Let us see how this might work in a very simple example.

2.5 Simple Planar Calibration Example

Consider a 3-DOF planar manipulator making a point contact with the ground. This manipulator is redundant with respect to the point contact constraint, and thus forms a mobile 4-bar closed linkage. See Figure 2-2. (Figure 2-2 may be viewed alternately as a 1-DOF manipulator being tracked by a 2-DOF manipulator.) The ground is considered to be the fourth link with a fixed length of a_4. The goal is to determine the kinematic parameters a_1, a_2, a_3, and a_4 from the joint angle readings θ_1, θ_2 and θ_3.
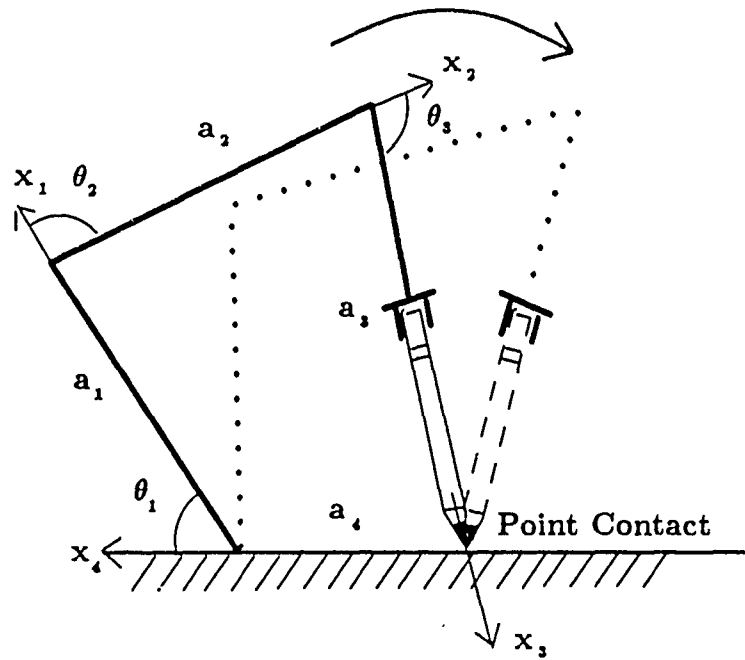
Figure 2-2: A 3-DOF planar manipulator with a fixed point contact to ground.

The three kinematic constraint equations (at the *ith* configuration) may be written as:

$$a_1 cos(\theta_1^i) + a_2 cos(\theta_1^i + \theta_2^i) + a_3 cos(\theta_1^i + \theta_2^i + \theta_3^i) + a_4 = 0 \qquad (2.1)$$

$$a_1 sin(\theta_1^i) + a_2 sin(\theta_1^i + \theta_2^i) + a_3 sin(\theta_1^i + \theta_2^i + \theta_3^i) = 0 \qquad (2.2)$$

$$\sum_{j=1}^{4} \theta_j^i = 0 \qquad (2.3)$$

Evidently, the length parameters may be scaled arbitrarily and still satisfy equations (2.1) and (2.2). For this reason one link length must be defined as unity. Let $a_4 = 1$. To continue, each additional configuration of the mechanism provides two additional position equations. Placing the equations from two configurations into matrix form we have:

$$\underline{0} = C\underline{\varphi} + \underline{y} \qquad (2.4)$$

26

where $\underline{\varphi} = (a_1 \ a_2 \ a_3)^T$, $\underline{y} = (1 \ 0 \ 1 \ 0)^T$, $\phi_j^i = \sum_{k=1}^{j} \theta_k^i$ and

$$
C = \begin{bmatrix} \cos(\phi_1^1) & \cos(\phi_2^1) & \cos(\phi_3^1) \\ \sin(\phi_1^1) & \sin(\phi_2^1) & \sin(\phi_3^1) \\ \cos(\phi_1^2) & \cos(\phi_2^2) & \cos(\phi_3^2) \\ \sin(\phi_1^2) & \sin(\phi_2^2) & \sin(\phi_3^2) \end{bmatrix} \tag{2.5}
$$

The least squares solution is $\underline{\varphi} = (C^T C)^{-1} C^T (-\underline{y})$. A unique solution is guaranteed provided that the columns of C are independent. Observe that the columns of C will only be dependent if the mechanism happens to be a parallelogram (that is, $\phi_1^i = \phi_3^i$). Once calibration is complete (i.e., $\underline{\varphi}$ is determined), arbitrary positioning of the manipulator in task space is possible with the kinematic equations (2.1) and (2.2).

2.6 Closed-Loop Kinematic Calibration

In the next three chapters the above example will be generalized, and referred to as *closed-loop kinematic calibration*. In contrast to the planar example, the general calibration equations are non-linear. Thus, the calibration must proceed iteratively, starting with initial parameter estimates, and may arrive at local or multiple solutions. It is crucial that eventually the parameters are uniquely determined by the data and constraint equations; if they are not, they may only model the training data set locally, and may not be of use in computing transformations to arbitrary points in task space.

Though the calibration method will be developed strictly in the context of robotics, the generalization to motor control should be clear from the discussion in this chapter. After developing the method, Chapter 6 will further discuss the relevance of this model-based approach to motor control.

Chapter 3

Closed-Loop Kinematic Calibration

3.1 Introduction

Kinematic calibration is important for model-based robot control [16]. We [33] and many other authors (see review paper [34]) have developed open-loop methods that estimate the geometric and static non-geometric kinematic parameters of open-chain manipulators, by relying on special purpose pre-calibrated endpoint locating systems, such as precision points or camera-based measurement systems. Section 3.2 summarizes our open-loop method, which is the starting point for our new method; new results on the identifiability of the open-loop method are also provided.

Our new method, which we call *closed-loop kinematic calibration,* eliminates the need for endpoint locating systems: *if a manipulator is formed into a mobile closed kinematic chain, then its joint angle readings alone are enough to identify the kinematic parameters.* A manipulator may form a mobile closed-loop kinematic chain if it is redundant with respect to its endpoint constraint (task). Section 3.3 considers the simplest endpoint constraint: the position and orientation of the endpoint are fixed relative to the base link. For this 0-DOF task, the manipulator must be redundant (≥ 7 DOFs) to form a mobile closed loop. For each loop configuration there are three position and three orientation loop consistency equations. If the closed loop is placed

28

into n configurations (with the same endpoint location), there result $6n$ equations that may be solved for the unknown parameters.

An equivalent scenario is two manipulators rigidly attached together at their endpoints with a combined total of DOFs ≥ 7. The last link of the second manipulator may be defined as the base, and the entire closed kinematic chain may be viewed as a single equivalent manipulator.

Section 3.4 then considers two endpoint constraints with passive degrees of freedom: 1) rotation about a passive revolute joint (e.g., opening a door), and 2) rotation about a passive spherical joint (e.g., point contact). For constraint 1 a non-redundant 6-DOF manipulator can form a *mobile* closed loop, while for constraint 2 a 4-DOF manipulator could suffice. In general, for each passive degree of freedom introduced into the endpoint constraint one less degree of freedom is required by the manipulator. As a corollary, the geometry of the task can also be identified, for example, the position and orientation of the revolute joint in constraint 1.

Several technicalities were overcome in developing this closed-loop method. A theorem was developed to determine which parameters are identifiable in the consistency equations. We also show how the passive DOFs can be eliminated from the endpoint constraint for the two cases studied, and mention how to do it in general. Thirdly, we apply a Newton-like search method for the kinematic parameters, which starts from an initial guess at the parameters. Simulations will demonstrate the convergence of the method. Finally, the manipulator must be able to make constrained internal joint movements, without knowing the true kinematic parameters or producing excessive internal or endpoint forces.

Closed-loop kinematic calibration is related to mechanism synthesis [35], which characterizes closed-loop mechanisms with one degree of mobility through relative displacements of designated input and output angles. By eliminating (with difficulty) the five unspecified DOFs from the kinematic equations, a displacement equation results that is a 16th order polynomial in the tangent half-angles of the input and output angles [36]. A difference from mechanism synthesis is that serial-chain manipulators typically have sensors on all the joints, and so eliminating the unsensed

29
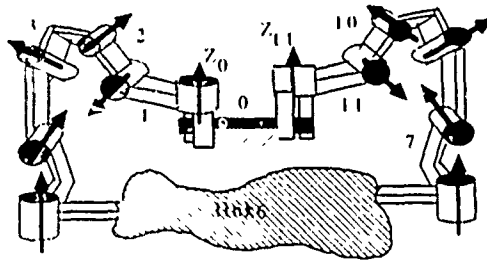
Figure 3-1: A single closed-loop kinematic chain formed by a redundant manipulator or by dual manipulators.

passive DOFs at the endpoint from the kinematic equations is considerably easier. Portions of this work have been previously reported [37], [38], [39].

3.2 Open-loop kinematic calibration

This section presents our method for open-loop kinematic calibration [33], which serves to set the basic concepts and mathematics from which the closed-loop method is derived. New results in identifiability are presented for our open-loop method; these results apply more generally to similar methods that have appeared in the literature [34].

3.2.1 The Kinematic Model

Both geometric and non-geometric parameters are required for kinematic calibration. The Denavit-Hartenberg (D-H) convention [40] is employed for the geometric parameters (Figure 3-2). For a manipulator with n DOFs, the end effector is located by the position vector $\mathbf{p}_c^i$ and the orientation matrix $\mathbf{R}_c^i$:

$$\mathbf{p}_c^i = \sum_{j=1}^{n} s_j z_{j-1} + a_j x_j \tag{3.1}$$

$$\mathbf{R}_c^i = \prod_{j=1}^{n} \mathbf{R}_z(\theta_j^i)\mathbf{R}_x(\alpha_j^i) \tag{3.2}$$

30
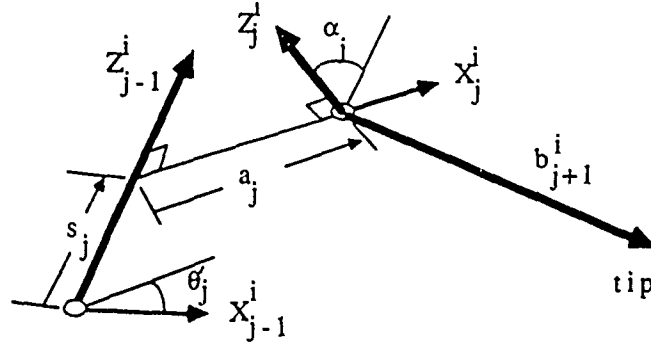
Figure 3-2: Denavit-Hartenberg coordinates and tip vector b_j^i.

where $\mathbf{R}_z(\phi)$ and $\mathbf{R}_x(\phi)$ are 3×3 rotation matrices about $\mathbf{z}$ and $\mathbf{x}$ axes by the angle ϕ, and the subscript c indicates that the position and orientation are computed from the model. The superscript i refers to the configuration of the manipulator, since in kinematic calibration it is placed into a number of configurations $\underline{\theta}^i = (\theta_1^i, \ldots, \theta_n^i)$, $i = 1, \ldots, m$. The required geometric parameters are s_j, α_j and a_j, for links $j = 1, \ldots, n$.

The non-geometric parameters are focused at a joint, and reflect errors between the true and measured joint angle; sources of error include backlash, gear eccentricity, joint compliance, and joint angle offset. We model only the joint angle offset error θ_j^{off}, which needs to be identified. It is related to the actual θ_j' and measured θ_j D-H joint angles by $\theta_j' = \theta_j + \theta_j^{off}$. All of the unknown kinematic parameters are placed into a single vector $\underline{\varphi} = (\underline{\theta}^{off}, \underline{s}, \underline{a}, \underline{\alpha})$, where $\underline{s} = (s_1, \ldots, s_n)$, etc.

Instead of the orientation matrix $\mathbf{R}_c^i$, it is convenient to represent the orientation by the vector $\mathbf{r}_c^i = (\phi_x, \phi_y, \phi_z)$, representing the xyz Euler angles. The computed endpoint location $\underline{x}_c^i = (\mathbf{p}_c^i, \mathbf{r}_c^i)$ may then be written as:

$$\underline{x}_c^i = \underline{f}(\underline{\theta}^i, \underline{\varphi}) \tag{3.3}$$

where the function $\underline{f}$ is derive' from (3.1)-(3.2). It's exact form is not required here.

3.2.2 Iterative Identification

To estimate $\underline{\varphi}$, the manipulator must be moved into an adequate number m of configurations, in consideration of the large number of parameters in $\underline{\varphi}$ and of statistical averaging. At each configuration i the actual endpoint location $\underline{x}_a^i$ is measured. The goal is to determine the $\underline{\varphi}$ that best predict from the kinematic model (3.3) all of the endpoint measurements $\mathcal{X} = (\underline{x}_a^1, \ldots, \underline{x}_a^m)$:

$$\mathcal{X} = \mathcal{F}(\underline{\varphi}) \tag{3.4}$$

where $\mathcal{F}(\underline{\varphi}) = (\underline{f}(\underline{\theta}^1, \underline{\varphi}), \ldots, \underline{f}(\underline{\theta}^m, \underline{\varphi}))$.

Solving for $\underline{\varphi}$ from (3.4) is a nonlinear estimation problem, which can be done by linearization and iteration:

$$\Delta \mathcal{X} = \mathcal{C} \Delta \underline{\varphi} \tag{3.5}$$

where $\mathcal{C} = \partial \mathcal{F} / \partial \underline{\varphi}$. We can consider $\Delta \mathcal{X} = (\Delta \underline{x}^1, \ldots, \Delta \underline{x}^m)$, with $\Delta \underline{x}^i = \underline{x}_a^i - \underline{x}_c^i$, as the location errors. Similarly, $\Delta \underline{\varphi} = \underline{\varphi} - \underline{\varphi}_0$ is the error in the total parameter set, where $\underline{\varphi}_0$ is the current estimate and $\underline{\varphi}$ is the corrected estimate. In $\Delta \underline{\varphi}$, $\Delta \underline{s} = \underline{s} - \underline{s}_0$, etc. An estimate of the parameter errors is provided by minimizing $LS = (\Delta \mathcal{X} - \mathcal{C} \underline{\varphi})^T (\Delta \mathcal{X} - \mathcal{C} \underline{\varphi})$, which yields

$$\Delta \underline{\varphi} = (\mathcal{C}^T \mathcal{C})^{-1} \mathcal{C}^T \Delta \mathcal{X} \tag{3.6}$$

Finally, the guess at the parameters is updated as $\underline{\varphi} = \underline{\varphi}_0 + \Delta \underline{\varphi}$ and the iteration continues until $\Delta \mathcal{X} \to 0$.

The basis for linearization is the assumption that $\underline{x}_c^i$ is close to $\underline{x}_a^i$. Then

$$\Delta \underline{x}^i = \underline{x}_a^i - \underline{x}_c^i = (dx^i, dy^i, dz^i, \partial x^i, \partial y^i, \partial z^i) \tag{3.7}$$

where $\Delta \mathrm{p}^i = (dx^i, dy^i, dz^i)$ is the incremental position error and $\Delta \mathrm{r}^i = (\partial x^i, \partial y^i, \partial z^i)$ is the incremental orientation error. When $\underline{\varphi}_0$ is far from the final values, problems with this approach may occur, as discussed later.

The Jacobian $\mathcal{C}$ is often formed through the use of differential homogeneous transformations, but to address identifiability we find the use of screw coordinates more convenient and transparent [41], [42], [43]. The differential of (3.3) is

$$\Delta \underline{x}^i = \frac{\partial \underline{x}_c^i}{\partial \underline{\theta}} \Delta \underline{\theta} + \frac{\partial \underline{x}_c^i}{\partial \underline{s}} \Delta \underline{s} + \frac{\partial \underline{x}_c^i}{\partial \underline{a}} \Delta \underline{a} + \frac{\partial \underline{x}_c^i}{\partial \underline{\alpha}} \Delta \underline{\alpha} = \mathbf{C}^i \Delta \underline{\varphi} \qquad (3.8)$$

where

$$\mathbf{C}^i = \frac{\partial \underline{x}_c^i}{\partial \underline{\varphi}} = \begin{bmatrix} \frac{\partial \underline{x}_c^i}{\partial \underline{\theta}} & \frac{\partial \underline{x}_c^i}{\partial \underline{s}} & \frac{\partial \underline{x}_c^i}{\partial \underline{a}} & \frac{\partial \underline{x}_c^i}{\partial \underline{\alpha}} \end{bmatrix}$$

and

$$\mathcal{C} = \begin{bmatrix} \mathbf{C}^1 \\ \cdot \\ \mathbf{C}^n \end{bmatrix} \qquad (3.9)$$

Subsequently, we use the abbreviation $\mathbf{J}_\beta^i = \partial \underline{x}_c^i / \partial \beta$, as each matrix in (3.8) is a Jacobian with respect to a particular parameter; thus $\mathbf{J}_\theta^i$ is the ordinary Jacobian related to joint angle displacement.

The endpoint variation $\Delta \underline{x}^i$ can be considered an instantaneous screw displacement composed of an incremental translation $\Delta \mathbf{p}^i$ and rotation $\Delta \mathbf{r}^i$, caused by the combined variation in all of the parameters. For example, a variation Δs_j contributes $\Delta s_j \mathbf{z}_{j-1}^i$ to $\Delta \mathbf{p}^i$. A variation $\Delta \alpha_j$ contributes $(\Delta \alpha_j) \mathbf{x}_j^i$ to $\Delta \mathbf{r}^i$ and $(\Delta \alpha_j) \mathbf{x}_j^i \times \mathbf{b}_{j+1}^i$ to $\Delta \mathbf{p}^i$, where $\mathbf{b}_{j+1}^i$ is a vector from the jth coordinate system to the endpoint (Figure 3-2). The θ_j and a_j parameters are treated analogously. In total,

$$\Delta \mathbf{p}^i = \sum_{j=1}^{n} \mathbf{z}_{j-1}^i \times \mathbf{b}_j^i \Delta \theta_j + \mathbf{z}_{j-1}^i \Delta s_j + \mathbf{x}_j^i \times \mathbf{b}_{j+1}^i \Delta \alpha_j + \mathbf{x}_j^i \Delta a_j \qquad (3.10)$$

$$\Delta \mathbf{r}^i = \sum_{j=1}^{n} \mathbf{z}_{j-1}^i \Delta \theta_j + \mathbf{x}_j^i \Delta \alpha_j \qquad (3.11)$$

Comparing to (3.8), it is seen that

33

$$(\mathbf{J}_a^i)_j = \begin{bmatrix} \mathbf{x}_j^i \\ 0 \end{bmatrix}, \; (\mathbf{J}_s^i)_j = \begin{bmatrix} \mathbf{z}_{j-1}^i \\ 0 \end{bmatrix}, \; (\mathbf{J}_\theta^i)_j = \begin{bmatrix} \mathbf{z}_{j-1}^i \times \mathbf{b}_j^i \\ \mathbf{z}_{j-1}^i \end{bmatrix}, \; (\mathbf{J}_\alpha^i)_j = \begin{bmatrix} \mathbf{x}_j^i \times \mathbf{b}_{j+1}^i \\ \mathbf{x}_j^i \end{bmatrix}$$

$$(3.12)$$

where the jth column of each Jacobian $\mathbf{J}_\beta^i$ is indicated by the subscript, and represents a screw coordinate for variation in the parameter β_j.

3.2.3 Identifiability

Next we derive several results pertaining to the identifiability of $\underline{\varphi}$ in (3.4). First we establish that the solution cannot be globally unique.

Theorem 1 *There are at least 2^{n-1} solutions $\underline{\varphi}$ to (3.4).*

Proof. We presume that at least one solution $\underline{\varphi}$ exists, because the data come from a physical system. Additional solutions may be derived from this $\underline{\varphi}$. There are two possible parameter sets per joint. For a fixed $\mathbf{z}_j^i$, the $\mathbf{x}_j^i$ axis can be made to point in opposite directions by adding 180° onto θ_j^{off}; to accommodate this change, the sign is changed on a_j and α_j while s_j is unchanged. At the endpoint, the directions $\mathbf{x}_n^i$ and $\mathbf{z}_n^i$ are specified by the position requirement. Hence we have generated 2^{n-1} solutions from the original solution $\underline{\varphi}$. $\square$

Though there are multiple solutions, in practice kinematic calibration starts off with a rough estimate $\underline{\varphi}_0$ and searches locally for a solution. Thus, the relevant question is whether or not there is a unique solution within a small region of the parameter space. We draw on some results from differential topology [44], [45].

Definition 1 (Locally unique) *A solution $\underline{\varphi}'$ to (3.4) is locally unique if it is the only solution in an arbitrarily small neighborhood (ball) around $\underline{\varphi}'$.*

In addition to uniqueness, we also want to know if a well-behaved inverse function $\mathcal{F}^{-1}$ exists to generate the solution $\underline{\varphi}'$.

Definition 2 (Locally identifiable) *A smooth function* $\mathcal{X} = \mathcal{F}(\underline{\varphi})$ *is locally identifiable at* $\underline{\varphi}'$ *if (1)* $\underline{\varphi}'$ *is locally unique, and (2) there exists a smooth inverse function* $\mathcal{F}^{-1}$ *such that* $\mathcal{F}^{-1}(\mathcal{F}(\underline{\varphi})) = \underline{\varphi}$.

A smooth function has continuous partial derivatives of all orders. Notice that the existence of a smooth inverse function in part 2 of the definition does not guarantee uniqueness (part 1).

If the number of equations equals the number of unknown parameters, then local identifiability is equivalent to requiring that $\mathcal{F}$ is a *local diffeomorphism*. It is established in [44] that $\mathcal{F}$ is a local diffeomorphism if and only if the square Jacobian matrix $C = [\partial \mathcal{F}/\partial \underline{\varphi}']$ is non-singular. This motivates the following results for when C is not necessarily square. Lemma 1 is a general result that applies to all equations of the form (3.4). Lemmas 2 and 3 are particular to the kinematic calibration problem.

Lemma 1 *Let* $\underline{\varphi}'$ *be a solution to (3.4). The Jacobian C has full rank if and only if the parameters* $\underline{\varphi}'$ *are locally identifiable.*

Proof. Assume C has full rank. Let $\underline{\varphi}$ be another solution to (3.4). A Taylor series expansion relates $\underline{\varphi}$ to $\underline{\varphi}'$:

$$\mathcal{F}(\underline{\varphi}) = \mathcal{F}(\underline{\varphi}') + C(\underline{\varphi} - \underline{\varphi}') + \cdots \tag{3.13}$$

where $\mathcal{F}(\underline{\varphi}) = \mathcal{F}(\underline{\varphi}')$. If φ is in a sufficiently small neighborhood of $\underline{\varphi}'$, then the higher order terms after the first differential may be neglected. Then $C(\underline{\varphi} - \underline{\varphi}') = 0$. Since C does not have a null space, then $\underline{\varphi} = \underline{\varphi}'$, and $\underline{\varphi}'$ is locally unique. Furthermore, there exists a smooth inverse function $\mathcal{F}^{-1}$, as (3.6) suffices.

Conversely, assume the parameters $\underline{\varphi}'$ are locally identifiable. Let $\mathcal{F}^{-1}$ be a smooth inverse function. Differentiating $\mathcal{F}^{-1}(\mathcal{F}(\underline{\varphi})) = \underline{\varphi}$ by φ yields $[\partial \mathcal{F}^{-1}/\partial \mathcal{X}][\partial \mathcal{F}/\partial \underline{\varphi}] = I$. If C does not have full rank, then there exists a vector element $\underline{n}$ of its null space. Postmultiplying by $\underline{n}$ yields $\underline{0} = \underline{n}$, a contradiction. Hence C has full rank. $\square$

If Jacobian C has dependent columns, the solution to (3.4) is not necessarily locally unique because the higher order terms of the Taylor series expansion of $\mathcal{F}$ may be

non-zero when evaluated at an element of the null space of C. The following two lemmas require the definition of C by (3.8); they do not hold in Section 3.3.

Lemma 2 *The Jacobian C does not have full rank if and only if there exists a constant linear relation among the $\mathbf{x}_j^i$ and $\mathbf{z}_j^i$ axes, that is,*

$$0 = \sum_{j=1}^{n} c_j \mathbf{z}_{j-1}^i + k_j \mathbf{x}_j^i \qquad (3.14)$$

for some constants c_j and k_j, not all zero, for all configurations $i = 1, \ldots, m$.

Proof. Part 1: Assume C does not have full rank. Then there is a constant linear relation among the screw coordinates (3.12). Two cases must be considered. First, if this linear relation only includes the left two screw coordinates in (3.12), then the same linear relation must hold in the positional component of the screws, the first three rows that contain just the $\mathbf{x}_j^i$ and $\mathbf{z}_j^i$ axes. Thus (3.14) holds for some constants c_j and k_j, not all zero, for all configurations $i = 1, \ldots, m$. Second, if this linear relation includes the right screws in (3.12), then this linear relation must hold in the rotational component of the screws, the last three rows that also contain just the $\mathbf{x}_j^i$ and $\mathbf{z}_j^i$ axes. Again, (3.14) holds.

Part 2: Conversely, assume (3.14) holds. Then at least the screw coordinates $(\mathbf{J}_a)_j$ and $(\mathbf{J}_s)_j$ have a constant linear dependence, and C does not have full rank. □

Lemma 3 *C has full rank if and only if $\underline{\varphi}'$ is locally unique.*

Proof. Assume C has full rank. By Lemma 1, $\underline{\varphi}'$ is locally identifiable and hence is locally unique. Next assume $\underline{\varphi}'$ is locally unique. If C did not have full rank, then by Lemma 2 we could add (3.14) to (3.1) to change the length parameters without affecting $\mathbf{p}_c^i$. The kinematic length parameters would not be unique, contradicting the assumption. Hence C has full rank. □

Theorem 2 (Identifiability) *The parameters $\underline{\varphi}$ are locally unidentifiable or locally non-unique if and only if there exist constants c_j and k_j, not all zero, such that*

36

$$0 = \sum_{j=1}^{n} c_j z_{j-1}^i + k_j x_j^i \tag{3.15}$$

for all configurations $i = 1, \dots, m$.

Proof. This theorem follows from Lemmas 1, 2 and 3. □

Various categories of singularities (occurrences of (3.15)), which are generic to the closed-loop case as well (see Section 3.3), will now be enumerated. These categories are meant to be illustrative rather than exhaustive. Although not expressly discussed in each category, the real problem is associated with near singular situations, which cause intractable numerical sensitivity problems while solving for the parameters.

Singularity 1: coordinate description. In the D-H convention, when there are two consecutive parallel joint axes, there is no unique common normal (Figure 3-2). Parallel axes imply:

$$z_j^i - z_{j-1}^i = 0 \tag{3.16}$$

Thus (3.15) is true and the corresponding s_i and s_{i+1} may not be identified alone (although the difference $s_i - s_{i+1}$ can be identified). T.. situation can be avoided by changing the coordinate description of the parallel axes to a convention such as Hayati's [46], which however may not be used exclusively because it too suffers from a parameter ambiguity when two consecutive joint axes are perpendicular.

A revolute joint axis is a *line vector*, which is located by 4 parameters. Hence any coordinate description with greater than 4 parameters per link is singular (unless extra constraints are imposed). Similarly, a prismatic (linear) joint axis is a *free vector* defined by only 2 orientation parameters, and coordinate descriptions with more than 2 parameters are singular.

Singularity 2: insufficient excitation. If the mechanism is not moved into a sufficient number of configurations, then the data are not *sufficiently exciting* [47]. A small variation in each parameter of φ should cause an observable displacement in the end effector. The optimal data set would maximize the observable model error over variations in all of the parameters [48]. An impoverished data set would not be able to distinguish changes in particular parameters, which could vary arbitrarily.

A trivial example is an immobile joint whose axes x_j^i, z_j^i, x_{j-1}^i, and z_{j-1}^i are always linearly dependent.

Singularity 3: transient singularities. During the course of the iterative search, an intermediate singular parameter set may be found even though the real mechanism may not have singularities. Simulations show that this situation is surprisingly common when the initial guess $\underline{\varphi}_0$ is not close to the true solution. Since this singularity is associated with the algorithm, it may be avoided by the modified minimization criteria $LS' = LS + \lambda \Delta \underline{\varphi}^T \Delta \underline{\varphi}$. In addition to minimizing the end effector tracking error, LS' minimizes the variation in parameters so that at a potential singularity the arbitrary parameters tend to remain fixed. Minimizing LS' yields

$$\Delta \underline{\varphi} = (\mathcal{C}^T \mathcal{C} + \lambda I)^{-1} \mathcal{C}^T \Delta \underline{\mathcal{X}} \qquad (3.17)$$

Iteratively applying (3.17) results in the Levenberg-Marquardt algorithm [49], [50]. The free parameter λ determines the trade-off between a straight Newton iteration and a much slower gradient descent.

3.3   Closed-Loop Kinematic Calibration

We consider next a redundant manipulator (≥ 7 DOFs) rigidly attached to the ground at its endpoint. In general, the resulting closed-loop kinematic chain is mobile, since the fixed endpoint constrains only 6 of the DOFs of the manipulator. Our closed-loop method makes use of this mobility to kinematically calibrate the manipulator without endpoint sensing. The following observation is the key: the origin of coordinates can be placed at the fixed endpoint location and can be defined to have zero orientation and position. Hence $\underline{x}_a^i = \underline{0}$, and no measurements are required because the actual endpoint location is known and is zero (by definition).

Figure 3-3 illustrates this origin placement for a 7-DOF manipulator. The combined manipulator tool and ground may be viewed as a single effective link that connects the last to first joint of the manipulator. The end effector axes z_7^i and x_7^i are
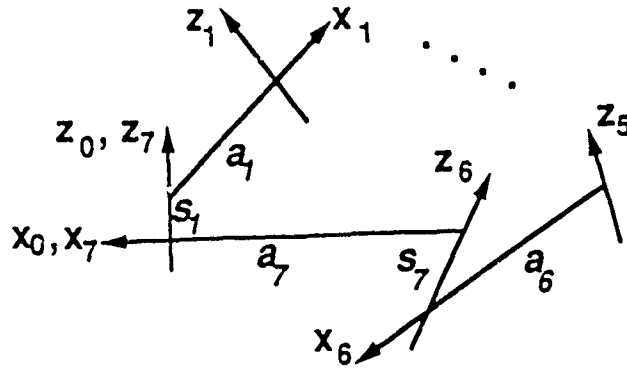
Figure 3-3: Ground link definition.

made coincident with the base coordinate axes z_0^i and x_0^i. Note that the kinematic parameters of the ground link must now be identified.

The mathematical development in the previous section then applies, with one modification. As before, the mobile closed chain is moved into a number of configurations. At each configuration i the endpoint error follows simply from (3.7):

$$\Delta \underline{x}^i = -\underline{x}_c^i = -(dx_c^i, dy_c^i, dz_c^i, \partial x_c^i, \partial y_c^i, \partial z_c^i) \tag{3.18}$$

where $\Delta \mathbf{p}^i = (dx_c^i, dy_c^i, dz_c^i)$ is the computed position and $\Delta \mathbf{r}^i = (\partial x_c^i, \partial y_c^i, \partial z_c^i)$ is the computed orientation. The iterative estimation procedure cannot be applied further without modification because the Jacobian $\mathcal{C}$ is singular. The position equations for the closed loop are:

$$\mathbf{p}_c^i = \sum_{j=1}^n s_j \mathbf{z}_{j-1}^i + a_j \mathbf{x}_j^i = 0 \tag{3.19}$$

Hence the length parameters are linearly dependent and (3.14) is satisfied. Intuitively, the size of the manipulator can be scaled arbitrarily and still satisfy the loop closure equations.

To proceed with our closed-loop method, it is necessary to specify one length parameter to scale the size of the mechanism. For example, suppose we set $a_1 = -1$. We redefine $\underline{a} = (a_2, \ldots, a_n)$ and remove the first column from the Jacobian $\mathbf{J}_a^i$, which redefines $\mathbf{C}^i$ in (3.8). We may then proceed as before with the parameter · identification. Similarly, if another parameter such as s_3 had been specified instead,

39

analogous changes in the definition of $\underline{s}$ and $\mathbf{C}^i$ would be required. In the remainder of this paper, we vary which parameter sets the scale for convenience.

3.3.1 Identifiability

For the purposes of identifiability, we will proceed with the scaling $a_1 = -1$. The following identifiability results are couched in terms of the choice of a_1, but a different choice would result in trivial changes to the results. Of course, it is necessary in the actual mechanism that $a_1 \neq 0$. We do not consider mechanisms that have all length parameters zero (i.e., spherical mechanisms).

Theorem 1 and Lemma 1 apply intact to the closed-loop case, but Lemmas 2-3 and Theorem 2 require a slight modification. Redefine the endpoint position as

$$\mathbf{p}_c^i = \mathbf{x}_1^i = \sum_{j=1}^n s_j \mathbf{z}_{j-1}^i + \sum_{j=2}^n a_j \mathbf{x}_j^i \tag{3.20}$$

Also, we must make the following definition to treat a possible exception arising from $\mathbf{x}_1^i$ being in the expression for $(\mathbf{J}_\alpha^i)_1$.

Definition 3 (Type-E Special Mechanism) *A single loop closed kinematic chain is type-e if its screw coordinates in (3.12) satisfy the following exceptional relation:*

$$0 = \sum_{j=1}^n s_j (\mathbf{J}_\theta^i)_j + a_j (\mathbf{J}_\alpha^i)_j + q_j (\mathbf{J}_s^i)_j + r_j (\mathbf{J}_a^i)_j \tag{3.21}$$

for all configurations $i = 1, \ldots, m$. q_j and r_j are arbitrary constants.

Perhaps (3.21) never occurs, but for completeness we include its possibility.

The new identifiability theorem can now be stated.

Theorem 3 (Fixed Endpoint Identifiability) *For a redundant manipulator with fixed endpoint forming a closed kinematic chain that is not type-e, the parameters $\underline{\varphi}$ are locally unidentifiable, or locally non-unique if and only if there exist constants c_j*

and k_j, not all zero and not all $c_j = s_j$ and $k_j = a_j$, such that

$$0 = \sum_{j=1}^{n} c_j z_{j-1}^i + k_j x_j^i \qquad (3.22)$$

for all configurations $i = 1, \ldots, m$. Furthermore, the parameters of a type-e mechanism are non-unique, if (3.22) holds for the c_j and k_j restricted as above.

Proof. With the added restriction that not all $c_j = s_j$ and $k_j = a_j$ Lemma 2 holds if x_1^i is eliminated from (3.14) by substitution of (3.20), provided that the mechanism is not type-e. Lemma 3 holds if its proof is modified to use (3.14), with x_1^i eliminated, and (3.20) instead of (3.1). Alternatively, for all mechanism types local non-uniqueness follows directly from (3.22) by adding (3.22) to (3.20) and remarking, as in the proof to Lemma 3, that the length parameters are non-unique. This theorem then follows. □

For type-e mechanisms the angle-dependent screw coordinates $(\mathbf{J}_\alpha^i)_j$ and $(\mathbf{J}_\theta^i)_j$ in (3.12) are linearly related by the length parameters as defined above. The orientation component of this linear screw relation (the last 3 rows) gives (3.14) with $c_j = s_j$ and $k_j = a_j$ for all joints $j = 1, \ldots, n$. This provides no addition information, as it is the same as (3.20), and case 2 in part 1 of the proof to Lemma 2 cannot proceed. We do not know if a type-e mechanism can actually occur and do not consider it further.

We now discuss two additional singularities in the closed-loop calibration procedure to the three singularities in the open-loop procedure that also apply here.

Singularity 4: Inherent singularities in the mechanism. Certain mechanisms have particular symmetries that allow the kinematics to be described in less than four parameters per joint. It is difficult to provide a general rule for when this will happen, but it is usually restricted to mechanisms of mobility one. A simple example is a 3-DOF planar manipulator that makes a point contact with the ground (Figure 2-2). If the resulting closed-loop, four-bar linkage happens to be a parallelogram, then the opposite x axes are always parallel:

$$x_2 + x_4 = 0 \qquad (3.23)$$

41

This satisfies the condition (3.22), and thus the lengths of the opposite sides, a_2 and a_4, are not identifiable (except as a sum). Clearly, this problem may be eliminated by having the manipulator change its endpoint location so that a parallelogram is not formed.

Singularity 5: structural immobility. If a particular joint j is immobile, then two consecutive joint coordinates are fixed relative to one another. This implies that x_j, z_j, x_{j-1}, and z_{j-1} have a constant linear relation (satisfying (3.22)), as these four vectors span a three dimensional space. Of course, it is not surprising that the parameters of the links connected by the immobile joint are unidentifiable. Conceivably a fictitious link that combined the two links could be defined and the rest of the mechanism identified.

To proceed, it is necessary to spot immobile joints. Following the approach in [42], we first determine whether the mechanism is totally immobile. Since the classical mobility definition [35] does not suffice for special mechanisms, the following condition is derived.

Lemma 4 *A single-loop closed kinematic chain is mobile if and only if the columns of the Jacobian $\mathbf{J}_\theta^i$ are linearly dependent.*

Proof. Let the screw coordinate $\$_j^i$ represent the jth column of $\mathbf{J}_\theta^i$. Since $\mathbf{J}_\theta^i \dot{\underline{\theta}}^i = \underline{0}$, then

$$\underline{0} = \dot{\theta}_1^i \$_1^i + \cdots + \dot{\theta}_n^i \$_n^i \tag{3.24}$$

All $\dot{\theta}_j^i$'s will be identically zero if and only if the joint screws $\$_j^i$ are independent. $\square$

Next we determine whether a single joint, say joint 1, is immobile. From (3.24), link one's instantaneous movement is $\dot{\theta}_1^i \$_1^i = -\dot{\theta}_n^i \$_n^i - \cdots - \dot{\theta}_2^i \$_2^i$. For link one to move, $\$_1^i$ must be a linear combination of the other screws. Stated otherwise, the space $span[\$_1^i]$ must intersect the space $span[\$_n^i, \ldots, \$_2^i]$ spanned by the other screws. The following result from linear algebra is useful [51].
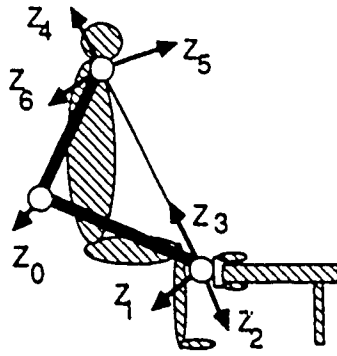
Figure 3-4: Anthropomorphic arm screw coordinate assignment.

Joint	$\underline{s}$ (m)	$\underline{a}$ (m)	$\underline{\alpha}$ (rad)	$\underline{\theta}^{off}$ (rad)
1	1.694	0.837	3.774	1.100
2	1.622	- \.627	-0.553	0.080
3	1.000	-0.100	0.930	0.090
4	-0.430	-0.430	2.040	0.900
5	0.540	-0.600	-0.150	0.050
6	-0.560	-0.550	1.350	0.040
7	-1.693	0.711	-1.859	0.000

Table 3.1: 7 DOF mechanism: initial parameters.

Lemma 5 *Let A and B be subspaces of a vector space V such that $V = A + B$, where $A + B = [v \mid v = a + b, a \in A, b \in B]$. Then*

$$K(A \cap B) = K(A) + K(B) - K(V) \qquad)$$

where $K(W)$ denotes the dimension of a vector space W.

For the following lemma, identify A with $span[\$_1^i]$ and B with $span[\$_n^i, \ldots, \$_2^i]$.

Lemma 6 *Joint one will be mobile if and only if*

$$1 + K(span[\$_n^i, \ldots, \$_2^i]) - K(span[\$_n^i, \ldots, \$_1^i]) > 0 \qquad (3.26)$$

Any joint's mobility may be ascertained by (3.26) with the appropriate re-numbering of the links.

As an example, consider the mechanism formed by rigidly fixing the hand of an anthropomorphic arm [23] relative to its shoulder (that is, imagine holding onto the

43

Joint	$\underline{s}$ (m)	$\underline{a}$ (m)	$\underline{\alpha}$ (rad)	θ^{off} (rad)
1	1.594	0.737	3.604	0.000
2	1.722	-0.527	-0.503	0.000
3	1.000	0.000	0.530	0.000
4	-0.330	-0.330	2.300	0.000
5	0.440	-0.440	-0.900	0.000
6	-0.660	-0.550	1.200	0.000
7	-1.793	0.911	-1.459	1.825

Table 3.2: 7 DOF mechanism: calibrated parameters.

Joint	$\underline{s}$ (m)	$\underline{a}$ (m)	$\underline{\alpha}$ (rad)	θ^{off} (rad)
1	-1.694	-0.837	3.504	0.100
2	-1.822	0.627	-0.553	0.050
3	1.000	0.100	0.580	0.070
4	0.430	0.430	2.380	1.070
5	-0.540	0.540	-0.980	0.080
6	0.760	0.650	1.280	0.050
7	1.200	0.760	-1.390	0.100
8	1.200	1.500	3.800	0.100
9	0.600	-1.400	1.550	0.200
10	0.300	1.100	-1.380	0.300
11	1.300	0.600	0.880	0.900
12	-1.982	-1.839	1.772	0.400

Table 3.3: 12 DOF mechanism: initial parameters.

desk in front of you). Although this mechanism has a classical mobility of 1 (7 minus 6), the elbow joint can be shown to be immobile. Consider the upper arm as the base link, so that $\$_1^i$ is the screw coordinate for the elbow (Figure 3-4). Without loss of generality, one of the three wrist joint axes may be defined to intersect the shoulder joint. Thus the three shoulder joint axes and this wrist joint axis are linearly dependent, and $K(span[\$_2^i, \ldots, \$_7^i]) = 5$ whereas $K(span[\$_1^i, \ldots, \$_7^i]) = 6$. Therefore (3.26) shows that the elbow joint is immobile. The solution to this problem is to relax the endpoint constraint so that the elbow is mobile; for example, only maintain a point contact with the ground, allowing arbitrary orientation of the hand. This solution requires a reformulation of the identification equations and is taken up in

Joint	$\underline{s}$ (m)	$\underline{a}$ (m)	$\underline{\alpha}$ (rad)	$\underline{\theta}^{off}$ (rad)
1	-1.594	-0.737	3.604	0.000
2	-1.722	0.527	-0.503	0.000
3	1.000	0.000	0.530	0.000
4	0.330	0.330	2.300	0.000
5	-0.440	0.440	-0.900	0.000
6	0.660	0.550	1.200	0.000
7	1.100	0.660	-1.300	0.000
8	1.100	1.400	3.900	0.000
9	0.500	-1.300	1.400	0.000
10	0.200	1.000	-1.300	0.000
11	1.200	0.500	0.800	0.000
12	-1.882	-1.939	1.722	0.000

Table 3.4: 12 DOF mechanism: calibrated parameters.

Section 3.4.

3.3.2   Simulations

This section presents two simulations, one for a 7-DOF manipulator and the other for two 6-DOF manipulators rigidly attached at their endpoints. In these and all subsequent examples the rank of the matrix C was monitored to avoid singularities. Further, C has full rank for the actual parameters, and thus all mechanisms are identifiable.

Example 1. A 7-DOF manipulator, with actual D-H parameters in Table 3.2, was formed into a closed loop mechanism by the end effector grasping the ground at a fixed arbitrary position. This mechanism was simulated in 40 distinct configurations ($\theta_1 =$ 0 to 0.5 *rad*). Starting with the initial guesses in Table 3.1 and with the definition $s_3 = 1$, the simulated joint angles were fed into the iterative Levenberg-Marquardt algorithm, and the parameters in Table 3.2 were recovered to within four decimal places.

Example 2. Two 6-DOF manipulators whose end effectors are rigidly grasping together form the 12-DOF closed mechanism in Table 3.4. These parameters were used to simulate the movements of this mechanism into 40 different configurations

45

($\theta_j = 0$ to 0.5 rad, $j = 1$ to 6). With the initial parameters given in Table 3.3 and the simulated joint angles the calibration was performed (also $s_3 = 1$ fixed). The parameters in Table 3.4 were recovered to within four decimal places.

3.4 Non-Redundant Robot Calibration and Task Geometry Estimation

Next we extend the closed-loop method to situations where the end effector contact with the ground has some passive DOFs. Two examples, treated in detail below, are a manipulator opening a door (a 1-DOF task) and a manipulator under point contact (a 3-DOF task). If t is the number of task DOFs, then the mobility of the resultant closed chain is $n + t - 6$. For the door-opening task, 6-DOF non-redundant manipulators can therefore be calibrated. For the point contact task, manipulators with as few as 4 DOFs may be calibrated. At the same time, the geometry of the task is calibrated.

Since the passive task DOFs are unsensed, they must be eliminated from the 6 kinematic loop closure equations. Up to 5 unsensed DOFs may be eliminated to leave at least one equation for the identification procedure. This elimination is simple for the door opening and point contact tasks, but more difficult for arbitrary task kinematics.

3.4.1 Point Contact

An n-DOF manipulator under point contact is equivalent to grasping a passive spherical ball joint. There are 3 passive DOFs at the endpoint corresponding to orientation that are unsensed. Hence the orientation equations in the previous calibration procedure cannot be used, but the three position equations (3.19) can. Again, define the base origin to coincide with the endpoint position. For example, for the 6-DOF manipulator in Figure 3-5, the position of the base coordinates (subscript -1) is coincident with that of the endpoint coordinates (subscript 6). The orientation of the -1

46
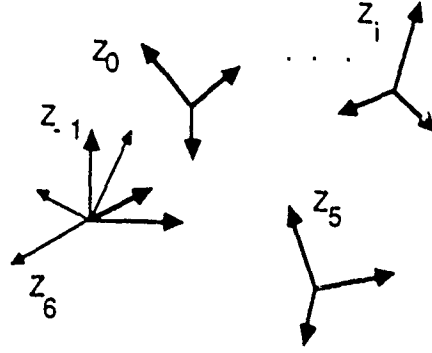
Figure 3-5: Coordinate description of a manipulator under point contact.

coordinates is arbitrary with respect to the 0 coordinates, so θ_0^{off} and α_0 are taken as arbitrary constants. Moreover, the orientation of the end effector coordinates is arbitrary with respect to the 5 coordinates; hence α_6 (or more generally α_n) is taken as an arbitrary constant also. Finally, it is necessary to specify one length parameter; for the theorem below, we select $a_0 = -1$.

To incorporate just the position equations, we redefine $\underline{x}_c^i = p_c^i = 0$ from (3.3) and $\Delta \underline{x}_c^i = (dx_c^i, dy_c^i, dz_c^i)$ from (3.7). The constant parameters θ_0^{off}, α_0, α_n, and a_0 are removed from $\underline{\varphi}$. Then $\mathcal{X}$, $\mathcal{F}$, $\mathcal{C}$, and $\mathbf{C}^i$ are redefined in (3.4)-(3.5) and (3.8) to reflect the reduced dimensions. In particular, each column of each Jacobian in (3.12) contains only the top vector or first three rows.

$$\left(\mathbf{J}_a^i\right)_j = x_j^i, \quad \left(\mathbf{J}_.^i\right)_j = z_{j-1}^i, \quad \left(\mathbf{J}_\theta^i\right)_j = z_{j-1}^i \times b_j^i, \quad \left(\mathbf{J}_\alpha^i\right)_j = x_j^i \times b_{j+1}^i \qquad (3.27)$$

These columns are now interpreted as *partial velocity* vectors with respect to the parameters instead of as screw coordinates [52]. Notice that we have used up three kinematic equations in order to eliminate the unmeasured orientation DOFs of the endpoint. The identification procedure can then be applied as before.

As before, the identifiability of the parameters depends on the linear dependence of the columns of the Jacobian $\mathbf{C}^i$. Because of the form of the columns in (3.27), a stronger identifiability condition is derived than (3.15).

Theorem 4 (Point-Contact Identifiability) *The parameters $\underline{\varphi}$ are unidentifiable*

47

Joint	$\underline{s}$ (m)	$\underline{a}$ (m)	$\underline{\alpha}$ (rad)	$\underline{\theta}^{off}$ (rad)
0	1.694	0.837	3.600*	0.000*
1	1.622	-0.627	-0.553	0.100
2	1.000*	-0.100	0.930	0.090
3	-0.430	-0.430	2.040	0.100
4	0.540	-0.600	-0.150	0.050
5	-0.560	-0.550	1.350	0.040
6	-1.693	0.711	-1.860*	1.700

Table 3.5: The initial D-H parameters of a 6-DOF manipulator under point contact.

Joint	$\underline{s}$ (m)	$\underline{a}$ (m)	$\underline{\alpha}$ (rad)	$\underline{\theta}^{off}$ (rad)
0	1.594	0.737	3.600*	0.000*
1	1.722	-0.527	-0.503	0.120
2	1.000*	0.000	0.530	0.000
3	-0.330	-0.330	2.300	0.000
4	0.440	-0.440	-0.900	0.000
5	-0.660	-0.550	1.200	0.000
6	-1.793	0.911	-1.860*	1.825

Table 3.6: The actual/calibrated D-H parameters of a 6-DOF manipulator under point contact.

if and only if there is a constant linear relation among the partial velocity vectors for all configurations. That is, there exist constants c_j^k, $k = 1, \ldots, 4$, not all zero, such that

$$0 = \sum_{j=0}^{n} c_j^1 z_{j-1}^i + \sum_{j=1}^{n} c_j^2 z_{j-1}^i \times b_j^i + c_j^3 x_j^i + \sum_{j=1}^{n-1} c_j^4 x_j^i \times b_{j+1}^i \qquad (3.28)$$

for all $i = 1, \ldots, m$.

Again, trivial modifications to the theorem can be made if a different length parameter than a_0 is fixed.

We now simulate a 6-DOF manipulator under point contact; the actual parameters are given in Table 3.6. The arbitrary constant parameters are marked with a *, and in particular we have chosen $s_2 = 1$ as the fixed length parameter. This entire mechanism was simulated in 30 distinct configurations ($\theta_1, \theta_2, \theta_3 = 0$ to 0.5 rad), starting with the initial guesses in Table 3.5. The parameters in Table 3.6 were recovered to within
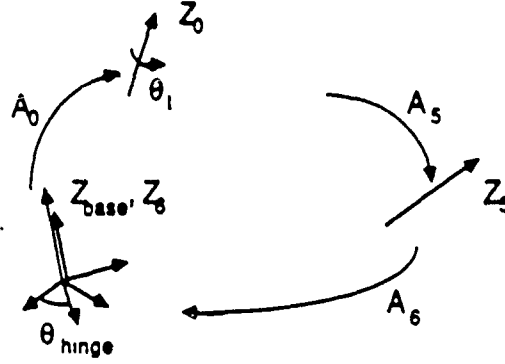
Figure 3-6: The coordinate description of a manipulator connected to a hinge joint.

four decimal places.

3.4.2 Opening a Door

The hinge joints of a door define a rotary axis. Since the endpoint coordinates are arbitrary, it is convenient to make z_n^i coincident with the door's axis (Figure 3-6). We also position the base coordinates at the endpoint coordinates, and let z_{-1}^i coincide with z_n^i. The door hinge angle θ_z^i measured about z_{-1}^i is unknown, and the orientation equation relating to this rotation must be eliminated from the calibration procedure.

To begin, the position equations are the same as before: $\mathbf{p}_c^i = 0$ from (3.3) and $\Delta \mathbf{p}^i = (dx_c^i, dy_c^i, dz_c^i)$ from (3.7). The endpoint orientation is given by

$$\mathbf{R}_c^i = \mathbf{R}_x(\partial x_c^i)\mathbf{R}_y(\partial y_c^i)\mathbf{R}_z(\theta_z^i) \tag{3.29}$$

where ∂x_c^i and ∂y_c^i are infinitesimal and θ_z^i is finite. Expanding the first column of (3.29) and neglecting the second order terms, one finds that $\theta_z^i = atan2(\mathbf{R}_{c(2,1)}^i, \mathbf{R}_{c(1,1)}^i)$, where the indices denote the elements of the rotation matrix $\mathbf{R}_c^i$. The desired variations ∂x_c^i and ∂y_c^i are extracted from $\mathbf{R}_c^i \mathbf{R}_z(\theta_z^i)^T = \mathbf{R}_x(\partial x_c^i)\mathbf{R}_y(\partial y_c^i)$. The computed endpoint location is then given by the 5-vector $\underline{x}_c^i = (dx_c^i, dy_c^i, dz_c^i, \partial x_c^i, \partial y_c^i)$. Thus one kinematic equation has been used up in order to eliminate the unmeasured door hinge angle.

As before, one length parameter needs to be specified, say $a_1 = -1$. Since z_{-1}^i . aligns with the door hinge and with z_n^i, then θ_0^{off} and θ_0 can be arbitrarily set to zero. $\underline{\varphi}$ is adjusted to eliminate a_1 and θ_0^{off}. Finally, $\mathcal{X}, \mathcal{F}, \mathcal{C}$, and $\mathbf{C}^i$ are redefined in

49

Joint	$\underline{s}$ (m)	$\underline{a}$ (m)	$\underline{\alpha}$ (rad)	θ^{off} (rad)
0	1.694	0.837	3.774	*
1	1.622	-0.627	-0.553	0.080
2	1.000	-0.100	0.930	0.090
3	-0.430	-0.430	2.040	0.900
4	0.540	-0.600	-0.150	0.050
5	-0.560	-0.550	1.350	0.040
6	-1.693	0.711	-1.859	1.400

Table 3.7: The initial D-H parameters for a 6-DOF manipulator opening a door.

Joint	$\underline{s}$ (m)	$\underline{a}$ (m)	$\underline{\alpha}$ (rad)	θ^{off} (rad)
0	1.594	0.737	3.604	*
1	1.722	-0.527	-0.503	0.000
2	1.000	0.000	0.530	0.000
3	-0.330	-0.330	2.300	0.000
4	0.440	-0.440	-0.900	0.000
5	-0.660	-0.550	1.200	0.000
6	-1.793	0.911	-1.459	1.825

Table 3.8: The actual/calibrated D-H parameters of a 6-DOF manipulator opening a door.

(3.4)-(3.5) and (3.8) to reflect the reduced dimensions of $\underline{x}_c^i$. The kinematic calibration procedure may then be applied.

Once again, identifiability is related to the rank of $\mathbf{C}^i$. Theorem 3 applies to the door-opening case, as do the various sources of parameter ambiguity discussed in the previous sections.

Next we simulate a 6-DOF manipulator grasping a door with a hinge joint. The D-H parameters are given in Table 3.8; arbitrary parameters are marked by a *, including the fixed length $s_3 = 1$. This entire mechanism was simulated in 40 distinct configurations ($\theta_1 = 0$ to 0.5 rad), starting with the initial guesses in Table 3.7. The parameters in Table 3.8 were recovered to within four decimal places.

3.4.3 Identifying Arbitrary Task Kinematics

We now discuss how the algorithm presented for closed-loop kinematic calibration readily generalizes to identifying arbitrary task kinematics. As mentioned earlier, the chief difficulty is eliminating the unknown DOFs from the environment kinematics. This may be achieved by determining the unknown DOFs in terms of the known ones (and the kinematic parameters). For instance, in calibrating a system comprised of a robot opening a door with a handle, both the door hinge angle and the handle angle may be determined in terms of the known manipulator joint angles. Once all of the DOFs are determined, the iterative identification algorithm presented above is directly applicable to identifying the kinematic parameters. In particular, the over-determined system of equations (3.8) may be solved by the iterative Levenberg-Marquardt algorithm.

Determining the unknown DOFs may proceed as follows: (a) using the nominal model of the robot, compute the location of the endpoint at a specific configuration, then (b) notice that this endpoint also locates the endpoint of the environment kinematic chain, and finally (c) using the nominal kinematics of the environment calculate the inverse kinematic solution of the endpoint position given in step (a). The resulting joint angles are the unknown DOFs. The inverse kinematics of step (c) must in general be performed iteratively (for example, with [49]). Notice that a nominal model of the kinematics is required. Each iteration of kinematic calibration algorithm presented in Section 3.3 improves the nominal model. Thus, the above determination of joint angles must be performed anew for each step of the kinematic calibration iteration.

3.5 Discussion

We have presented a new kinematic calibration method that does not require endpoint measurements or precision points. By forming manipulators into mobile closed kinematic chains, we have shown that consistency conditions in the kinematic loop closure equations are adequate to calibrate the manipulator from joint angle readings

alone. This closed-loop kinematic calibration method is an adaptation of an iterative least squares algorithm used in calibrating open chain manipulators.

Identifiability of the kinematic parameters of the closed loop was reduced to inspecting the rank of the Jacobian matrix C. Rank degeneracies were in turn studied with the screw coordinate interpretation of the columns of the Jacobians $\mathbf{C}^i$. Specifically, a requirement that there be no constant linear relation among the local link $\mathbf{x}_j^i$ and $\mathbf{z}_j^i$ axes accounts for all singularities when there are no passive DOFs. Closed mechanism with passive DOFs must be studied on a case by case basis for identifiability.

Three tasks were studied in detail: (1) fixed endpoint, (2) point contact, and (3) opening a door. Nevertheless, the method readily generalizes to a large class of robot tasks. The main requirement is that there be positive mobility in the closed chain; in general, the sum of manipulator DOFs plus the passive DOFs of the endpoint constraint must exceed 6. Fixed endpoint constraints generally require redundant arms to achieve positive mobility. An equivalent scenario is two manipulators rigidly attached at their endpoints with combined DOFs greater than 6; thus two non-redundant arms could be calibrated together. When passive endpoint constraints are allowed, single non-redundant arms may be calibrated as well; for example, under point contact the manipulator only requires 4 DOFs. In principle, up to 5 passive DOFs can be allowed in the endpoint. For every passive DOF, one of the six kinematic loop closure equations is used up to eliminate the unknown joint angle; this procedure is akin to mechanism synthesis.

In our method, it is necessary to specify one length parameter to scale the mechanism. An independent means for measuring this parameter is required. This is a feature of other kinematic calibration methods as well, such as those using theodolites [53].

Another issue with our method is how to handle the forces encountered when moving the manipulator with an inaccurate kinematic model under endpoint constraints. It is beyond the scope of this thesis to present a detailed solution, but an appropriate force control procedure must be implemented. The task is made easier if the joint

actuation is inherently compliant. For example, one could drive only as many joints as there are degrees of mobility in the loop. Alternatively, one could drive all joints using the initial guess at the kinematic parameters to calculate the constrained joint motion, and then rely on the joint compliance to allow for error in the commanded joint trajectories. Though more complicated, this latter method is better, as the former method could lead to the drive joints jamming at singularities. In Chapter 4 we apply the method to calibrating two fingers of the Utah-MIT Dextrous Hand which are rigidly attached at the endpoints to form a closed-loop mechanism with 8 DOFs (see also [54]); the fingers are moved manually as a simple remedy in this particular case.

Although the joint offsets $\underline{\theta}^{off}$ were the only non-geometric parameters modeled in this chapter, in principle more complicated non-geometric joint models could be calibrated. For example, in Chapter 4 (see also [54]) an additional scaling factor for the joint angle sensors is required and can also be identified.

Our closed-loop method to kinematic calibration represents a departure from the typical dichotomy found in robotics between model building and task performance. The removal of this dichotomy may generalize to other problem areas in robotics. In this chapter the models of the task and the manipulator are improved *while* performing the task. In Chapter 5 we will show how an uncalibrated stereo vision system can be calibrated together with an uncalibrated manipulator (see also [55]). Thus we feel that our approach is a step towards true autonomy: no special precalibrated endpoint measurement device — or external 'teacher' — is needed.

Chapter 4

Closed-Loop Kinematic Calibration of the Utah-MIT Dextrous Hand

4.1 Introduction

The previous chapter proposed a technique for calibrating closed-loop kinematic chains formed by dual or redundant manipulators. This technique differs from conventional calibration schemes [34] in that it does not require special endpoint-sensing equipment. The present work will experimentally verify this closed-loop calibration technique by calibrating the Utah-MIT Dextrous Hand [56] [57].

Briefly, the closed-loop kinematic calibration method is described as follows. Consider a finger of the hand system opposing the thumb, such that the fingertips are rigidly connected (Figure 4-1). As each finger has four degrees of freedom (DOF) an 8-DOF closed loop is formed; this loop has in general a mobility of two. Observe that fixing only two joint angles uniquely defines the configuration of this mechanism (except for the possibility of multiple inverse kinematic solutions). Thus, the other six joint angle sensors are *redundant*. This sensor redundancy may be exploited to estimate the kinematic parameters. Specifically, the loop consistency equations for a given configuration give three position and three orientation equations containing

54
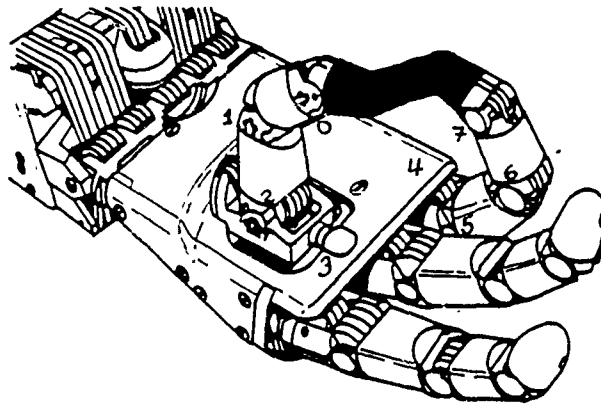
Figure 4-1: Hand with two fingers opposed, adapted from [4].

the unknown kinematic parameters. Moving the fingers into different configurations while maintaining the same contact condition provides six additional equations per pose. Potentially these equations can be solved for the kinematic parameters, that is provided certain identifiability conditions defined in Chapter 3 are met.

The chapter is organized as follows: (1) outline of calibration procedure, (2) experimental results, and (3) discussion of future work. Several modifications are made to method described in Chapter 3. Initial experiments revealed that the joint angles of the hand not only have joint offsets, but also joint scale factors that are difficult to determine a priori. For this reason the algorithm is augmented to include the identification of these joint scale factors. Perhaps the most difficult task in any kinematic calibration procedure is determining the initial guess at the kinematic parameters, particularly for the base and fingertip transformations. As a partial solution to this problem, the more accurately known parameters are fixed while the others are first estimated. Finally, singular value decomposition provides a means of dealing with parameter ambiguity, and also conveniently produces a measure of parameter observability.

4.2 Method

4.2.1 Manipulator Kinematics

Geometric Parameters

Consider two fingers of the hand connected together rigidly at their tips (i.e., the thumb opposed to a finger); see Figure 4-1. This closed kinematic chain has $n_f = 8$ degrees of freedom. Locate a reference (base) coordinate frame coincident with the last joint of the thumb; then number the joints proceeding from that distal joint to the palm, and then back out to the tip of the finger, as in Figure 4-1. Let the 4×4 homogeneous transformation A_j from link j to link $(j-1)$ be defined by the Denavit-Hartenberg (D-H) convention[40] given in Figure 3-2 and symbolically as:

$$A_j = Rot(z, \theta'_j)Trans(z, s_j)Trans(x, a_j)Rot(x, \alpha_j) \qquad (4.1)$$

where the notation $Rot(x, \phi)$ indicates a rotation about an axis x by ϕ and $Trans(x, a)$ indicates a translation along an axis x by a.

Since the D-H s parameter is not uniquely defined for consecutive parallel axes the following Hayati convention[46] (see Figure 4-2) is employed for such axes (i.e., for joints 0, 1, 3, 5 and 6):

$$A_j = Rot(z, \theta'_j)Trans(x, s_j)Rot(x, a_j)Rot(y, \alpha_j) \qquad (4.2)$$

The position of the last link is computed by a sequence of these homogeneous transformations:

$$T_c = A_1 A_2 ... A_{n_f} \qquad (4.3)$$

This homogeneous matrix representation of the endpoint is equivalent to the position vector (3.1) and rotation matrix (3.2) representation used in Chapter 3.

The goal is to identify the geometric parameters s_j, α_j and a_j, and also any

56
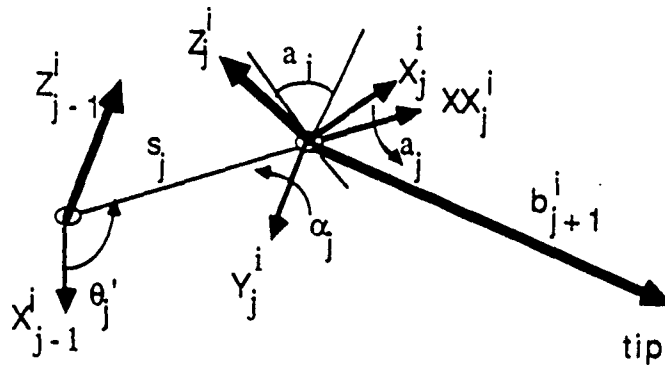
Figure 4-2: Hayati coordinates, and intermediate x-axis xx_j.

non-geometric parameters that may be included in the kinematic model.

Non-Geometric Parameters

The non-geometric effects on the kinematic model potentially include bearing play and joint angle sensor error. Although parametric models of both of these processes may be included we choose to only model joint angle sensor error. In particular, the D-H joint angle is presumed to be related to the sensor reading as

$$\theta'_j = k_j \theta_j + \theta_j^{off} \tag{4.4}$$

Thus, we wish to identify the constant joint angle offset θ_j^{off}, and the joint scale factor k_j. The joint scale gives the calibration factor for the measured electronic signal from the Hall effect joint sensors.

4.2.2 Unidentifiable and Identifiable Parameters

If we try to identify all the k_i there is a trivial solution $k_i = 0$, which will satisfy any set of joint angle data. To avoid this difficulty, fix a joint scale factor that can be measured independently. For the hand we choose $k_7 = 1.0$. Likewise, one link length must be known. This length defines the length scale of the closed mechanism. For example, in Section 4.3 we set $s_0 = -1.3$.

All of the potentially identifiable kinematic parameters are placed into a single

Figure 4-3: Coordinate assignment for loop of two fingers attached at their endpoints.

vector:

$$\underline{\varphi} = (\underline{\theta}_{off}^T, \underline{s}^T, \underline{a}^T, \underline{\alpha}^T, \underline{k}^T)^T \tag{4.5}$$

where $\underline{s} = (s_1, s_2, ...)^T$ etc.

4.2.3 Base Coordinate Assignment and Endpoint Location

The two connected fingertips may be viewed as a single effective endpoint link that connects the most distal joint of the finger to the first joint of the kinematic chain (i.e., the most distal joint of the thumb); see Figure 4-3. Defined as such, the endpoint always has zero orientation and position relative to the base coordinates (i.e., those coordinates that were defined to be aligned with the thumb's most distal joint axis). Notice that in addition to the robot kinematic parameters we will also identify the D-H parameters of this effective link which completes the loop.

4.2.4 Endpoint Location Error Calculation

With a sufficiently good initial parameter estimate the computed endpoint location, T_c, differs only slightly from zero (the base coordinates). The endpoint error computations can therefore be simplified as follows. Let the computed position (i.e., the fourth column of T_c) be represented by $(dx_c, dy_c, dz_c)^T$. Similarly, let the calculated orientation R_c (that is, the upper left 3×3 matrix of T_c) be represented by

infinitesimal xyz-Euler rotations:

$$R_x(\partial x_c)R_y(\partial y_c)R_z(\partial z_c) \approx \begin{bmatrix} 1 & -\partial z_c & \partial y_c \\ \partial z_c & 1 & -\partial x_c \\ -\partial y_c & \partial x_c & 1 \end{bmatrix} \qquad (4.6)$$

where the right hand side of (4.6) is computed by directly expanding the left hand side and ignoring second order differential terms. Thus, the modeled endpoint location, evaluated at the *ith* joint configuration $\underline{\theta}^i$, is represented by a six vector:

$$\underline{x}_c^i = \underline{x}_c^i(\underline{\theta}^i, \underline{\varphi}) = (dx_c, dy_c, dz_c, \partial x_c, \partial y_c, \partial z_c)^T \qquad (4.7)$$

directly computed from T_c. Thus, the explicit form of (3.3) is given by (4.7).

As stated, the actual position and orientation of the endpoint is taken to be zero, thus the endpoint error is given by (3.18).

4.2.5   Iterative Identification

Iterative identification may proceed as in Section 3.2.2.

Differential Kinematics

At the *ith* joint configuration $\underline{\theta}^i$ the first differential of (4.7) is given by a similar relation to (3.8):

$$\Delta \underline{x}^i = \frac{\partial \underline{x}_c^i}{\partial \underline{\theta}}\Delta\underline{\theta} + \frac{\partial \underline{x}_c^i}{\partial \underline{s}}\Delta\underline{s} + \frac{\partial \underline{x}_c^i}{\partial \underline{a}}\Delta\underline{a} + \frac{\partial \underline{x}_c^i}{\partial \underline{\alpha}}\Delta\underline{\alpha} + \frac{\partial \underline{x}_c^i}{\partial \underline{k}}\Delta\underline{k} \qquad (4.8)$$

where again $\Delta\underline{x}^i = 0 - \underline{x}_c^i$ and $\Delta\underline{s} = \underline{s} - \underline{s}^0$ etc. By denoting the combined Jacobian:

$$C^i = \frac{\partial \underline{x}_c^i}{\partial \underline{\varphi}} = \begin{bmatrix} \frac{\partial \underline{x}_c^i}{\partial \underline{\theta}} & \frac{\partial \underline{x}_c^i}{\partial \underline{s}} & \frac{\partial \underline{x}_c^i}{\partial \underline{a}} & \frac{\partial \underline{x}_c^i}{\partial \underline{\alpha}} & \frac{\partial \underline{x}_c^i}{\partial \underline{k}} \end{bmatrix} \qquad (4.9)$$

equation (4.8) may be expressed more concisely as

$$\Delta \underline{x}^i = C^i \Delta \underline{\varphi} \qquad (4.10)$$

Jacobian Calculation

From (3.12) the D-H parameter Jacobian elements are:

$$\text{col}_j \frac{\partial \underline{x}_c^i}{\partial \underline{\theta}} = \begin{bmatrix} \mathbf{z}_{j-1}^i \times \mathbf{b}_j^i \\ \mathbf{z}_{j-1}^i \end{bmatrix}, \quad \text{col}_j \frac{\partial \underline{x}_c^i}{\partial \underline{s}} = \begin{bmatrix} \mathbf{z}_{j-1}^i \\ \mathbf{0} \end{bmatrix} \qquad (4.11)$$

and

$$\text{col}_j \frac{\partial \underline{x}_c^i}{\partial \underline{a}} = \begin{bmatrix} \mathbf{x}_j^i \\ \mathbf{0} \end{bmatrix}, \quad \text{col}_j \frac{\partial \underline{x}_c^i}{\partial \underline{\alpha}} = \begin{bmatrix} \mathbf{x}_j^i \times \mathbf{b}_{j+1}^i \\ \mathbf{x}_j^i \end{bmatrix} \qquad (4.12)$$

The Jacobian columns for parameters of the alternate Hayati convention are found analogously to be:

$$\text{col}_j \frac{\partial \underline{x}_c^i}{\partial \underline{\theta}} = \begin{bmatrix} \mathbf{z}_{j-1}^i \times \mathbf{b}_j^i \\ \mathbf{z}_{j-1}^i \end{bmatrix}, \quad \text{col}_j \frac{\partial \underline{x}_c^i}{\partial \underline{s}} = \begin{bmatrix} \mathbf{xx}_{j-1}^i \\ \mathbf{0} \end{bmatrix} \qquad (4.13)$$

and

$$\text{col}_j \frac{\partial \underline{x}_c^i}{\partial \underline{a}} = \begin{bmatrix} \mathbf{xx}_j^i \times \mathbf{b}_{j+1}^i \\ \mathbf{xx}_j^i \end{bmatrix}, \quad \text{col}_j \frac{\partial \underline{x}_c^i}{\partial \underline{\alpha}} = \begin{bmatrix} \mathbf{y}_j^i \times \mathbf{b}_{j+1}^i \\ \mathbf{y}_j^i \end{bmatrix} \qquad (4.14)$$

where $\mathbf{xx}_j$ stands for the local x-axis just prior to the last rotation about the jth y-axis by α_j (see Figure 4-2).

In both parameter conventions the columns of the Jacobian with respect to the joint scale factors are:

$$\text{col}_j \frac{\partial \underline{x}_c^i}{\partial \underline{k}} = \theta_j{}^i \begin{bmatrix} \mathbf{z}_{j-1}^i \times \mathbf{b}_j^i \\ \mathbf{z}_{j-1}^i \end{bmatrix} \qquad (4.15)$$

4.2.6 Data Collection and Parameter Estimation

As in the previous chapter, a series of n configurations of the actual mechanism provides n sets of joint angle measurements $\underline{\theta}^i$, and $6n$ equations of the form (4.10).

60

With the C^i defined in (4.9) redefine C as

$$C = \begin{bmatrix} C^1 \\ \cdot \\ C^n \end{bmatrix} \qquad (4.16)$$

A solution may be found iteratively using the parameter error estimates (3.6), and $\underline{\varphi} = \underline{\varphi}_0 + \Delta\underline{\varphi}$.

As mentioned in Chapter 3, during iteration the matrix $C^T C$ may become singular at an intermediate parameter set, even though the final parameter set does not have a singularity. To avoid the problem the least squares criteria is modified as in Section 3.2 to be:

$$LS' = (\Delta\underline{\mathcal{X}} - C\Delta\underline{\varphi})^T(\Delta\underline{\mathcal{X}} - C\Delta\underline{\varphi}) + \lambda(\Delta\underline{\varphi})^T(\Delta\underline{\varphi}) \qquad (4.17)$$

In contrast to Chapter 3, this criteria is minimized here by using the singular value decomposition (SVD) of C, zeroing singular values that are less that p percent of the maximum singular value, and then implementing the generalized inverse from the SVD matrices [58]. The value of p implicitly gives λ, and it is set high (e.g., $p = 5$ percent) initially and reduced once convergence occurs.

If the kinematics are over-parameterized for the collected joint angle data then C will always have zero singular values. The number of near zero singular values indicates the number of non-independent parameters.

Two other variations of the original algorithm are as follows. Th poorly known parameters (base and tip transformations) are first estimated by assuming that the finger parameters are correct. Then all parameters are allowed to freely vary, giving the final results. Also, it is often found useful to check that the present update to the parameters improves the endpoint positioning error. If it does not then the parameter update is repeatedly halved, until the endpoint error improves (see [58]).

Joint	θ^{off} (rad)	s (in)	a (in)	α (rad)	k
0*	0.0000 ~	-1.3000	0.0000	0.0000	1.0000
1*	0.0000	-1.7000	0.0000	0.0000	1.0000
2	0.0000	0.0000	-0.4500	1.5708	1.0000
3*	-1.5708~	2.1200~	0.4094~	0.2080~	1.0000
4	0.0000~	2.2500~	0.6000~	-1.5708	1.0000
5*	0.0000~	1.7000	0.0000	0.0000	1.0000
6*	0.0000	1.3000	0.0000	0.0000	1.0000
7	3.1415~	-0.5000~	-1.0000~	-0.2618~	1.0000

Table 4.1: 8 DOF mechanism. Initial parameters. A * indicates that the parameters are those of the Hayati convention (with the respective units). The parameters marked with a ~ are difficult to measure and were either guessed (for link 7) or roughly calculated from known specifications.

4.3 Experimental Results

Finger three of the hand was opposed to the thumb (finger 0) by rigidly connecting the fingertips (screwed into a common aluminum plate). The nominal kinematic parameters for this 8 DOF closed kinematic chain were taken from [57] and are shown in Table 4.1. The geometric parameters (i.e., the s, a and α parameters) marked with a ~ are difficult to measure independently. The joint angle offset and scale parameters are also not well known. Those geometric parameters *not* marked with a ~ are likely to be more accurate than parameters identified by any identification scheme relying on the limited accuracy of the joint angle sensors.

A series of 200 configurations of the finger/thumb mechanism provided input joint angles for the above identification algorithm. These joint angles are plotted in Figure 4-4. The joint angles for the thumb are negated so that the identified joint axes are in the same direction as defined in [57]. Considerable care was taken to make sure that all joints moved as much as possible.

The calibration was performed with the initial parameters given in Table 4.1, the recorded joint angles, and the two fixed parameters $s_0 = -1.3$ and $k_7 = 1.0$. Convergence of the algorithm required $p = 0.5$ in the SVD based pseudo-inverse, and produced the parameters in Table 4.2.
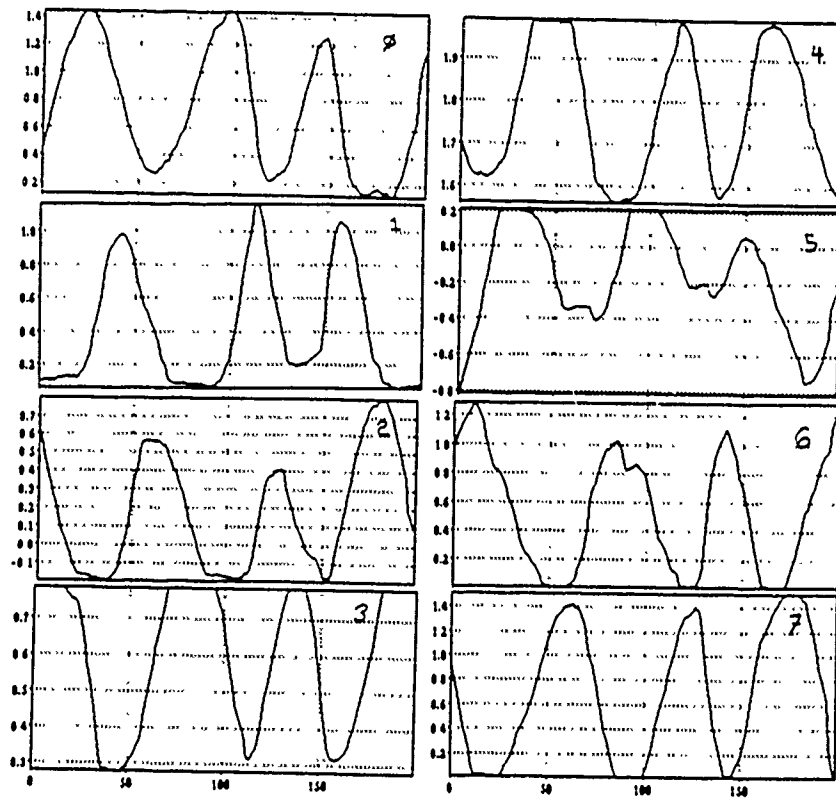
Figure 4-4: Joint angle (rad) vs. pose number for all 8 joints of the thumb and finger.

Joint	θ^{off} (rad)	s (in)	a (in)	α (rad)	k
0*	0.2380	-1.3000	0.0069	0.0668	0.9508
1*	0.0850	-1.5085	-0.1515	-0.0480	0.8596
2	-0.0943	0.1604	-0.3097	1.6207	0.9336
3*	-1.7824	1.8050	0.5755	0.2890	0.9579
4	0.1389	1.7151	1.3356	-1.5836	1.0125
5*	0.5464	1.6307	0.0292	0.0737	0.8577
6*	-0.0425	1.1474	0.1745	0.1260	0.9350
7	3.7552	-0.8322	-1.4377	-0.5631	1.0000

Table 4.2: 8 DOF mechanism. Calibrated parameters. A * indicates that the parameters are those of the Hayati convention (with the respective units).

63

4.3.1 Endpoint Errors

The calibration may be assessed by measuring the error in closure between the fingertips. This error is simply given by the position and orientation vector Δx_c^i for each pose i. Averaging over all poses, the pre-calibration root mean square (RMS) position error was 0.5780 *in* and the RMS orientation error was 0.4645 *rad*. After calibration these errors are reduced to 0.0201 *in* and 0.0290 *rad* respectively.

4.3.2 Geometric Parameter Errors

As stated, the geometric parameters *not* marked with a $\sim$ are likely to be more accurate than the parameters identified by any identification scheme relying on the limited accuracy of the joint angle sensors. These parameter values may be used to check the validity of the calibration algorithm. Comparing these parameters in Tables 4.1 and 4.2 reasonable agreement is seen. The existing miss-match could be partly due to *unmodeled kinematics* such as joint wobble, and other factors caused by machining imprecision. Also, as discussed below, certain parameters may not be uniquely determined from the limited accuracy joint sensor readings.

4.3.3 Non-Geometric Parameter Errors

It is seen from Table 4.2 that the joint angle offsets and scale factors are an important source of error in the kinematic model. The joint offsets marked with a $\sim$ are particularly hard to measure, and indeed show the greatest error. The non-geometric parameters that are more accessible (i.e., θ_j^{off} and k_j for $j = 0, 1, 6$) were carefully re-measured after calibration. This post hoc measurement indicated that these non-geometric parameters were identified more accurately than the initial guesses in Table 4.1.

4.4 Parameter Identifiability

The ratio of the minimum singular value to the maximum singular value of C provides an index of parameter identifiability. This ratio is 0.003, indicating that $C^T C$ is not singular, but is not well conditioned. Thus, all the parameters are theoretically identifiable, but some may be sensitive to measurement noise. As stated, to obtain convergence all the singular values less than 0.5 percent of the maximum singular value were zeroed. This translated into zeroing seven singular values. Thus, for this mechanism, and for this particular joint angle data set, there are seven parameters that are close to linearly dependent upon the other 31 parameters.

It is difficult to determine the geometrical significance of these interdependent parameters. In theory, linear relations between the instantaneous parameter variations may be found from the null space of the Jacobian (the null space is determined by the span of the columns of the matrix V that correspond to (near) zero singular values, where V is part of the SVD of the Jacobian: $C = UDV^T$). It is not clear though how to interpret these first order relations to determine the source of the parameter ambiguities.

Certain parameter dependencies do have a simple explanation though. For example, consider the parameters associated with the most proximal joint of the finger and the most proximal joint of the thumb (joints angles 3 and 4). These two almost parallel joints are partially decoupled from the rest, in the sense that is possible to move them without large movements of the other joints and visa versa. From the data (Figure 4-4) it is seen that joints 2 and 3 move the least (only 0.4 rad). Roughly, these two joints, being perpendicular to the others, move the plane of the rest of the finger/thumb complex. The location of this plane is given by the parameters a_2 and a_4, which are measured along the common normals x_2 and x_4. Unfortunately, these two common normals stay almost parallel for all the data collected (mostly because of the small movement ranges of the joints 2 and 3). In the extreme case where they are fixed to being exactly parallel then the D-H distances a_2 and a_4 along these common normals may vary arbitrarily, as long as the difference $a_2 - a_4$ is kept the same.

Joint	θ^{off} (rad)	s (in)	a (in)	α (rad)	k
-1*	0.0000	1.8050	0.5755	0.2890	N/A
0	0.1389	1.7151	1.3356	-1.5836	1.0125
1*	0.5464	1.6307	0.0292	0.0737	0.8577
2*	-0.0425	1.1474	0.1745	0.1260	0.9350
3	?	?	?	?	1.0000

Table 4.3: Identified finger parameters relative to a palm reference frame, where a * indicates that the parameters are those of the Hayati convention (with the respective units), and a ? means an unknown tip transformation.

Though these common normals are not exactly parallel to one another, we should predict a sensitivity problem in separately identifying a_2 and a_4 from finite precision measurements. See Chapter 3 for a more general discussion of identifiability.

The identifiability of these parameters may be improved by relaxing the endpoint constraint to be a point contact (with the endpoint free to orient arbitrarily) instead of a rigid contact. In the case just discussed the axes x_2 and x_4 would then no longer be constrained to be nearly parallel. The use of a point contact constraint (or a perhaps more elaborate rolling contact constraint) has not yet been attempted because, as yet, we do not have tactile sensors that could be used to assure the point contact. We could build a ball joint to connect the fingertips, but this would not be as general, or natural way of proceeding.

4.5   Common Palm Reference Frame Conversion

Once a finger is calibrated against the thumb, as just described, it is necessary to convert the identified parameters into a reference frame located on the stationary palm of the hand, similar to [57]. This reference frame is the frame labeled 2' in Figure 4-3, that is, the frame found after the rotation of local frame 2 by the joint angle θ_3. The finger's parameters relative to this palm reference are therefore given by the parameters labeled 3 and greater (except θ_3), and are re-written in Table 4.3. The tip transformation is not identified by the above method. It could be identified if a point contact constraint were used instead of a fixed constraint. For practical

Joint	θ^{off} (rad)	s (in)	a (in)	α (rad)	k
0	1.7824	0.0000	0.3097	-1.6207	0.9336
1'	0.0000	-0.1604	0.0000	0.0000	N/A
1*	0.0943	1.5085	0.1515	0.0480	0.8596
2*	-0.0850	1.3000	-0.0069	-0.0668	0.9508
3	?	?	?	?	1.0000

Table 4.4: Identified thumb parameters relative to a palm reference frame, where a * indicates that the parameters are those of the Hayati convention (with the respective units), and a ? means an unknown tip transformation.

purposes the tip D-H parameters are taken to be $\theta^{off} = 0$, $s = 0$, $a = 0.735$ and $\alpha = 0$ [57]. Finally, notice that the parameter set labeled -1 locates the first axis of the finger relative to the thumb.

The thumb parameters are found by following the kinematic chain from the palm frame $2'$ backwards to the 'base' (actually, the fingertips). This simply entails reversing the sign on the respective θ, s, a and α parameters. Also, in the case of the Hayati convention parameters the order of transformations must be changed to:

$$A_j = Rot(z, \theta'_j)Rot(y, \alpha_j)Rot(x, a_j)Trans(x, s_j) \qquad (4.18)$$

The thumb parameters are thus calculated to be those shown in Table 4.4. Notice that an additional s translation, s'_1, is required to provide the translation of -0.1604 along the thumb joint 1 axis.

When the whole calibration procedure is repeated with other fingers opposing the thumb then the identified palm reference frame $2'$ may differ from finger to finger. That is, this frame may be arbitrarily displaced or rotated on the thumb's first joint axis (labeled z_2 in Figures 4). One such reference frame may be defined as the 'common reference frame' and the others related to it. The unknown translation and rotation on z_2 (between any two palm reference frames) may be estimated by locating the thumb in a fixed position and calculating its endpoint in both reference frames. The difference between these endpoint locations gives the two unknown quantities.

4.6 Discussion

Studies investigating the kinematic calibration of the Utah-M$^\mathrm{I}$T Dextrous Hand have been presented. The approach was to use the closed-loop kinematic calibration technique developed in the previous chapter. Several modifications of the original algorithm were necessary. First, it was found that joint angle scale factors had to be included as parameters to be identified. Second, it proved to be important to identify initially the endpoint and palm (base) transformations by assuming the initial guesses at the finger kinematic parameters were correct. This provided improved initial estimates of these parameters, which were otherwise tricky to measure. Once this first step was completed the full scale non-linear parameter calibration technique was used. Finally, SVD provided a convenient way of resolving the parameter ambiguity.

The experimental results indicate that the kinematics of the finger/thumb complex can be identified by the proposed closed-loop kinematic calibration method. Endpoint positioning error was improved by over an order of magnitude. Further, the identified values of the parameters that were also accurately known a priori were in close agreement with these a priori values.

Certain parameters were not uniquely determined from the collected joint angle data. This parameter ambiguity, while clearly not a problem for the particular finger contact situation studied (see RMS error), may cause troubles when the identified kinematics is used for very different finger configurations. The parameter ambiguity is principally due to the lack of joint movement allowed by the fixed constraint (it may also be due to limited joint sensor resolution. and other unmodeled kinematics). In the future we intend to use a point contact constraint (as described in Chapter 3 and [39]). This will produce an 11 DOF mechanism with higher mobility. The natural way to implement this is to use tactile sensors to assure that the fingers stay at a point contact, while allowing arbitrary orientation of the fingertips. This experiment awaits the completion of tactile sensors for the fingers. Other more complex endpoint constraints can also be explored. In fact. the above technique may be extended to identifying the geometry of an object grasped between the fingers (see Chapter 3 and

[38]).

Chapter 5

Autonomous Calibration for Hand-Eye Coordination

5.1 Introduction

Hand-eye coordination is a particularly demanding task because it requires the consistency of two separate sensing systems — the robot manipulator and the stereo vision system. It is the intention in this chapter to address the issue of how these two systems may be calibrated autonomously. By calibration it is meant the determination of the parameters of the internal models of both the camera and arm systems. As in the the previous chapters, the emphasis is on autonomy. Thus, only the robot's *internal* joint angle and camera image sensors are permitted for the calibration.

5.1.1 Motivation

Autonomy is a particularly important property for a robot that must function outside of controlled laboratory conditions. It is inevitable that a robot will have its base moved, links bent, cameras misaligned or be otherwise damaged. In such situations it would be desirable not to have to resort to the use of special purpose calibration equipment to update the model used for robot control. In fact, an ultimate goal would be for the robot to be able to calibrate its internal model in real time.

70

While in certain engineering applications the goal of autonomy may be sacrificed in favor of simplicity, it was pointed out in Chapter 2 that humans have no such choice in calibrating their sensorimotor system. Thus, a second motivation for studying autonomous calibration derives from an interest in understanding the human sensorimotor system.

5.1.2 Previous Research

In the domain of robot *dynamics* autonomous calibration has essentially been achieved, although the kinematics must be assumed to be known (for example [16]). In particular, it is possible to estimate the inertial parameters that define the various links by only using internal joint torque (current), position, and velocity measurements. This idea has actually been made to operate in real time model-based adaptive control schemes[59]. The success of inertial estimation is based on the observation that the suitable combinations of the inertial parameters enter linearly into the dynamic equations.

In contrast, autonomously determining the *static* relationship between the internal joint angle sensors and the manipulator endpoint position — the *kinematic model* – has not been as successful as autonomous dynamic estimation (see review [34]). Typically, researchers have viewed the manipulator as a positioning device — that is, an open-loop kinematic chain. This view demands that the endpoint be measured in addition to the joint angles to infer the kinematic parameters. Therefore, autonomous calibration is not possible.

If instead the manipulator is viewed as a device to interact with the environment then autonomous calibration is possible, as described in Chapter 3 (see also [37][39][38]). The basic observation is that the manipulator may form a *mobile closed-loop kinematic chain* when performing a task. The internal model structure, the knowledge of the type of task constraint, and the internal joint angle measurements collected while in a number of configurations provide enough consistency equations to solve for the kinematic parameters. This technique of closed-loop kinematic calibration is quite general. As an instance that is most relevant to the hand-eye calibration

71

problem, we recall from Chapter 3 that two uncalibrated manipulators may calibrate one another by moving while rigidly grasping (a 0-DOF task) a common object.

Three observations are worth stressing:

- The knowledge of the *task constraint* (e.g., two robots gripping together) replaces the need for an external sensor.

- The *redundancy* of the sensing systems (e.g., two arms) with respect to the task enables the various redundant components to move while performing the same task.

- The *a priori model structure* knowledge allows one to form a number of consistency equations (the kinematics) which may be solved for the kinematic parameters.

These three observations serve as a basis for extending autonomous manipulator calibration to complete hand-eye calibration. First we review relevant *vision* system calibration techniques.

The conventional methodology for camera calibration is to move a number of known precision points into the field of view of the cameras and infer the camera calibration from the given points in space (see review [60]).

One effective approach is to form a look-up table from known rays (obtained from two planes of points in space) to recorded image locations [61][62], and then use splines to do local interpolation. Look-up table approaches need external calibration points, and thus they must be disregarded for autonomous camera calibration.

Various model based approaches have been used for camera calibration. In computer vision and graphics the pinhole camera model has been used extensively [63] [64] [65] [66]. This model may be augmented to account for lens distortions [67] [68] [69]. Since the pinhole camera model is non-linear in its parameters there have been various proposals to make the calibration equations linear [31] [70] [69]. These methods are important because they provide initial guesses at the parameters that general non-linear optimization methods require. Other empirical polynomial interpolation

models have also be used [61] [71] [62], their only advantage being that the parameters enter linearly into the equations.

While the above camera modeling techniques and parameter identification methods are relevant to autonomous calibration, most of this work is predicated on the assumption that there are external calibration points available. There are a few notable exceptions. For example, early photogrammetric engineering work [72] and more recent robotics research [73] have demonstrated that the camera parameters may be recovered by moving the cameras while viewing arbitrary unknown points in space.

Finally, there is a considerable body of literature that addresses the problem of registering the calibrated vision system's coordinates with respect to the robot base (see review [34]). Especially interesting is the work in [74]. Their technique is to determine the camera to hand transformation simultaneously to the robot parameters by viewing an arbitrary fixed point in space. The internal camera parameters are calibrated beforehand by viewing a precision calibration jig.

5.1.3 Towards Autonomous Hand-Eye Calibration

As can be seen the calibration of a robot manipulator/vision system is typically based on a 'divide and conquer' principle. None of these approaches may be made autonomous. Further, there is no guarantee that once the various separately calibrated components are assembled they will be *consistent*. This is a very important point since we know that *models and sensor readings are inaccurate*. We thus propose that a solution is to calibrate the models of the manipulator and two cameras simultaneously while performing the *task* of interest — hand-eye coordination. This may be done as follows.

Recalling the three observations made concerning closed-loop manipulator calibration, it is remarked that hand-eye calibration fits into this framework. First, a manipulator and a vision system may sense the location of the same point in space; and thus, the total robot sensing is *redundant*. Second, if the *task* is defined as the cameras tracking the hand then there is a closed kinematic loop formed. This task constraint replaces the need for external calibration points. Finally, because we may

73

assume a priori knowledge of both the *camera and arm kinematic model structure* it is possible to write out consistency equations of the closed loop in a nv˙ ber of configurations, and thus solve for the parameters. We will develop this idea in what follows.

5.1.4 Outline

As stated, the purpose of this chapter i˙ to extend the closed-loop calibration approach developed for calibrating robot arms o calibrating a complete robot — with a stereo vision system in addition to the m˙ ipulator. The stereo system is assumed to have one axis of rotation per camera, b˙.' is otherwise taken to have an arbitrary geometry.

An uncalibrated stereo cam˙ . system will be made to track a point on the hand of an uncalibrated arm. Therf are at least two distinct approaches to forming the closed-loop calibration equatio˙s. The first is to formulate a model for the manipulator relative to each camera separately, and measure the position error in 2-D image plane coordinates. The calibration would proceed by collecting data from manipulator/camera movements and minimizing the *image plane* error in both cameras. The second approach is to directly model the position of the end effector given by the stereo calculation (from the image data). The calibration can then proceed by minimizing the *end effector error* between the manipulator and stereo models. Of these two approaches the second is chosen because it seems more natural to minimize the *task space* error. In addition, using the second approach enables one to formulate the iterative identification equations more simply; in particular, the manipulator Jacobians developed in Chapter 3 are directly applicable.

It is assumed that the point that is to be tracked may be unambiguously located on both camera images. This generally non-trivial correspondence problem [66] may be solved here because of two additional constraints. First, it is known that the hand is moving relative to the background; therefore, it is possible to disambiguate the hand image from the background. Second, a convenient point that can always be unambiguously located on the hand may be used (e.g., the tip of a pointer).

74

5.2 Model Definitions

5.2.1 Manipulator Model

Consider an arbitrary manipulator with n_f degrees of freedom. Let the 4×4 homogeneous transformation A_j from link j to link $(j-1)$ be defined by the Denavit-Hartenberg (D-H) convention[40] given in Figure 3-2 and (4.1).

For convenience we define the base of the manipulator to coincide with a head referenced coordinate system that is coincident with the left camera's axis of rotation (see next section). The position of the last link is related to these base coordinates by a sequence of D-H transformations defining the kinematic model:

$$T_c = A_0 A_1 A_2 ... A_{n_f} \tag{5.1}$$

Since the model must only locate a point on the end effector the last axis skew is unnecessary, i.e., let $\alpha_{n_f} = 0$.

The position of the point P to be tracked is thus given by the model:

$$\begin{bmatrix} \hat{\underline{x}} \\ 1 \end{bmatrix} = A_0 A_1 A_2 ... A_{n_f} \underline{o} \tag{5.2}$$

where the $\hat{\ }$ emphasizes that it is the position of P *modeled* by the manipulator system, and $\underline{o} = (0,0,0,1)$ is the location of the point P in the hand based reference frame.

All of the *unknown* manipulator kinematic parameters are placed into an array:

$$\hat{\underline{\phi}} = (\underline{\theta}_{off}^T, \underline{s}^T, \underline{a}^T, \underline{\alpha}^T)^T$$

where $\underline{s} = (s_1, s_2, ...)^T$ etc.

5.2.2 Visual System Model

The model of a stereo camera system may be decoupled into a purely geometric part giving the relative orientation and position of the cameras, and a part modeling each camera's projection of points in space. The parameters for these two portions are respectively called the *external* and *internal* camera parameters.

The *internal* camera model used is the standard pinhole camera model [66][75]. More refined parametric models including lens distortions [67][68][69] may also be incorporated without changing the general approach. Let the effective focal point distance be denoted f, and the projected point P in the image plane be given by the pair (u, v). Further define local camera coordinates to have x and y axes parallel to the camera (u, v) grid and have an origin at the focal point (see Figure 5-1). Thus, the coordinates (x_R, y_R, z_R) of a point P expressed in the right camera's local coordinate system is given by the standard projection equations:

$$z_R/(-f_R) = x_R/(u_R + u_R^{off}) = y_R/(v_R + v_R^{off}) \qquad (5.3)$$

Notice that provision is included for unknown offsets (u_R^{off}, v_R^{off}) between the image plane readings and the optical center of the camera. Analogously, the left camera equations are:

$$z_L/(-f_L) = x_L/(u_L + u_L^{off}) = y_L/(v_L + v_L^{off}) \qquad (5.4)$$

The *external* geometric model of the two camera system can be represented by D-H transformations. To distinguish the camera D-H parameters a tilde (e.g., $\tilde{s}_0$) is used. We assume that each camera has one degree of rotation about a fixed axis with a joint angle sensor ($\theta_L = \tilde{\theta}_2$ and $\theta_R = \tilde{\theta}_1$ for the left and right cameras respectively) as defined below. It is convenient to start the kinematic chain at the right camera's local coordinate system — that is, the frame located at the right camera's focal point and having its x and y axes parallel to the right image plane (u, v) coordinate grid. As mentioned in the previous section, the 'base' coordinates are assumed to be located at

the left camera axis of rotation. Thus, the transformation of a point $\underline{x} = (x, y, z, 1)^T$ in base coordinates to the local coordinates of the right camera $\underline{x}_R = (x_R, y_R, z_R, 1)^T$ is given by (see Figure 5-2):

$$\underline{x}_R = \tilde{A}_0 \tilde{A}_1 \underline{x} = T_R^{-1} \underline{x} \tag{5.5}$$

where the only variable parameter is $\tilde{\theta}_1' = \theta_R + \tilde{\theta}_1^{off}$, the right camera rotation. We also define the opposite transform as $\underline{x} = T_R \underline{x}_R$. The analogous left camera coordinate system may be located by a further two D-H transformations (see Figure 5-3):

$$\underline{x} = \tilde{A}_2 \tilde{A}_3 \underline{x}_L = T_L \underline{x}_L \tag{5.6}$$

where the only variable parameter is $\tilde{\theta}_2' = \dot{\theta}_L + \tilde{\theta}_2^{off}$, the left camera rotation. The parameters $\tilde{s}_3$ and $\tilde{\theta}_3$ translate and orient about the left optical axis so that the left coordinate system lines up with the (u, v) image grid, and is located at the focal point. The parameters $\tilde{a}_3$ and $\tilde{\alpha}_3$ are redundant and are taken to be fixed zero quantities. We also define R_R and R_L as the upper 3×3 rotation matrices of T_R and T_L respectively.

To solve the *stereo* camera equations it is convenient to define the vector p from the left focal point to the right focal point, the vector l from the base frame origin to the left focal point, and the two internal parameter vectors as follows:

$$\mathbf{p} = -R_L \mathbf{p}_L \ , \ \begin{bmatrix} \mathbf{p}_L \\ 1 \end{bmatrix} = \tilde{A}_0 \tilde{A}_1 \tilde{A}_2 \tilde{A}_3 \underline{o} \tag{5.7}$$

$$\begin{bmatrix} \mathbf{l} \\ 1 \end{bmatrix} = T_L \underline{o} \tag{5.8}$$

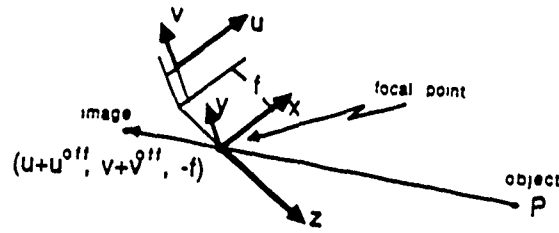$$\mathbf{u}_L = -R_L \begin{bmatrix} u_L + u_L^{off} \\ v_L + v_L^{off} \\ -f_L \end{bmatrix} \tag{5.9}$$

Figure 5-1: *The internal camera model.*

$$\mathbf{u}_R = -R_R \begin{bmatrix} u_R + u_R^{off} \\ v_R + v_R^{off} \\ -f_R \end{bmatrix} \tag{5.10}$$

where again $\underline{o} = (0,0,0,1)^T$. Notice that $\mathbf{u}_L$ and $\mathbf{u}_R$ are respectively vectors from the left and right focal points along the line of sight. Thus, the point P in base coordinates is simply:

$$\tilde{\underline{x}} = c\mathbf{u}_L + \mathbf{l} \tag{5.11}$$

where the $\tilde{}$ emphasizes that it is the position of P modeled by the camera system. The scalar c is given by:

$$c = \frac{\mathbf{u}_R \times \mathbf{u}_L \cdot \mathbf{u}_R \times \mathbf{p}}{\mathbf{u}_R \times \mathbf{u}_L \cdot \mathbf{u}_R \times \mathbf{u}_L} \equiv \Gamma(\mathbf{p}) \tag{5.12}$$

where '$\times$' denotes vector cross product, and '$\cdot$' denotes inner product. The *linear* operator $\Gamma(\cdot)$ has been defined here as it will be useful in Section 5.1.1. All of the *unknown* camera parameters are placed into an array:

$$\tilde{\underline{\phi}} = (\tilde{\underline{\theta}}_{off}^T, \tilde{\underline{s}}^T, \tilde{\underline{a}}^T, \tilde{\underline{\alpha}}^T, \tilde{\imath}^T)^T$$

· where $\tilde{\imath} = (f_R, f_L, u_R^{off}, v_R^{off}, u_L^{off}, v_L^{off})^T$ and $\tilde{\underline{s}} = (\tilde{s}_1, \tilde{s}_2, ...)^T$, etc.
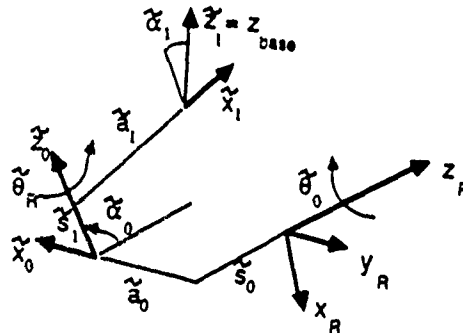
Figure 5-2: *The right camera axes to base D-H transformations. The first transformation locates the line of action of the right camera rotation. The second transformation locates the base coordinate z-axis, which is also the left camera axis of rotation.*
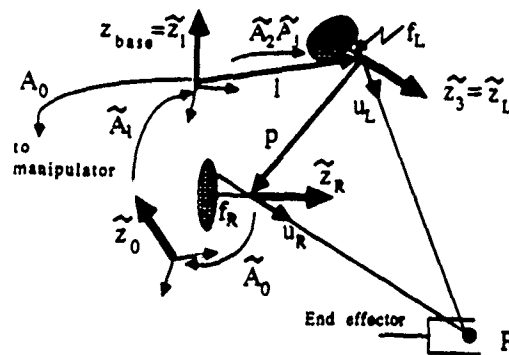

Figure 5-3: *A stereo camera system attached to a manipulator. L and R indicate the left and right cameras. The left and right cameras rotate about $\tilde{z}_1$ and $\tilde{z}_0$ respectively.*

5.2.3 The Closed-Loop Model

Comparing equations (5.11) and (5.2) it is seen that the difference defines the closed-loop kinematic equations of the hand-eye system:

$$0 = \bar{\underline{x}}(\bar{\underline{\phi}}) - \hat{\underline{x}}(\hat{\underline{\phi}}) = \Delta\underline{x}(\underline{\phi}) \tag{5.13}$$

where we have defined $\underline{\phi} = (\hat{\underline{\phi}}^T, \bar{\underline{\phi}}^T)^T$ as a concatenation of all of the parameters to be identified. Note that only *unknown* parameters need be included in $\underline{\phi}$. For example, if all the camera parameters were known and not included in $\underline{\phi}$ then the calibration method described would be a standard manipulator calibration scheme, with endpoint visual sensing.

Also, recall that the base coordinates of the manipulator were defined to correspond to the local coordinates of the left camera rotation. Thus, we see that the manipulator base coordinates are the camera coordinates with axes $\bar{x}_1$, $\bar{y}_1$, and $\bar{z}_1$.

5.3 Model Identification Procedure

As the cameras track the point P at discrete locations the joint angle and image plane sensory information is recorded. The data recorded at the *ith* configuration are placed into a single array:

$$\underline{u}^i = (\theta_1^i, ...\theta_{n_f}^i, \theta_L^i, \theta_R^i, u_L^i, v_L^i, u_R^i, v_R^i)^T \tag{5.14}$$

At the *ith* configuration of the hand, one vector equation of the form (5.13) may be written

$$0 = \Delta\underline{x}^i = \Delta\underline{x}(\underline{u}^i, \underline{\phi}) \tag{5.15}$$

where in additional to the functional dependence on the model parameters the dependence upon the *ith* data array $\underline{u}^i$ is explicitly shown. As a short form $\Delta\underline{x}^i$ will be used, where the functional dependence on the *ith* data array $\underline{u}^i$ will be understood

80

by the super-script i. After moving the hand and cameras into m distinct locations $3\,m$ scalar equations are generated. These equations must be solved in order to find the optimal parameter set $\underline{\phi}$, completing the calibration.

5.3.1 Iterative Identification Technique

We use the same iterative method introduced in Chapter 3 to search for the solution $\underline{\phi}$. By expanding (5.13) with a Taylor's series about an initial guess $\underline{\phi}_0$, and neglecting higher order terms, the following linearized form is obtained:

$$\Delta \underline{x}^i = \left[\frac{\partial \underline{\tilde{x}}^i(\underline{\phi}_0)}{\partial \underline{\phi}} - \frac{\partial \underline{\hat{x}}^i(\underline{\phi}_0)}{\partial \underline{\phi}} \right] \Delta \underline{\phi} = C^i \Delta \underline{\phi} \qquad (5.16)$$

where $\Delta \underline{\phi} = \underline{\phi}_0 - \underline{\phi}$. The Jacobian C^i may also be written as:

$$\left[\frac{\partial \underline{\hat{x}}^i}{\partial \underline{\theta}} \Big| \frac{\partial \underline{\hat{x}}^i}{\partial \underline{s}} \Big| \frac{\partial \underline{\hat{x}}^i}{\partial \underline{a}} \Big| \frac{\partial \underline{\hat{x}}^i}{\partial \underline{\alpha}} \Big| \frac{\partial \underline{\tilde{x}}^i}{\partial \underline{\tilde{\theta}}} \Big| \frac{\partial \underline{\tilde{x}}^i}{\partial \underline{\tilde{s}}} \Big| \frac{\partial \underline{\tilde{x}}^i}{\partial \underline{\tilde{a}}} \Big| \frac{\partial \underline{\tilde{x}}^i}{\partial \underline{\tilde{\alpha}}} \Big| \frac{\partial \underline{\tilde{x}}^i}{\partial \underline{i}} \right]$$

Recall that $\Delta \underline{x}^i$ is the difference between the location of the point P given by the camera model and the manipulator model (computed using ϕ_0). Until the system is calibrated this difference is non-zero.

Place the equations for each of the loop configurations into one array:

$$\Delta \underline{X} = \begin{bmatrix} \Delta \underline{x}^1 \\ \Delta \underline{x}^2 \\ . \\ . \\ \Delta \underline{x}^m \end{bmatrix} = \begin{bmatrix} C^1 \\ C^2 \\ . \\ . \\ C^m \end{bmatrix} \Delta \underline{\phi} = C \Delta \underline{\phi} \qquad (5.17)$$

The Levenberg-Marquardt style non-linear search described in Section 3.2.3 is used to iteratively estimate the parameters. To reiterate, the solution which minimizes the

81

modified least squares criteria $(\Delta\underline{X} - C\Delta\underline{\phi})^T(\Delta\underline{X} - C\Delta\underline{\phi}) + \lambda\Delta\underline{\phi}^T\Delta\underline{\phi}$ is (3.17):

$$\Delta\underline{\phi} = (C^TC + \lambda I)^{-1}C^T\Delta\underline{X} \tag{5.18}$$

The current guess at the parameters is iteratively updated using (5.18) and $\underline{\phi} = \underline{\phi}_0 - \Delta\underline{\phi}$.

Jacobian Calculation

The columns of the manipulator Jacobian were derived in (3.27) to be:

$$\text{col}_j \frac{\partial \hat{\underline{x}}^i}{\partial \underline{a}} = \begin{bmatrix} \mathbf{x}_j \end{bmatrix}, \quad \text{col}_j \frac{\partial \hat{\underline{x}}^i}{\partial \underline{s}} = \begin{bmatrix} \mathbf{z}_{j-1} \end{bmatrix} \tag{5.19}$$

and

$$\text{col}_j \frac{\partial \hat{\underline{x}}^i}{\partial \underline{\theta}} = \begin{bmatrix} \mathbf{z}_{j-1} \times \mathbf{b}_j \end{bmatrix}, \quad \text{col}_j \frac{\partial \hat{\underline{x}}^i}{\partial \underline{\alpha}} = \begin{bmatrix} \mathbf{x}_j \times \mathbf{b}_{j+1} \end{bmatrix} \tag{5.20}$$

The partial derivatives of the camera model may be obtained by similar methods. First concentrate on the length parameters. Notice that from (3.1) the vectors p and l in equations (5.7) and (5.8) may also be written as:

$$-\mathbf{p} = \sum_{j=0}^{3} \tilde{s}_j \tilde{\mathbf{z}}_{j-1} + \tilde{a}_j \tilde{\mathbf{x}}_j \tag{5.21}$$

$$\mathbf{l} = \sum_{j=2}^{3} \tilde{s}_j \tilde{\mathbf{z}}_{j-1} + \tilde{a}_j \tilde{\mathbf{x}}_j \tag{5.22}$$

where $\tilde{\mathbf{z}}$ and $\tilde{\mathbf{x}}$ are local camera z and x axes. Thus, the camera model of point P (5.11) can be re-written to explicitly show the linear dependence of the length parameters:

$$\bar{\underline{x}}^i = -\sum_{j=0}^{1} \tilde{s}_j[\Gamma(\tilde{\mathbf{z}}_{j-1})\mathbf{u}_L] + \tilde{a}_j[\Gamma(\tilde{\mathbf{x}}_j)\mathbf{u}_L] \tag{5.23}$$

$$+ \sum_{j=2}^{3} \tilde{s}_j[\tilde{\mathbf{z}}_{j-1} - \Gamma(\tilde{\mathbf{z}}_{j-1})\mathbf{u}_L] + \tilde{a}_j[\tilde{\mathbf{x}}_j - \Gamma(\tilde{\mathbf{x}}_j)\mathbf{u}_L]$$

where we have taken advantage of the linearity of the operator $\Gamma(\cdot)$ defined in (5.12). It is thus apparent that the column of the Jacobian with respect to a particular length

82

parameter is given by the term in square brackets that it multiplies in the previous equation. For example, the columns with respect to $\bar{s}_1$ and $\bar{s}_2$ are respectively:

$$\text{col}_j \frac{\partial \bar{\underline{x}}^i}{\partial \bar{s}_1} = \left[\ \Gamma(\bar{z}_0)\mathbf{u}_L \ \right], \quad \text{col}_j \frac{\partial \bar{\underline{x}}^i}{\partial \bar{s}_2} = \left[\ \bar{z_1} - \Gamma(\bar{z_1})\mathbf{u}_L \ \right] \tag{5.24}$$

The other parameters may be treated by direct differentiation of (5.11). For example, consider the movement of the point P due to a variation in $\bar{\alpha}_2$:

$$\Delta \underline{x}_\alpha = \Delta \bar{\alpha}_2 [\frac{\partial c}{\partial \bar{\alpha}_2}\mathbf{u}_L + c\bar{x}_2 \times \mathbf{b}_3'] \tag{5.25}$$

where $\mathbf{b}_3' = \mathbf{u}_L$. The term in square brackets in (5.25) is the column of the Jacobian with respect to $\bar{\alpha}_2$. The evaluation of $\partial c/\partial \bar{\alpha}_2$ is straightforward but messy. It involves only the partial derivatives of $\mathbf{u}_L$ and $\mathbf{p}$ which are respectively $\bar{x}_2 \times \mathbf{b}_3'$ and $\bar{x}_2 \times \mathbf{p}$.

5.4 Model Identifiability

Inspecting the form of $\mathcal{C}$ defined in equation (5.17) it is seen that the columns of $\mathcal{C}$ will be independent, and thus the model identifiable (as defined in Chapter 3) if and only if there does not exists some fixed linear relation among the columns of the Jacobians C^i. Using (5.19), (5.20), (5.24) and (5.25) the following condition condition is obtained:

> **Identifiability condition:** identifiability is guaranteed by checking that there be no constant (for all $i = 1..m$ configurations) linear relation among the manipulator local link x_j^i axes and z_j^i axes, their moment vectors $x_j^i \times \mathbf{b}_j^i$ and $z_{j-1}^i \times \mathbf{b}_j^i$, and the camera Jacobian vectors given in the previous section.

The identifiability of the parameters manipulators was studied in detail in previous chapters; thus, we will restrict ourselves to camera related problem situations.

As a first example of unidentifiable parameters, consider the situation when the two camera rotation axes are parallel: $\bar{z}_0^i = \bar{z}_1^i \equiv z^i$. One might suspect a problem

83

because it is well known that the D-H s parameter is poorly defined for serial link kinematic chains with consecutive parallel axes [46]. The columns of the Jacobian (5.24) with respect to $\tilde{s}_1$ and $\tilde{s}_2$ are $\Gamma(\mathbf{z}^i)\mathbf{u}_L^i$ and $\mathbf{z}^i - \Gamma(\mathbf{z}^i)\mathbf{u}_L^i$ respectively. These two vectors are not linearly dependent, so the problem is not as simple as for serial link chains. Notice though that $\bar{\mathbf{z}}_1^i = \mathbf{z}^i$ is the base coordinate's z-axis of the manipulator, and the Jacobian vector with respect to the manipulator parameter s_0 is $\mathbf{z}$. Thus, there exists a linear relation among these three Jacobian vectors:

$$0 = -[\mathbf{z}^i] + [\mathbf{z}^i - \Gamma(\mathbf{z}^i)\mathbf{u}_L^i] + [\Gamma(\mathbf{z}^i)\mathbf{u}_L^i] \quad \forall i \tag{5.26}$$

and by the identifiability condition the parameters s_0, $\tilde{s}_1$ and $\tilde{s}_0$ are not identifiable alone. This becomes a practical problem because it also means that $C^T C$ will be singular in the iteration algorithm (5.18). The solution is to use an alternate coordinate convention for the transformation $\tilde{A}_1$. The Hayati convention [46] developed for manipulators provides such a four parameter system (see Chapter 4). This convention cannot be used for all joints because it too has a similar ambiguous parameter when there are two consecutive perpendicular axes.

As a second instance of unidentifiable parameters, notice that the closed-loop equations (5.13) of the calibrated model may be written to show explicitly the linear dependence of the length parameters:

$$
\begin{aligned}
0 = & -\sum_{j=0}^{1} \tilde{s}_j [\Gamma(\tilde{\mathbf{z}}_{j-1})\mathbf{u}_L] + \tilde{a}_j [\Gamma(\tilde{\mathbf{x}}_j)\mathbf{u}_L] \\
& + \sum_{j=2}^{3} \tilde{s}_j [\tilde{\mathbf{z}}_{j-1} - \Gamma(\tilde{\mathbf{z}}_{j-1})\mathbf{u}_L] + \tilde{a}_j [\tilde{\mathbf{x}}_j - \Gamma(\tilde{\mathbf{x}}_j)\mathbf{u}_L] \\
& - \sum_{j=0}^{n_f} s_j [\mathbf{z}_{j-1}] + a_j [\mathbf{x}_j]
\end{aligned}
\tag{5.27}
$$

where in addition to equations (5.13) and (5.24) the fact that the manipulator length parameters enter linearly into the kinematics has been used. All of the terms in square brackets are columns of the Jacobian C^i, and thus, the closed loop is unidentifiable by the above 'identifiability condition'. Also from (5.27) it is seen that the source of the

84

trouble is that the loop equations may be scaled arbitrarily and still satisfy the joint angle and image plane data. The solution to this problem is to fix one link length arbitrarily. This length determines the units of length. If conventional units, such as a meter, are desired the calibrated vision system merely has to view the desired meter stick and calculate the correction scale factor to its internal units of length.

As a final example of unidentifiable parameters consider the case when the data is not 'persistently exciting'. For instance, if the hand point P is always to move such that it stayed in a plane defined by the right camera axis $\tilde{z}_0^i$, and this plane happened to be coincident with both focal points, then $(u_R^i \times u_L^i) \times \tilde{z}_0^i = 0$ for all i configurations. Thus, $\Gamma(\tilde{z}_0^i) = 0$ and the column of the Jacobian with respect to $\tilde{s}_1$ is identically zero. The parameter $\tilde{s}_1$ is unidentifiable in this situation. Though this scenario is unlikely it does point out the importance of the choice of the configuration data used for calibration. Although perhaps only simulation may determine the optimal data set, it is possible to study the sensitivity of particular parameters [76].

5.5 An Example and Simulation

In order to clarify the general calibration procedure an example is now presented and solved by simulation. Consider the planar 2-DOF manipulator connected to a head mounted stereo system in Figure 5-4. In total there are six degrees of freedom in the system: two manipulator joints, two camera rotations, and two one-dimensional images. The kinematic parameters of interest are in the following order placed into the array $\underline{\phi}$: the three link lengths, three joint angle offsets, three length parameters providing the displacement between cameras coordinates, two camera rotation offsets, and two focal lengths: $\underline{\phi} = (a_0, a_1, a_2, \theta_0, \theta_1^{off}, \theta_2^{off}, \tilde{s}_0, \tilde{a}_1, \tilde{s}_3, \tilde{\theta}_1^{off}, \tilde{\theta}_2^{off}, f_L, f_R)^T$. A simulation of this hand-eye system was performed by using the 'actual' parameter values

$\underline{\phi} = (1.0, 1.0, 1.0, -.8, 0, 0, .1, .36, .1, 0, 0, .05, .05)^T$ (lengths are in meters and angles in radians). Joint angle data was generated by moving the four rotational joints θ_1, θ_2, $\tilde{\theta}_1$, and $\tilde{\theta}_2$ over a trajectory starting at $\theta_1 = 0$, $\theta_2 = 0$, $\tilde{\theta}_1 = 0$, and $\tilde{\theta}_2 = 0$, and covering

Figure 5-4: *Example hand-eye system used for simulation purposes.*

a joint space volume defined by increasing each joint three times in increments of 0.1 rad - i.e., $3 \times 3 \times 3 \times 3 = 81$ distinct configurations. The resulting joint angles and calculated image pairs were used as input to the iterative algorithm given by (5.18). In addition, a preliminary guess of $\underline{\phi}_0 = (1.1, 1.1, 1.1, -.9, .1, .1, .11, .4, .11, .1, .1, .06, .06)^T$ was provided and $\tilde{s}_0$ was fixed at 0.1 m. The algorithm was run until the 'actual' parameters were recovered to within eight decimal places.

5.6   Summary

A general framework for calibrating a manipulator and stereo system for performing the task of hand-eye coordination has been presented. The emphasis has been on autonomous calibration. The vision system was seen to be represented simply with the D-H convention, thus allowing a unification of manipulator and camera model notation. The vector based derivation of the columns of the closed-loop Jacobian enabled an identifiability condition to be derived. As examples of the application of this condition the parallel axis problem, the length parameter scale problem, and the data 'persistency of excitation' problem were all discussed. The iterative parameter search algorithm introduced in Chapter 3 was generalized and demonstrated in simulation.

Chapter 6

Relevance of Robot Calibration to Human Motor Control

The theory of closed-loop kinematic calibration is based on two premises that, though generally taken for granted in robotics, must be justified for human motor control:

- There is need for a task space, and we must therefore learn transformations from our sensors to this 3-D internal representation – a representation distinct from other internal representations such as joint space.

- There are structured internal models representing the sensorimotor transformations. These models are constrained to reflect the physics of our arms and sensors, and do not take on an arbitrary form.

The second premise is not independent of the first; the hypothesis that there is a task space requires a constrained parametric representation of the transformations in order to reasonably explain how the transformations are calibrated (re Section 2.4).

Both of these premises are investigated in the following literature review.

6.1   Internal Models

The notion that there may exist an abstract internal model of the world may be traced back to Descartes [77]. For example, his contemplations of how a blind man

uses a stick for perception led him to the conclusion that we have available a "natural geometry". Without knowing the length of the stick the blind man can triangulate to locate points in space. Descartes did not seem to confront the question of how our arms are calibrated to provide the required hand positions. Nevertheless, he did recognize the need for a geometric reasoning ability, or more specifically an internal model structure.

6.2 Accuracy of Pointing

6.2.1 Accuracy Without Vision

One of the earliest systematic investigations of arm movement revealed that accuracy can be maintained even in the absence of vision [78]. Woodworth concluded that there are two phases to a movement: an impulse phase that moves the arm most of the way to the target, and a current controlled phase that provides final adjustments. During non-visually guided movement the latter phase does not exist and movement is executed in a feedforward manner (with respect to vision).

To further investigate non-visually guided movements Woodworth [78] had subjects repeat a target movement of a certain distance. The repeat movement was performed (1) in a different area of the workspace, (2) with another writing implement, (3) at a different speed, (4) with the wrist instead of the arm, and (5) with a different hand. The results show that across all of these conditions the *extent* of the movement can be reproduced to within approximately 10 percent of the extent of the target movement. When movements were made with different parts of the body (e.g., torso, foot, etc.) accuracy of repeating the extent of movement was still maintained to within 30 percent. Apparently the motor system is able to represent "distances," independently of the sensory modality, which is consistent (but not necessarily the only interpretation) with the hypothesis that an internal 3-D representation of the world exists.

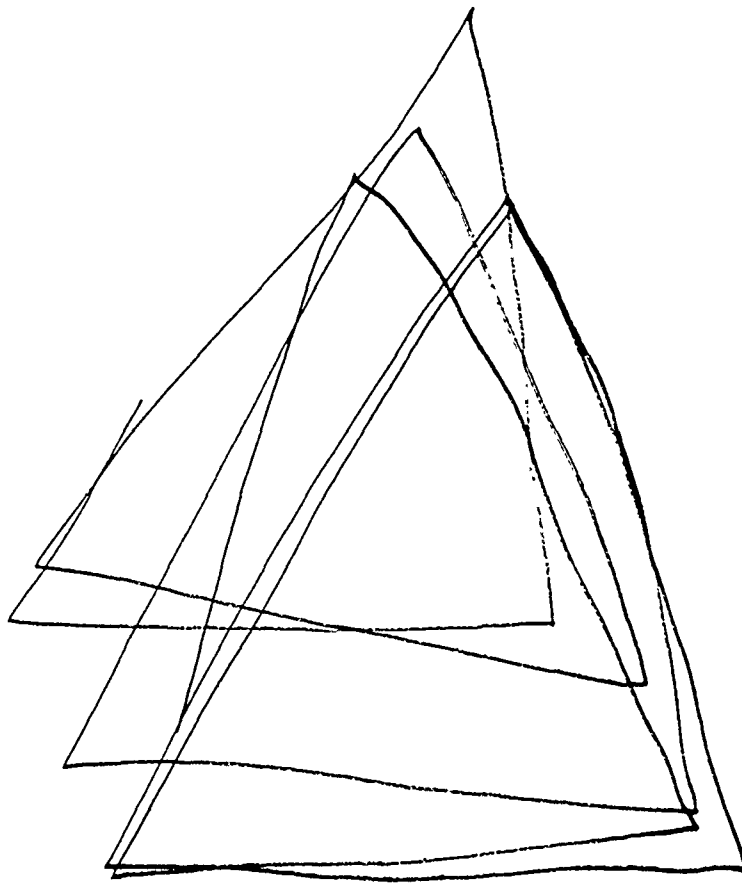Woodworth [78] goes on to argue that the sensation of distance is not purely

Figure 6-1: A subject's attempt at drawing equal overlapping triangles with his eyes closed (actual size). The movement was relatively slow, ≈500 ms per segment.

derived from the endpoint positions in space. This is because, although the extent of movement can be accurately controlled, the absolute positioning is less accurately controlled. For example, in drawing a triangle repeatedly without vision a subject replicates the lengths of the sides well, but the absolute location of the vertices drift substantially [78]. This experiment is easy to repeat; see Figure 6-1.

Fitts [79] also noticed that movement accuracy depends upon other variables than the target position: the initial position, the velocity and the extent of movement all influence accuracy of hitting a target. It may be speculated from these studies that velocity and reafferent force information are used in addition to position information. This conclusion is in line with present knowledge of proprioceptors. Joint capsule sensors seem not as important in providing position sense as spindles, and spindles

provide only velocity and relative length changes in the muscle [4]. Thus, the primary proprioceptive sense must be *integrated* to provide position. Such integration is sensitive to initial conditions, and is prone to drift.

6.2.2 Accuracy and Head Movement

Fitts [79] found that blind pointing accuracy to targets initially seen visually decreased with the angular displacement away from straight ahead (see review [80]). Biguer [81] extended these results to show that the inaccuracy was principally due to the eye rotating laterally more than 30 degrees. If subjects are allowed to move their head pointing accuracy changed in the direction of the head movement. These results only reveal that our joint angle sensors are accurate within limited ranges – not surprising.

6.3 Proprioceptive Distortions

6.3.1 Normal Proprioceptive Distortions

Other work has revealed that the position sense inaccuracies are not just due to sensor limitations. There are systematic distortions in our perception of distance measured by our arms. For example, forced choice studies reveal that distances sensed in the horizontal plane are perceived longer in the radial direction than across the chest [82, page 31-25][83]. Such global distortions cannot be accounted for by a purely memory-based account of the sensory transformations, and is more symptomatic of inaccurate structured models. Unfortunately, these results are difficult to interpret because distance perception is affected by duration, force and ease of movement [78].

6.3.2 Vibration Induced Proprioceptive Distortions

Vibratory stimulation of the arm muscles can produce illusions of movement – presumably from primary spindle excitation. These illusions are so powerful that movement can be perceived to go beyond joint limits and distort parts of the body that the hand is touching. More importantly, such arm muscle vibrations can also create vi-
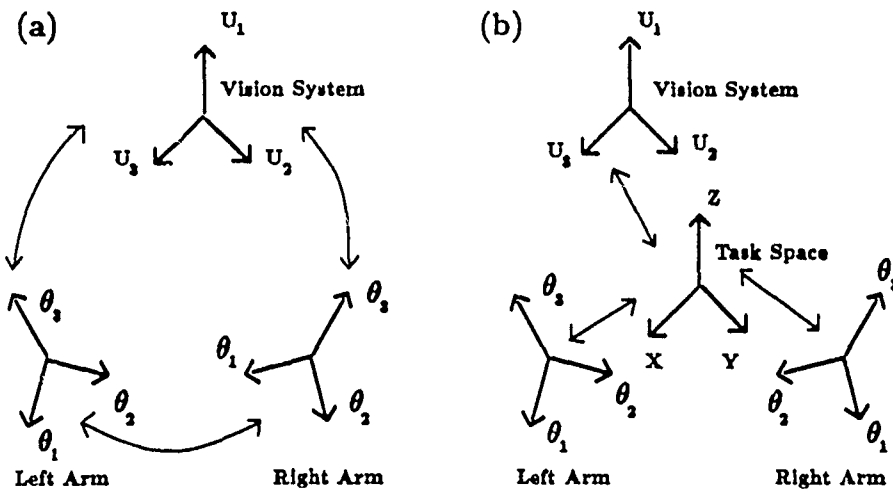
Figure 6-2: (a) Transformations learned by strict association. (b) Transformations with an abstract intermediate reference frame.

sual distortions that are most consistent with a hypothesis that a 3-D body-centered reference frame exists and has rotated [84].

6.3.3 Prism Glasses and Adaptation

The most studied perceptual distortion is that caused by wearing prism glasses (with lateral displacing, rotating, or inverting lenses) [29] [85] [86] [87] [88]. In a typical experiment subjects wear prism glasses and are asked to adapt to manipulating objects with *one* hand under the distorted view. Complete adaption usually occurs if enough time is allowed (hours or days). Two aspects of the recovery are relevant.

(1) The adapted ability generalizes from the learned set of target points. This global generalization supports the notion that the sensory transformations are constrained, as opposed to being built up by strict association. It is not clear, though, whether the constraint is as simple as linear interpolation between neighboring points in space [89], or whether the transformations are due to parametric adaption of global models.

(2) The other aspect of the recovery from prism distortion is that *inter-manual* transfer can occur. Inter-manual transfer refers to the ability to immediately achieve

accurate hand-eye coordination with the hand that was *not* exposed during the adaption period. The inter-manual transfer depends on various factors present during adaption: whether the eye tracks the hand or visa versa, whether the whole arm is seen or not, and whether neck movement is permitted or not [86][87]. However these dependencies are explained, the important conclusion is that inter-manual transfer can occur. If inter-manual transfer never occurred then the simplest interpretation would be that no intermediate coordinate system is used, and direct transformations between the sensors are learned (Figure 6-2a). The finding that transfer does occur suggests that there are separate *modules* for the left arm, the right arm and the head-eye system, and that each module transforms the sensor-space information into a common task space – see Figure 6-2b (there is a possibility here that task space is identical to joint space or retinotopic space). If adaption occurs in the head-eye module then inter-manual transfer is observed. If adaption erroneously occurs in the arm module then inter-manual transfer is not observed.

6.3.4   Teleoperation as a Proprioceptive Distortion

Another approach to studying adaption is to change the arm's geometry. Though this cannot be done easily, an equivalent effect can be achieved by having a human operator control a teleoperated robot [90][91] in a master-slave set-up (the master being an exo-skeleton fit on the human arm). Distortion in the kinematics could be systematically introduced into the slave manipulator. Variables such as whether the shoulder joints intersect, or the link lengths change could be controlled. As with the prism experiments generalization and inter-manual transfer could be studied.

Unfortunately, the teleoperation literature does not contain such studies. There are reports that much training is necessary (months) [92]. A few groups have investigated the problem of using differing geometry master and slave robots. A so called "incompatibility index" has been developed to measure the tolerated mechanical differences between arms [93]. Vertut [90] has found that up to 30 degree orientation mismatch is tolerated by an operator.

I have conducted informal studies of subjects learning to control an X-Y point

on an oscilloscope screen with the elbow angle driving the X-movement and the shoulder angle driving the Y-movement. The hypothesis that the adaption is highly structured predicts that learning fast and accurate hand-eye (oscilloscope-eye) coordination in one region of the workspace should generalize immediately to the rest of the workspace. The two subjects tested took over three hours to learn to accurately move in one quarter of the workspace. By this time they could move "ballistically" to target points. In spite of this long adaption period, the learning immediately generalized to the rest of the workspace – as predicted by the constrained representation hypothesis. These findings are only preliminary, and must be repeated with more degrees of freedom involved, and less dramatic changes in the kinematics.

6.4 Mental Imagery

6.4.1 Reaction Times to Recognize Rotated Objects

The notion of an abstract 3-D reference frame is a premise of the work on mental imagery [94]. A typical result from these studies is that the reaction time in recognizing a rotated object is proportional to the object's degree of orientation away from the target object. The conclusion is that the object is incrementally rotated in an abstract 3-D reference frame until it aligns with the target object. Though plausible, this ability to reason spatially does not prove that a 3-D representation exists. It would be adequate to explain these results with an internal joint-space representation. In fact, in robotics joint space (or more generally, configuration space [95]) is often used for planning. Further, when mental rotation experiments are repeated with pictures of hands used as stimuli, instead of arbitrary objects, the reaction times, oddly enough, obey arm anatomical joint limits [96].

More conclusive evidence for an internal 3-D reference frame comes from studies in which subjects recognized letters drawn on various surfaces of their bodies. The letters – half mirror reversed – were drawn while the body parts were in different configurations. The findings turn out to be consistent with the idea that we do

maintain one or more internal reference frames [97].

6.4.2 Structure from Motion

One of the most persuasive arguments for representing the world in a 3-D task space comes from our ability to recover a rigid body's structure from the motion of moving points [98][99]. Surprisingly, we can recognize a rigid object by only viewing random points projected from a moving object onto a screen, in spite of distance not being preserved between projections of points into different views. Ullman [99] argues that this ability requires an assumption of the object being a rigid body in the 3-D world. Thus, again, it seems that the motor system can represent "distance" in the 3-D world.

A similar situation is encountered in joint space. The distance between points in joint space is not preserved as the points are rigidly moved in the world. To see this you only need to let one point be at your shoulder and the other at your hand. Movement of only the shoulder joint leaves the the distance between these two point fixed in space, but it does change the Euclidean distance calculated in joint space. Thus, none of the natural (intrinsic) sensor coordinates provide a convenient way in which to reason about *metrical* relationships in our 3-D world.

6.5 Neurophysiological Evidence

6.5.1 Direction Coding in the Cortex

There are recent findings that indicate that the firing of populations of neurons in the cortex encode the direction of hand movement – independently of the arm configuration [100] or load [101]. While encouraging, these results are hard to interpret. The finding that cells fire independently of the actual arm configuration or load only indicates that there is an internal representation. It does not imply that this representation is abstract from one of the intrinsic sensor spaces (e.g., retinotopic space).

6.5.2 Muscles and Adaption

It is sometimes possible to explain sensorimotor adaption by muscle or muscle spindle changes (e.g., see [102] and page 189 in [4]). Indeed, active movements seem to be necessary for adaption to prism glasses [29]. While these findings are of eventual interest in explaining the implementation of parametric adaption, they do not explain how the amounts by which to adjust the muscle parameters are calculated. Further, such muscle or spindle adaption can only accommodate simple changes such as joint angle offsets or scales (for example, changing the neck joint angle offset by adjusting the muscle spindles could compensate for lateral displacement prism glasses). These muscle mechanisms cannot compensate for errors in the knowledge of link lengths or joint axis orientations.

6.6 Discussion

In summary, the psychophysical data are not inconsistent with the hypothesis that we can transform sensory information into an abstract 3D task space. Further, from a functional stand point such a 3D task space is attractive: it enables simplicity in representing and recognizing objects in the world. One contribution of this thesis has been to show how structured models may be used to learn transformations to a 3D task space. Another contribution has been to show how hard this learning process really is, even with simplified robotics models. This difficulty of learning must be carefully weighed against the above simplicity arguments for using a 3D task space in the first place.

Part II

Dynamics of the Elbow Joint

During Movement

Chapter 7

Movement Control Theories

7.1 Introduction

Human arm movements are surprisingly stable, fast, and accurate considering the slow neural hardware and large feedback propagation delays. As mentioned in Chapter 1 this performance is partly due to pre-planned feedforward motor drive. We regularly make ballistic movements without visual guidance, and animals are found to still execute normal movement after proprioceptive deafferentation [103]. In the previous chapters the focus was on the learning of feedforward kinematic information. In the following chapters dynamic feedforward compensation is studied. The issue is not how a feedforward dynamic model is learned, but whether such a model exists, and what form it takes.

Another reason for the high performance of the human arm is muscle dynamics. Muscle has a very large dynamic force range. It can produce forces per unit weight exceeding current robotics actuator technology, while it can still produce fine enough forces to control the hand of an eye surgeon. Muscle can also be extremely fast; for example, contraction frequencies of 120 Hz have been observed in some insects [104]. But most importantly, muscle has built in compliance. It has a short range high stiffness, which may function in impact situations such as running [105], and a longer range low stiffness [105], which may allow compliant motion control without excessive active feedback.

97

A series of experiments are described with the goal of characterizing the control system used in arm movement. Feedforward compensation and muscle properties will be shown to be of particular importance.

7.2 Non-Linear Operator Description of Arm Control

The arm control system may take on the general form depicted in Figure 7-1, where it is assumed that the task is to track a joint angle trajectory. The input command is the desired joint angle trajectory $\theta_d(t)$ and the actual output trajectory is $\theta(t)$. The non-linear operator $\mathcal{A}$ represents the feedforward dynamics. It computes the feedforward torque $\tau_d(t) = \mathcal{A}\theta_d(t)$. (The word *operator* is used here in the mathematical sense defined in [106][10]. An operator maps one whole time sequence onto another whole time sequence. In contrast to a function, an operator may represent systems with memory.) The non-linear operator $\mathcal{R}$ represents the feedback system driven by muscle spindles (or other proprioception) with a sensitivity controlled by the gamma drive. Finally, the non-linear operator $\mathcal{P}$ represents the musculo-skeletal plant being controlled. Though the following treatment will be general, it is helpful for understanding to keep in mind the example of a proportional-plus-derivative controller acting on a second order linear system. In this example $\mathcal{P}^{-1} = I d^2/dt^2 + B d/dt + K$, $\mathcal{R} = K_v d/dt + K_p$ and $\mathcal{A} = 0$.

In the absence of external perturbations τ, inspection of Figure 7-1 yields the general input-output relation of:

$$(1 + \mathcal{P}\mathcal{R})\theta = (\mathcal{P}\mathcal{A} + \mathcal{P}\mathcal{R})\theta_d \qquad (7.1)$$

If $\mathcal{A}$ inverts the musculo-skeletal plant dynamics (i.e., $\mathcal{P}\mathcal{A} = 1$) then perfect *feedforward control* is achieved: $\theta = \theta_d$ (except for input signals zeroed by $1 + \mathcal{P}\mathcal{R}$). Also, if the open-loop operator $\mathcal{P}\mathcal{R}$ has a much larger effect than either $\mathcal{P}\mathcal{A}$ or the unity operator 1 on any signal (i.e., the 'gain' [10][106] of $\mathcal{P}\mathcal{R}$, denoted $|\mathcal{P}\mathcal{R}|$, is large),
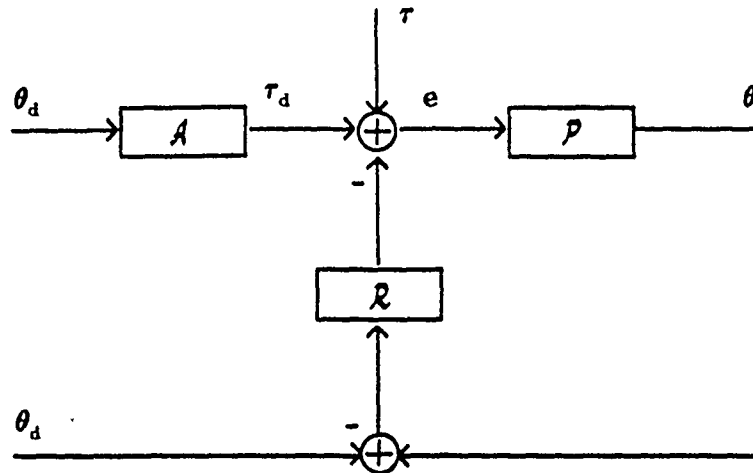
Figure 7-1: General controller for a joint angle trajectory $\theta(t)$.

then *high gain feedback* command following is achieved: $\theta \approx \theta_d$ (except for input signals zeroed by $\mathcal{PR}$). This last item should be used with consideration of the small gains theorem [10][106]: if the open-loop gain $|\mathcal{PR}|$ is less than unity, then stability is always guaranteed. See Section 1.1.1.

7.3 Closed-Loop Dynamics and a Perturbation Model

With human subjects, aside from measuring EMG, the motor system may only be studied by injecting external torques $\tau(t)$ and measuring the joint angles $\theta(t)$. None of the other quantities in Figure 7-1 can be measured. In this section a model of relationship between total torque inputs and joint angle displacement will be developed for the motor system governing the elbow joint. Then a perturbation model will be developed to relate externally applied perturbations to recorded joint angle movements.

7.3.1 Model of Closed-Loop Single Joint Dynamics

The operator expressing the closed-loop dynamics relating total torque inputs to joint angle $\theta(t)$ is easily derived to be $\mathcal{P}_{cl}$ such that:

$$(1 + \mathcal{P}\mathcal{R})\mathcal{P}_{cl} = \mathcal{P} \qquad (7.2)$$

We now derive a more detailed form of $\mathcal{P}_{cl}$. First transform Figure 7-1 into the functionally equivalent form of Figure 7-2:
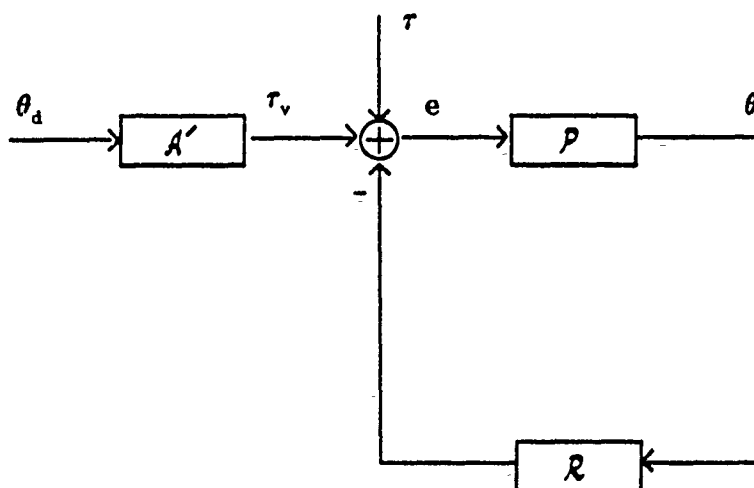
Figure 7-2: Transformed equivalent diagram to Figure 7-1.

where $\mathcal{A}' = \mathcal{A} + \mathcal{R}$, and $\tau_v(t)$ is considered to be the commanded (voluntary) torque input to the feedback controller. Now, include a muscle model as follows.

7.3.2 Model of Muscle

Assuming negligible serial tendon compliance, the single joint musculo-skeletal dynamics $\mathcal{P}$ may be represented by the following general circuit diagram:
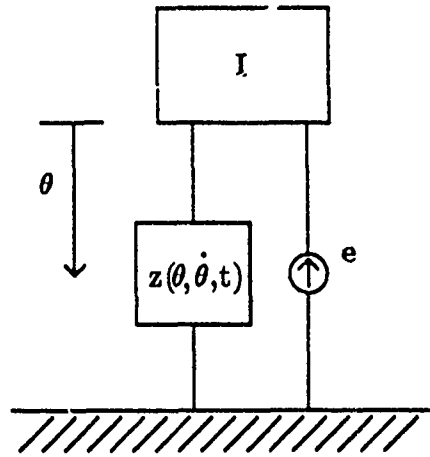
Figure 7-3: Musculo-skeletal dynamics $\mathcal{P}$.

where I is the inertia of the forearm, e is the muscle torque generation mechanism and $z(\theta(t), \dot{\theta}(t), t)$ represents the intrinsic parallel force dynamics of the muscles. Of course, multiple parallel muscles may act on the arm, but their effect can always be reduced to a circuit equivalent to Figure 7-3. Symbolically, Figure 7-3 may be written as:

$$e \;=\; I\ddot{\theta}(t) + z(\theta(t), \dot{\theta}(t), t) \tag{7.3}$$

Defining the new operators $\mathcal{Z}$ and $\mathcal{I}$ such that:

$$\mathcal{Z}\theta(t) \;=\; z(\theta(t), \dot{\theta}(t), t) \tag{7.4}$$

$$\mathcal{I}\theta(t) \;=\; I\ddot{\theta}(t) \tag{7.5}$$

the muscle dynamics may be explicitly included in Figure 7-2 to give Figure 7-4:
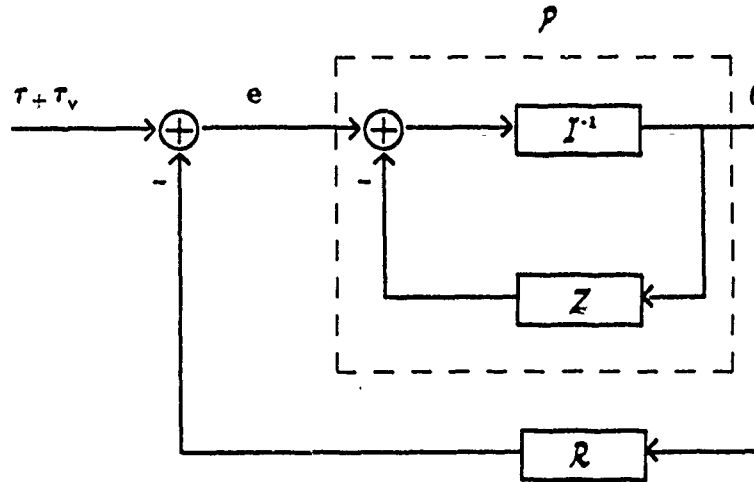
Figure 7-4: Closed-loop dynamics with muscle model explicitly shown.

7.3.3   Equivalent Feedback Model of the Joint Mechanical Properties

A further transformation of the diagram in Figure 7-4 gives the functionally equivalent Figure 7-5:
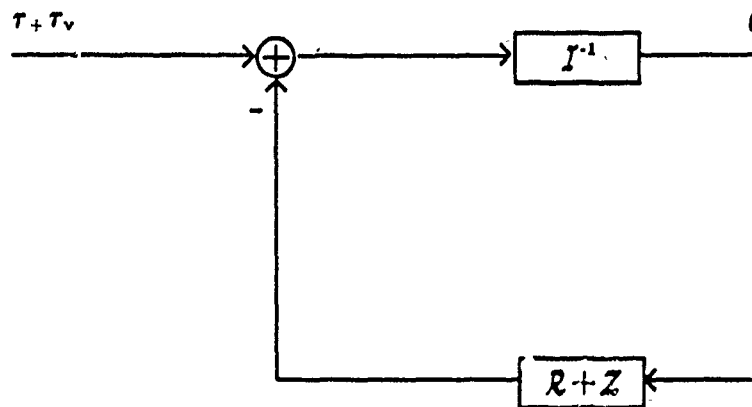
Figure 7-5: Equivalent feedback model of the joint mechanical properties.

or symbolically Figure 7-5 is:

$$0 \; = \; \mathcal{I}\theta(t) + (\mathcal{Z} + \mathcal{R})\theta(t) - \tau_v(t) - \tau(t) \tag{7.6}$$

102

This last loop transformation provides an important insight that will be used repeatedly. That is, the intrinsic muscle dynamics can be equivalently built with an active feedback system, and effectively provide feedback control. This is the idea behind the equilibrium control theories of [28], explaining experiments in which active feedback was removed. We will refer to the *effective feedback* system and will mean that of Figure 7-5 — generated by both intrinsic muscle properties $\mathcal{Z}$ and active feedback $\mathcal{R}$.

Just as the mechanical compliance of the muscles may be built from an equivalent active feedback controller, the active feedback can sometimes be realized by a physically equivalent passive device (e.g., Figure 7-5 can be realized with an equivalent physical circuit of the form shown in Figure 7-3 with $f = z + r$ substituted for z, where r is defined from the operator $\mathcal{R}$ as described below). Colgate [11] elaborates on this with regard to stability. We will also use this physical equivalence notion implicitly when we talk about mechanical compliance. The term compliance is typically applied to passive mechanical devices, but as an actively controlled feedback system can often be built with an equivalent passive device we can say that this active system has an *effective compliance*, or compliance for short.

7.3.4 Model of Reflexes

To proceed, assume that the proprioceptive feedback only provides velocity and position information. Further, let us neglect the effect of feedback delay (this will be discussed further in Section 7.6). Then, in general the non-linear feedback is $\mathcal{R}\theta = r(\theta(t), \dot{\theta}(t), t)$, and (7.6) becomes:

$$0 \;=\; I\ddot{\theta}(t) + r(\theta(t), \dot{\theta}(t), t) + z(\theta(t), \dot{\theta}(t), t) - \tau_v(t) - \tau(t) \qquad (7.7)$$

7.3.5 External Torques

Considering the perturbation torque $\tau(t)$ to be the input, and adding the possibility of gravity (7.7) becomes:

$$\tau(t) = I\ddot{\theta}(t) + f(\theta(t), \dot{\theta}(t), t) - \tau_v(t) - mgc\sin\theta(t) \qquad (7.8)$$

where I, m and c are the forearm inertia, mass and center of mass respectively, $f(\theta(t), \dot{\theta}(t), \tau_v(t), t) = r(\theta(t), \dot{\theta}(t), t) + z(\theta(t), \dot{\theta}(t), t)$, and $g = 9.8 m/s^2$. Notice that $f - \tau_v$ is the net muscle torque acting on the arm inertia (including parallel connective tissue forces, active feedback, and intrinsic mechanical properties). The gravity term was derived by assuming that the arm is moving in the vertical plane, and θ is defined to be zero at vertical as described in Section 9.1.

7.3.6 Perturbation Model Used in Experiments

We are now ready to address the question of how to experimentally study the closed loop dynamics $\mathcal{P}_{cl}$ represented in (7.8). As the internal forces (e.g., $\tau_v(t)$) that act in addition to the known external forces cannot be controlled or measured, only the local behavior of $\mathcal{P}_{cl}$ about a nominal trajectory $\theta_0(t)$ may be studied. Applying an external perturbation $\tau(t)$ during execution of the nominal trajectory gives a new trajectory that is related to the nominal trajectory through the dynamic behavior of the arm. The arm dynamics can be studied by estimating the relationship between the applied perturbations and the deviations from the nominal trajectory. Specifically, if the applied perturbations are small enough, the closed-loop dynamics may be approximated by the differential behavior about the operating point $(\theta_0(t), \tau_0(t), \tau_v(t))$, which is:

$$\Delta\tau(t) = I(t)\Delta\ddot{\theta}(t) + B(t)\Delta\dot{\theta}(t) + K(t)\Delta\theta(t) \qquad (7.9)$$

$$\Delta\theta(t) = \theta(t) - \theta_0(t)$$

$$\Delta\tau(t) = \tau(t) - \tau_0(t)$$

where the joint inertia $I(t) = I + \partial f / \partial \ddot{\theta}$, the joint viscosity $B(t) = \partial f / \partial \dot{\theta}$ and the joint stiffness $K(t) = \partial f / \partial \theta - mgc \cos \theta_0(t)$. The second term of $I(t)$ should be zero as it could only result from high bandwidth force feedback. Also, the negative gravity contribution to the stiffness turns out to be relatively small (see Figure 10-16 in the results, Chapter 9). θ_0 and τ_0 are the angles and torques measured during an average unperturbed movement. τ_0 may be non-zero.

In the sense that the parameters I, B, and K relate force input to velocity output, they may be referred to as *mechanical impedance* parameters. The relation between force input and position output may be referred to as *complex stiffness*, with *compliance* being the inverse of this relation.

7.4 Control Hypotheses and Predictions

In subsequent chapters experiments to estimate the perturbation model (7.9) are described. In these experiments subjects perform the simple task of moving their arm between two targets, and perturbations are applied to estimate the dynamics. For the present, assume that the locally linear behavior of $\mathcal{P}_{cl}$ may be estimated from these perturbations, and that it may be adequately modeled by the time-varying second order system (7.9). Now, consider what this experimentally determined perturbation model may reveal about the modules $\mathcal{A}$, $\mathcal{R}$ and $\mathcal{P}$ in Figure 7-1.

7.4.1 Feedforward Versus Feedback Control

First, focus on the role of $\mathcal{A}$, the feedforward control. One extreme hypothesis holds that $\mathcal{A}$ compensates for the plant dynamics entirely (i.e., $\mathcal{A} = \mathcal{P}^{-1}$, so $\theta = \theta_0$). This feedforward compensation is non-trivial (i.e., not a linear system) for multi-link arms [21] or even for a single joint operating against gravity. In spite of the difficulty of learning and computing $\mathcal{P}^{-1}$, this hypothesis of feedforward compensation is consistent with experimental evidence. Specifically, trajectories are found to be invariant across load, gravity and speed conditions (call this *trajectory invariance*). That is, for a given movement the trajectories are the same in spite of differing inertial

loads or gravity [107][108], and even take on the same form for different speeds once normalized by movement time [107].

A competing explanation for trajectory invariance is that the closed-loop system $\mathcal{P}_{cl}$ is made to operate as an effective high gain feedback controller ($|\mathcal{P}\mathcal{R}| \gg 1$, so $\theta = \theta_0$). Non-linear link interactions [21] or gravity are treated as disturbances to be servoed out by the high gain feedback. As shown in Figure 7-5, this may be implemented either by active feedback, $\mathcal{R}$, or by altering the intrinsic muscle properties, $\mathcal{Z}$. Both of these possibilities are unlikely. With regard to reflexes, Bizzi et al. [103] provide evidence showing that reflex gains are low. This is not surprising, as delays of more than 25 ms would make high gain feedback unstable. With regard to muscle stiffness, for normal speed movements the co-contraction necessary to produce high intrinsic stiffness is rarely observed [109][110] — tri-phasic, or bi-phasic alternating muscle bursts are usually observed. Thus, neither of these implementations are acceptable, and an account of trajectory invariance requires some form of feedforward control.

7.4.2 Compliance Control Hypothesis

A more likely scenario is that feedforward control is used, but it is not always accurate enough, so low gain feedback is used to assist when necessary. In this way trajectory invariance may be accounted for, and feedback $\mathcal{R}$ and intrinsic muscle properties $\mathcal{Z}$ may still have a role. More generally that role would be to *control the mechanical compliance* of the arm. Specific examples of compliance control have been suggested previously. For example, the reflex action of feedback may make the system dynamics look more like a linear compliance, thus simplifying the job of the feedforward controller [111]. Another suggestion is that low levels of muscle stiffness may provide stability against unexpected disturbances [28]. Finally, as mentioned in Chapter 1, the control goal of having a high mechanical compliance is advantageous for constrained motion, particularly when the constraint is unpredictable or unexpected (e.g., to avoid jamming, excessive contact force, damage or injury).

Thus, for the movements studied in this thesis a reasonable control hypothesis to

test is that the arm's mechanical compliance is maximized, while still maintaining the specified task accuracy. That is, the arm's effective stiffness (i.e., restoring forces to trajectory errors — with the motor system viewed as the feedback controller in Figure 7-5) should be low, but high enough to assure that trajectory errors larger than the specified task accuracy are removed. As imperfect feedforward control or external perturbations will inevitably cause trajectories errors, the effective stiffness must be positive at all times. In summary, the first prediction for the perturbation experiments is:

(P1) *In so far as the arm's stiffness can be adjusted for a particular task, the stiffness should be as low as the task accuracy allows. In the task of pointing between targets accuracy during movement is not demanded. Thus, the stiffness should be low during movement (to provide compliance), and higher at the targets (to ensure accuracy).*

The mechanism for controlling arm compliance may rely on both intrinsic muscle properties and reflex activity. For example, the intrinsic velocity dependent dynamics of muscle could make lowering of the stiffness during movement automatic (this is discussed further in Sections 7.5 and 11.3). In addition, reflexes are known to adjust dramatically during particular tasks. For example, in walking there is a strong anterior tibial H-reflex during stance, but little reflex response in the swing phase [112].

7.4.3 Limited (Static) Feedforward Control Hypothesis

The computational complexity of feedforward control naturally leads to the question of how much feedforward control is really necessary. Consider the hypothesis that only the instantaneous static component of the dynamics $\mathcal{P}_{cl}$ is inverted by the feedforward $\mathcal{A}'$ in Figure 7-2. That is, the feedforward torque τ_v is computed by (7.8) with $\dot{\theta} = \ddot{\theta} = \tau = 0$:

$$\tau_v(t) = f(\theta_d(t), 0, t) - mgc \sin \theta_d(t) \qquad (7.10)$$

107

Under this hypothesis, the desired trajectory $\theta_d(t)$ can be viewed as an *equilibrium trajectory* [28], in the sense that it is only achieved when the arm comes to rest. During movement of the arm there is always a trajectory error, due to the non-static components of $\mathcal{P}_{cl}$. Note that this is feedforward control in the sense that it requires knowledge of the static properties of muscles. The behavior of the actual trajectory $\theta(t)$ driven by the static feedforward command (7.10) is governed by:

$$
\begin{aligned}
0 \;=\;& I\ddot{\theta}(t) + f(\theta(t),\dot{\theta}(t),t) - f(\theta_d(t),0,t) \\
& -mgc(\sin\theta(t) - \sin\theta_d(t)) \tag{7.11}
\end{aligned}
$$

Now consider the consequences of this static feedforward hypothesis for attempting to generating two identical but different speed movements. That is, suppose (7.11) describes a particular movement $\theta(t)$ specified by the equilibrium trajectory $\theta_d(t)$, and suppose a faster speed movement $\theta_f(t)$ is attempted under this hypothesis — that is by simply time scaling the equilibrium profile by a factor of r. Thus, the new desired trajectory is $\theta_d(rt)$. Substituting this into (7.11), and replacing t by t/r gives the equation governing the behavior of the faster movement $\theta_f(t)$:

$$
\begin{aligned}
0 \;=\;& r^2 I\ddot{\theta}_f(t/r) + f(\theta_f(t/r),r\dot{\theta}_f(t/r),t/r) - f(\theta_d(t),0,t/r) \\
& -mgc(\sin\theta_f(t/r) - \sin\theta_d(t)) \tag{7.12}
\end{aligned}
$$

where the time scaled faster movement $\theta_f(t/r)$ should be close to $\theta(t)$.

To see how different $\theta_f(t/r)$ and $\theta(t)$ actually are make the following simplifications: (1) assume the dynamics f are time invariant (or at least they change at a rate r faster for the faster movement), and (2) assume that the dynamics are the same for both movement speeds (later we will see how scaling the dynamics may change things). Now subtract (7.11) from (7.12) to give:

108

$$0 = I(r^2\ddot{\theta}_f(t/r) - \ddot{\theta}(t)) + f(\theta_f(t/r), r\dot{\theta}_f(t/r)) - f(\theta(t), \dot{\theta}(t))$$
$$-mgc(\sin\theta_f(t/r) - \sin\theta(t)) \tag{7.13}$$

When the movements just start (without loss of generality, let that be at $\theta = 0$) only the acceleration terms are significant. Thus, (7.13) implies $r^2\ddot{\theta}_f(t/r) = \ddot{\theta}(t)$. That is, there is a factor of r^2 less acceleration in the *time scaled* faster movement at the beginning the movement. Equivalently, the scaled faster movement looks like it has r^2 times more inertia in its dynamics. Once significant velocity is reached predictions are harder to make without simulations, but the trajectories do diverge increasingly.

Alternatively, the dynamics might be adjusted to compensate for an increase in movement speed. Consider the case where the dynamics are linear and of second order. In this case, increasing the stiffness by a factor of r^2 and the damping by a factor of r is the appropriate adjustment to have the faster movement $\theta_f(t)$ have a time scaled trajectory $\theta_f(t/r)$ equal to the slower trajectory $\theta(t)$ [107][113] (assuming no gravity is present). To prove this, let $f(\theta_f(r), \dot{\theta}_f(t), t) = B\dot{\theta}_f(t) + K\theta_f(t)$, and $g = 0$ in (7.12), and divide through by r^2 to give:

$$0 = I\ddot{\theta}_f(t/r) + r^{-1}B\dot{\theta}_f(t/r) + r^{-2}K(\theta_f(t/r) - \theta_d(t)) \tag{7.14}$$

Letting $B = rB$ and $K = r^2K$ eliminates r, and thus makes the time scaled solution $\theta_f(t/r)$ identical for all speed movements.

In summary, with regard to different speed movements the static feedforward hypothesis implies the following prediction for the perturbation experiments:
(P2) *Either the time scaled trajectories must differ for different speed movements, or the dynamics must be scaled. If the dynamics are approximated by a second order linear system, this dynamic scaling requires that the stiffness increases by a factor of r^2 and damping increases by a factor of r, where r is the movement speed increase.*

Next consider the influence of gravity on a control system operated under the static feedforward hypothesis. The prediction for the experiments is simply:

(P3) *The absence or presence of gravity should not affect the stiffness, damping or trajectory. It should be compensated for by the hypothesized static feedforward system.*
Of course, if the actual trajectory differs significantly from the desired trajectory the gravity compensation might be inappropriate. See (7.11). This deviation of the actual trajectory from the desired trajectory should be small for slow speed movements, but increase with increased speed of movement — as discussed above.

It is possible that gravity compensation is achieved by feedback instead of feedforward control. For example, there could be an integrator in the feedback controller $\mathcal{R}$, eliminating the steady-state positioning error (e.g., PID control). In this case, the linearized dynamics would have to be at least third order. As second order dynamics adequately account for the variance in previous posture perturbation experiments (see review in Chapter 8) this is not expected to be a possibility.

Finally, with respect to non-static changes in the dynamics the static feedforward hypothesis does not predict compensation. For example,

(P4) *When the dynamics are changed by an external viscous damping load, the static feedforward compensation should not adjust for this change, and the trajectories should thus differ from the unloaded trajectories.*
Earlier studies of whole arm movements indicate that damping loads do change the trajectories. Using the instrumentation techniques and methods of [108][107] we studied whole arm sagittal plane movements with a damping load applied to the elbow joint. Figure 7-6 shows typical normal speed trajectories made with and without the damping load of 1.5 $Nm/rad/s$. The figures show three typical movements between targets after 20 practice trials. Movements recorded immediately after changing the damping are very similar, showing little adaption. Particularly striking is the increased difference between the upward (dotted lines) and downward movements (solid lines). See also [114].

The finding that a damping load does affect the arm's trajectories is to be contrasted with the finding that whole arm trajectories are unaffected by a mass load
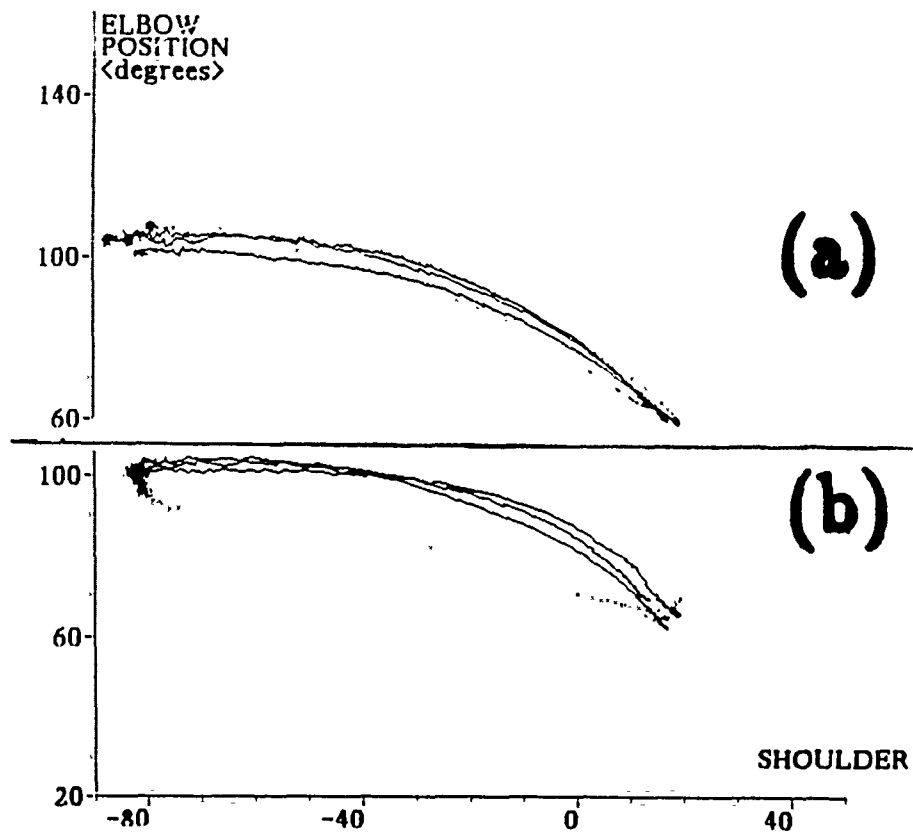
Figure 7-6: Whole arm joint-space trajectories made (a) without and (b) with a damping load of 1.5 $Nm/rad/s$ acting about the elbow joint. Subjects were given time to adapt to the load changes (though little adaption occurred), and in the unloaded case the subjects still carried the mass of the damper. Three upward (solid) and three downwards movements (dotted) are shown. Each movement took approximately 500 ms.

carried in the hand [107]. If the results in [107] are correct, there must at least be non-static compensation for inertial loads.

Approximate estimate of desired trajectory

Under the rough approximation that the muscle dynamics are linear it is possible to back calculate the desired equilibrium trajectory, given a static feedforward hypothesis:

$$\theta_{desired} = \theta + 1/K(t)[I(t)\ddot{\theta} + B(t)\dot{\theta} - mgc\sin\theta] \qquad (7.15)$$

The difference $(\theta - \theta_{desired})$ provides an indication of the positioning accuracy of the feedforward compensation. Although the dynamics may be non-linear (though see

111

[111] for the possible linearizing effect of reflexes), this calculation is approximately correct if the $\ddot{\theta}$, $\dot{\theta}$ and $(\theta - \theta_{desired})$ are respectively of similar amplitude and frequency content to the $\Delta\ddot{\theta}$, $\Delta\dot{\theta}$ and $\Delta\theta$ perturbations used to estimate I, B, and K.

7.4.4 Dynamic Scaling Feedforward Control Hypothesis

Another possible method to simplify feedforward control is to learn accurate feedforward commands for only one slow speed movement and scale up the torques and dynamics to achieve the same movement at higher speeds [107][113]. Assuming muscle is adequately approximated by a linear system it is possible to predict under this dynamic scaling hypothesis that:

(P5) *The stiffness should scale up by a factor of r^2, and the viscosity should scale up by a factor of r, where r is the speed increase factor.*

The weakness with this argument is, again, that the dynamics may not be linear.

For single joint movements executed under this dynamic scaling hypothesis the required stiffness and viscosity scaling keeps the damping ratio fixed. In recent posture experiments we have found that the damping ratio is constant across three levels of voluntary muscle co-contraction [115][116]. Scaling of the dynamics during movements has not yet been tested.

7.5   Role of Muscle Dynamics

The measured perturbation dynamics are a function of active feedback, inertia, connective tissue, and muscle. To assess the possible contribution of muscle the following review is provided.

7.5.1   Frequency Range of Interest

First, consider what aspects of muscle dynamics are *not* relevant. For the unconstrained movements studied in this thesis, it is possible to show that above 5 Hz the elbow joint dynamics are dominated by the arm inertia (see Figure 10-8). Thus, only

muscle/tendon dynamics between 0 and 5 Hz are relevant to understanding these arm movements.

7.5.2 Molecular Level Description

On a molecular scale the mechanism of muscle force production is described well by a model of crossbridge bonding between sliding filaments [117]. A cycle of crossbridge connection and disconnection happens continuously. The instantaneous number of connected crossbridges is related to the stimulation frequency, and it is roughly proportional to the net muscle force.

When a tetanized muscle fiber is subjected to an externally imposed step change in length there results a large transient increase in force (typically, lasting only a few milliseconds), and then a gradual change in force to a steady-state value [118]. The latter force dynamics are most relevant to the present arm movement study, (i.e., they are in the 0–5 Hz frequency range, above which inertia dominates). To a first approximation, the transient force can be attributed to the stiffness of the crossbridges before they break, and the dynamics of the slower force production process can be attributed to the crossbridges cycling and reforming. A more detailed analysis requires consideration of the distributed nature of the sarcomeres within the fiber. The sarcomere lengths are known to be non-uniform and change even when the muscle is in isometric contraction (see review in [119]).

7.5.3 Steady-State Length-Tension Curves

The steady state force value is a function of only the final length, giving the so called length-tension relation. Figure 7-7 shows a length-tension plot made by Gordon et al. [120] from an experiment where they measured the steady state force reached in response to an isotonic change to a specified fixed length (some points extrapolated). The force change to steady state takes 50-100 ms (as in [118]), which implies that the slope of the length-tension curve can only be interpreted as a 'stiffness' when dealing with phenomena slower than 50-100 ms.
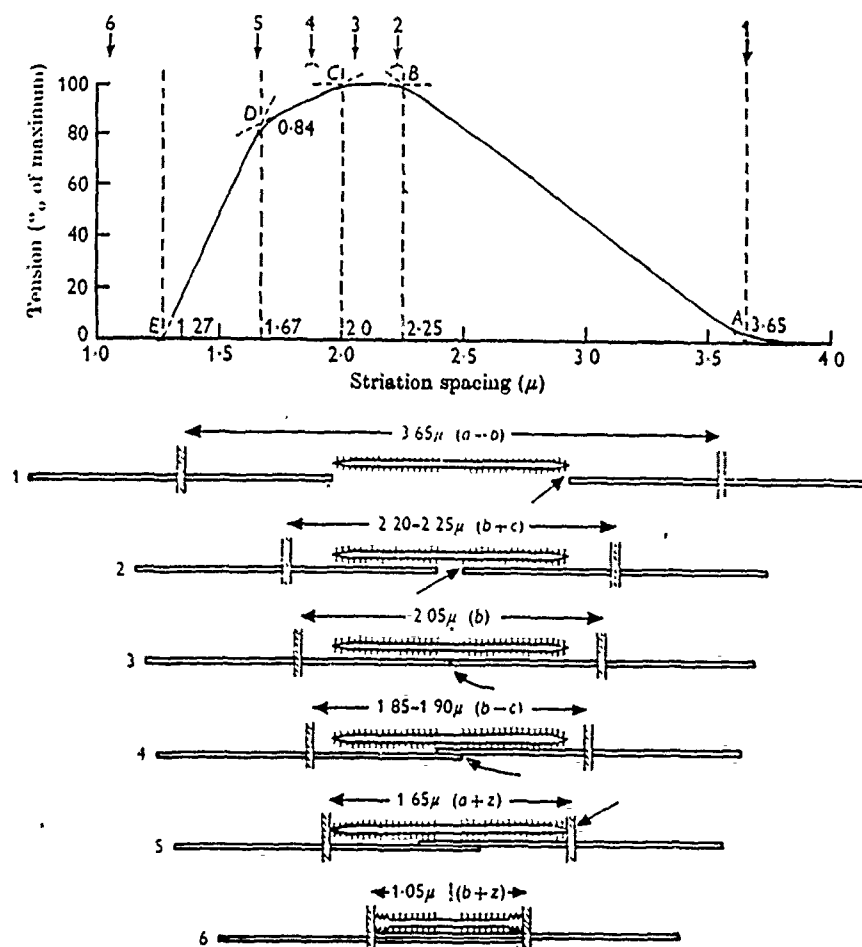
Figure 7-7: Static length-tension curve for changes of sarcomere length in a muscle fiber. Numbers correspond to interpretation in terms of the sliding filament theory. Reprinted from [120].

7.5.4 Isotonic Shortening

During muscle movement the length-tension relation has no meaning. In fact, during the isotonic shortening of the muscle fiber in [120] the velocity is relatively constant, indicating that the stretching fiber presents a viscous-like load, with zero stiffness.

7.5.5 Whole Muscle

On the macroscopic scale similar length-tension relations are found [121][122][123] (see Figure 7-8 from [122]), although the mechanisms are more complex. Mammalian

114
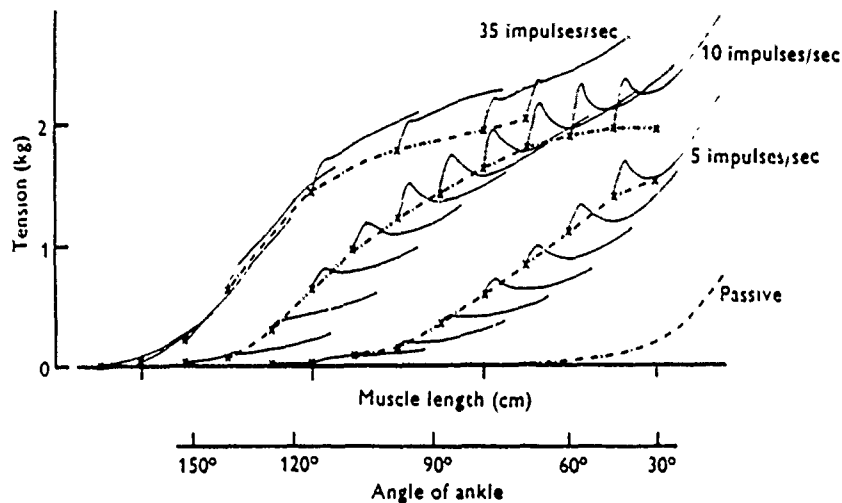
Fig. 3. Tension during extension through different parts of the length range. Tension records from a number of different extensions similar to those shown in Fig. 2 have been traced (continuous line) to show how the tension during lengthening differs from the isometric tension in various parts of the length range. Positions of the ankle joint are shown below corresponding parts of the abscissa.

In each case the muscle was lengthened through 6 mm at 7·2 mm/sec. The interrupted lines are isometric length-tension plots.

Figure 7-8: Static length-tension curves for responses to changes in whole muscle length, with different rates of asynchronous stimulation. Reprinted from [122]

muscle fibers are arranged in parallel, and attached to ligamentous tissue in a complex pennate structure. Changes in pennation angle can allow muscle length changes without significant muscle fiber length changes [124]. Also, muscle fiber recruitment can alter the dynamics. Muscle is innervated by many intermixed motor-neurons, which are commonly thought to be recruited by size [125], but can also be recruited in complex synergistic patterns [126]. Net muscle force production is regulated by recruitment and stimulation rate. At low forces recruitment is found to be the dominant control mechanism, and thus affects the muscle stiffness most dramatically [127]. Presumably, the force and dynamic stiffness should increase with an increase in the number of parallel muscle fibers recruited.

115

7.6 Role of Reflexes

The experiments described in this thesis do not provide a clear distinction between reflex induced stiffness and intrinsic muscle stiffness. An ideal way to investigate the role of feedback would be to reversibly block all relevant afferent information (e.g., with a fusimotor block [128] [129]) during selected movements and observe the difference in the estimated perturbation parameters. As this is a difficult experiment (even in animals) we can only distinguish the feedback and intrinsic muscle properties from the closed-loop dynamics, $\mathcal{P}_{cl}$. This distinction is perhaps possible because of delay.

If delayed feedback $\mathcal{R}$ is significant, then the closed-loop dynamics $\mathcal{P}_{cl}$ should be a function of not only the current state (velocity and position), but also delayed velocity and position. Thus, to a first approximation the linearized dynamics should be a second-order model with delay terms:

$$\Delta\tau(t) = I(t)\Delta\ddot{\theta}(t) + B(t)\Delta\dot{\theta}(t) + K(t)\Delta\theta(t) \qquad (7.16)$$
$$+B_d(t)\Delta\dot{\theta}(t+T) + K_d(t)\Delta\theta(t+T)$$

where, for example, $T = 25ms$. The parameters of (7.17) can be estimated, and the relative contribution of the delayed terms can then be tested. This will be left for future work.

Chapter 8

Literature Review

Many perturbation studies have been performed to infer intact arm dynamics. This chapter will review these studies to compare instrumentation, modeling techniques, and perturbation parameter estimates. With the exception of [130] the research has been restricted to measuring the mechanical properties during posture.

The review is organized in terms of the instrumentation used for applying the perturbations and the perturbation type. This organization is perhaps the clearest as the particular instrumentation limits the range of perturbations possible (and in some cases changes the arm's dynamics), which in turn affects the estimated perturbation dynamics. If the motor system was linear all perturbation methods should give the same results. Unfortunately, it is non-linear, and impedance estimates are known to depend on the perturbation amplitude, type, and frequency content.

8.1 Passive Mechanical Perturbations

8.1.1 Sinusoidal Position Perturbations

A simple method of perturbing the arm is to attach it to a shaft mounted eccentrically on a rotating fly wheel (a rotating cam setup). In [12] (see also Zahalak [131]) such an apparatus was used to apply sinusoidal position perturbations of up to 22 Hz. Perturbation amplitudes of 0.46 mm, 0.96 mm, and 4.6 mm were tested while

117

the subject maintained large mean forces (35-130 N). The frequency dependent damping was inferred from the out-of-phase force responses. Damping increased roughly proportionally to frequency, as is expected of a second order system, with the exception of the behavior between 8-12 Hz. In the 8-12 Hz frequency range the damping surprisingly dropped below zero for the smallest amplitude perturbations, predicting a form of limit cycle instability.

The main problem with this approach is that the low frequency sinusoidal stimuli may be tracked voluntarily. At frequencies below 6 Hz the authors found that the results were very variable and could not be used. As the in-phase system response was dominated by the arm inertia at or above 6 Hz (i.e., the in-phase force increased proportionally to the square of the frequency) stiffness estimates were difficult to make.

8.1.2 Viscoelastic Perturbations

Another method to assess the mechanical response of the arm is to attach it to a pair of springs [13][132]. The arm is set into oscillation by off-setting the spring from the equilibrium. In [13] this method was used to drive the arm into a sustained 8-12 Hz, 3 mm tremor (their predicted range of instability [12]). In [132] this method was used to show that the arm's natural frequency (considered as a second order system) increases with the subject's voluntary resistance to the perturbations. They also used a pseudorandom binary input (see below) to obtain a more detailed description of how the dynamics change with voluntary command change.

8.1.3 Inertial Perturbations

Bizzi et al. [133] used inertial loads to assess the difference in monkey head positioning with and without proprioceptive feedback. They found that even without proprioceptive feedback a monkey could still move its inertially loaded head to a desired position. As a follow up to this experiment Bizzi et al. [134][135][136] performed a similar experiment on monkey arms. Here they perturbed the deafferented arm

with a position pulse during movement [136], and found that the arm qualitatively returned to the original path after the pulse was over. Thus, they speculated that a virtual trajectory was specified as the input command, and the intrinsic muscle stiffness maintained the arm on that trajectory. No stiffness estimates were made during the movements.

8.2 Electromagnetic Actuators

8.2.1 Sinusoidal Positions Perturbations

Agarwal and Gottlieb [137] studied the position responses of the ankle joint to sinusoidal torque inputs applied by a DC torque motor. They also found that sinusoidal inputs were problematic. Such inputs produced a different compliance than measured with random inputs (see below). They suggest that the motor system's dynamics changes to adapt to each separate frequency input.

8.2.2 Sinusoidal Force Perturbations During Movement

Lanman [130] studied the response to sinusoidal force perturbation applied during movement. Only high frequency force inputs between 15 and 30 Hz were analyzed. He used a similar analysis technique to [12], which relies on a preliminary estimate of the arm inertia to estimate the total joint torque. This total joint torque was then compared with joint acceleration. He assumed a frequency dependent second order model, defining the in-phase component of the joint torque as the stiffness, and the out-of-phase component as the damping. The main finding was that the joint stiffness is proportional to (1) the load force and (2) the inverse of the velocity. For unloaded movements the stiffness drops during the movement. For movements loaded with a viscous damper the force dependency of stiffness cancels out the velocity dependency, and can even increase the stiffness over the resting stiffness. Lanman attributed the measured stiffness to short range stiffness of crossbridges (see discussion in Section 11.3).

8.2.3 Step Force Perturbations

Crossman and Goodeve [8] studied wrist rotation responses to small amplitude step changes in torque. Although they do not give details of the size of the perturbation or the nature of force actuation, they claim that a critically damped second order system models the responses well.

8.2.4 Step Position Perturbations

Mussa-Ivaldi et al. [138] used a two link direct drive manipulandum to apply perturbations to the whole arm supported in the horizontal plane at posture. They used a 'do not intervene' instruction to the subject, and defined the stiffness as the ratio of force to position change after about 200 ms. They found that the two dimensional stiffness fields always had a characteristic maximum value oriented radially through the shoulder.

Sinkjaer et al. [139] studied human ankle torque responses to step changes in angle. A servo controlled geared DC motor was used to provide 2^0 step angle changes with a 40 ms rise time (other amplitudes between 1^0 to 7^0 were also used). The 'steady state' (after 450 ms) torque changes were used as a measure of stiffness, with the subjects being asked to 'not intervene' during the perturbations. In spite of the possibility of voluntary intervention, they found that the stiffnesses measured at low background torques were comparable with the stiffnesses measured for the ankle joint with pseudorandom inputs [140][141]. However, at higher background torques they found almost constant stiffness, contrary to [141].

An interesting innovation in [139] is that they were able to measure active muscle stiffness without reflexes. The authors found that by stimulating the deep peroneal nerve transcutaneously they could activate the anterior tibial muscle to both maintain a fixed mean torque and abolish reflex or voluntary input. These intrinsic muscle stiffnesses were found to be only slightly lower than the stiffnesses measured with the reflex intact.

8.2.5 Gaussian Random Torque Perturbations

Agarwal and Gottlieb [140] studied the position responses of the ankle joint to random Gaussian noise torque input. Band limited (2 to 30 Hz useful power) Gaussian white noise was applied with a DC torque motor (the authors neglected to mention the amplitude (i.e., standard deviation) of the input). They found that, in contrast to their earlier sinusoidal perturbation studies, the response could be adequately modeled by a linear second order system (with coherence of about 90%).

The ankle joint stiffness was found to increase with mean voluntary torque production (ranging from 17 Nm/rad at zero torque to $45Nm$ at 2 Nm torque) and was angle dependent over a 24⁰ range (ranging from ₁5 Nm to 30 Nm for the zero voluntary torque level). Using the estimated inertia value of approximately 0.02 kgm^2 (which includes the inertia of the apparatus) these stiffness estimates give natural frequencies between 4 and 7 Hz.

Yosef and Inbar [142] also used Gaussian noise torque inputs to measure joint impedance. They used a torque motor to apply input forces to the elbow joint, but complicated matters by not measuring the motor torque. Thus they had to estimate the torque from the motor dynamics. They found that the estimated joint inertia can change and attributed these changes to Golgi organ tendon force feedback. Another explanation is that their estimated torques were not accurate.

8.2.6 Pseudorandom Binary Torque Perturbations

Soechting et al. [143] (see also [144][132][145] for related work by these authors) used pseudorandom binary sequence (PRBS) torque inputs to characterize the EMG response of the elbow joint during movement. They used an amplitude of 8 Nm, and 20 ms elements in the PRBS. A novel time-varying impulse response identification technique was used to characterize the force to EMG response. Although they recorded angular position information, they unfortunately did not report any force-position transfer functions.

8.3 Hydraulic Actuators

Hunter and Kearney [146][147] used angular pseudorandom binary sequence (PRBS) inputs to characterize the human ankle joint torque response. They drove a position servoed electro-hydraulic actuator with a 200 Hz PRBS command to produce an input power spectrum flat from 0 to 25 Hz. They found that a second order model adequately accounted for the response, but that the model parameters depended upon the perturbation amplitude.

Weiss, Hunter and Kearney [148][149][141] extended the results of [140]. They found that there is a position dependence of the joint stiffness over the entire range of motion, and that there is a linear relation between mean voluntary torque and stiffness for each position.

Damping ratio's of 0.3 to 0.4 were measured (the same as for the random inputs in [140]), which should be contrasted with the damping ratio's of 0.8 to 1.0 measured in pulse perturbation experiments (e.g., [8]). See Section 11.1 for further remarks concerning this discrepancy.

They also found that at high voluntary torque levels the estimated inertia increased. This anomaly is likely due to the muscle stiffness increasing so high that the actuator could not produce sufficient power at frequencies where the inertia dominated. Thus, for high force levels frequencies of up to 100 Hz are required for proper system identification.

8.4 Pneumatic Actuators

8.4.1 Pseudorandom Binary Torque Perturbations

We have reported preliminary results with a wrist-mounted pneumatic thruster (airjet) [116][150][151]. This one dimensional 400 g airjet applies ± 4 N binary forces to the wrist, at frequencies up to 75 Hz. The airjet switches the flow direction by a fluidic property called the Coanda effect. The current limitations of this airjet are that it can only produce binary force sequences, and that the magnitude of the

force cannot exceed 4 N. The advantages are that it is unencumbering, it changes the arm dynamics minimally, and it has a high bandwidth. We intend to develop a 3-dimensional version similar to Colgate's airjet described below [152].

8.4.2 Graded 3-Dimensional Torque Perturbations

Earlier wrist mounted airjets were designed by Colgate [152] and Murray [153]. Both of these designs incorporated the additional constraint that the airjet had to produce graded forces. The airjet in [153] produces 8 N pulses with a 40 ms rise time. It is of low bandwidth, but has three states: +8 N, -8 N, and 0 N. The airjet device in [152] produces controllable 3-dimensional forces at up to 8 Hz. The airjet's open-loop performance (i.e., just producing binary forces) could exceed 25 Hz. Both of these designs were based on a spool-valve switching mechanism.

Chapter 9

Time-Varying Identification Method

The objective of the experiments is to find the time-varying parameters $I(t)$, $B(t)$ and $K(t)$ in (7.9) while the subject is executing a fixed movement pattern, specified by $\theta_0(t)$. It should be emphasized that these impedance parameters are only valid for the operating conditions under which they are measured. In no way is the system assumed to be linear. This perturbation model describes the locally linear behavior of the closed-loop dynamics $\mathcal{P}_{cl}$.

9.1 The Task

In order to estimate time-varying dynamics many repeated movements are required to provide an ensemble average. Thus, it is critical to choose a task that may be made repeatably. After preliminary tests, it was found that a task that subjects could repeat accurately was to make rhythmic movements between two target points, in time to a regular auditory stimulus. This was the task performed in all experiments described.

The two targets used were 1.0 *rad* (approximately 57 degrees) apart, well away from the joint limits (Figures 9-1 and 9-2). The upper arm was immobilized in the sagittal plane perpendicular to the torso. Target 1 was at the position with the

124
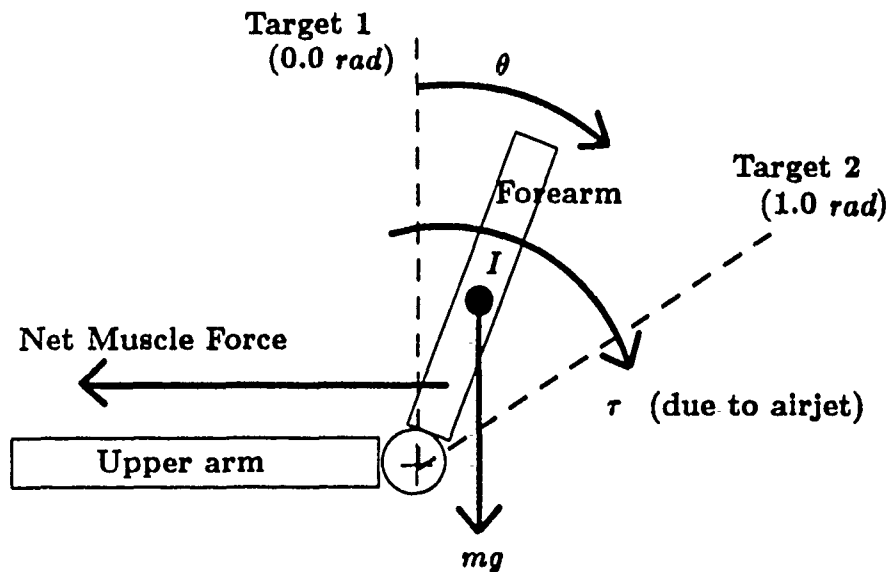
Figure 9-1: Target and variable assignments for movement task.

forearm perpendicular to the upper arm, and target 2 was at 1.0 rad extension from target 1. The joint angle θ is defined to be zero at target 1 and to increase with the elbow extension; thus, target 2 is at $\theta = 1.0 rad$. A single *movement* is defined to be one cycle from target 1 to target 2 and back.

The auditory stimulus was provided by clicks from a piezoelectric buzzer, at intervals of either 750 *ms* or 1000 *ms*. Subjects were instructed to move continuously and repeatedly between targets, and be at a target at the time of a click. Continuous movement, not accuracy, was stressed. Subjects were instructed to relax and move naturally, in spite of the perturbations.

In some trials the subjects were seated with their forearm moving in a vertical plane with respect to gravity. In others, subjects moved in the horizontal plane, with no gravity.

In addition to the two speed conditions (750 *ms* and 1000 *ms* movements) and the two gravity conditions, in some trials the subjects were loaded with a damper (approximately 1 $Nm/rad/s$) that acted about the elbow joint. The force-velocity specifications for the damper are shown in the Appendix.

For each condition 15 blocks of 30 *s* each were collected (this gives 300 movements

125
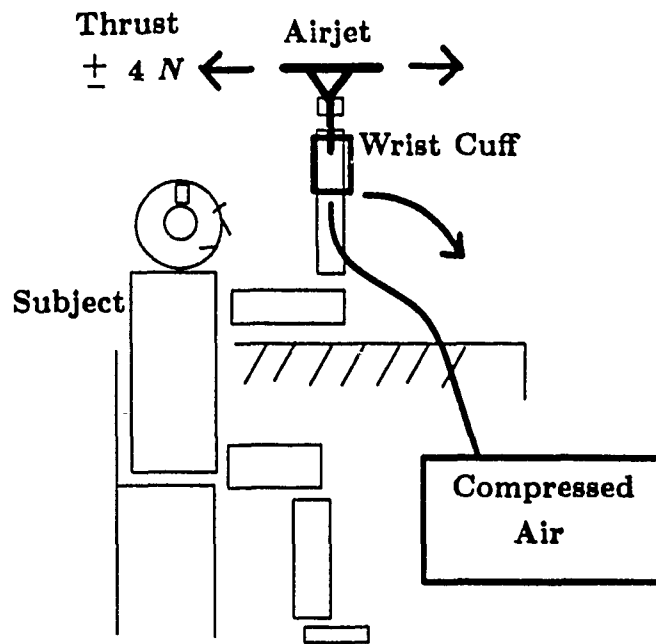
Figure 9-2: Experimental setup.

of 750 ms or 225 movements of 1000 ms per condition). Three minutes rest between blocks was provided to avoid fatigue.

To control for joint angle dependent stiffness (e.g., due to muscle moment arm changes) subjects also maintained one of three poses while being perturbed (for 5 s each). These poses were at target 1, target 2 and a target midway between 1 and 2 (i.e., at 0.5 rad). As in the movement experiments, subjects were asked to relax, but still achieve the task (i.e., maintain the target position).

9.2 Stimulus Type: PRBS

A pseudorandom binary force sequence, PRBS (see Figure 9-3), was chosen as the input stimulus because it could not be predicted by the subject, and it is optimal for system identification (in the sense that it can provide band limited white noise with a minimum length segment). See Chapter 8 for a review of the various alternative input stimuli.

The PRBS was applied continuously by an airjet [150][151] during all movements

126
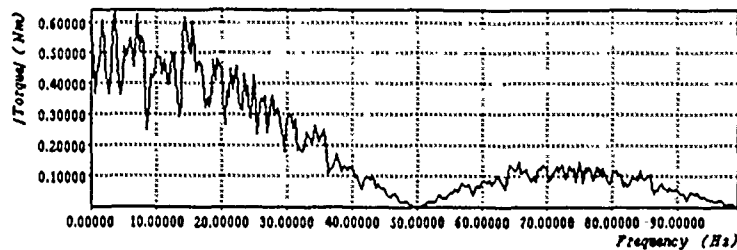
Figure 9-3: Frequency response of a PRBS with a switching interval of 20 ms.

tasks. The airjet applied forces of ±4 N to the wrist in the direction of elbow flexion/extension.

In preliminary experiments the PRBS was composed of 10 ms elements (10 ms is the minimum stable switching interval for the airjet), giving a relatively white noise inprt signal up to 50 Hz. Subsequent analysis revealed that for this movement task the natural frequency of the arm was below 3 Hz (see results in next chapter). Thus, to put more low frequency power into the system at its natural frequency the airjet was switched at 20 ms intervals in a PRBS. This results in a relatively white noise input between 0 and 25 Hz. See Figure 9-3 for the frequency response of this PRBS. Frequency spectral shaping is possible by stochastic shuffling [154] or by analytic techniques [155], but was not deemed necessary without more a priori information on the elbow joint dynamics.

9.3 Airjet Perturbation Device

9.3.1 Specifications

The primary design goal wa. ;hat the PRBS perturbation device must not constrain the arm movement, or significantly change the arm dynamics. For this reason, a light weight wrist-mounted pneumatic thruster device was used [150]. A further design constraint was that the device must have sufficient force and bandwidth to perturb the

arm measurably at frequencies up to 100 Hz. The 100 Hz frequency goal was chosen to be several times higher than the highest natural frequencies measured for joint dynamics (see measurements in [141] for example). This frequency allows accurate estimation of the inertia under all physiological conditions, provided the force is large enough. An approximately 4 N force turns out to be a good compromise for the the force produced by the airjet. As the inertia dominates at high frequencies it is possible to make a rough calculation of what displacement this force will produce at 100 Hz. With an inertia of $I = 0.1 kgm^2$ and a moment arm of 0.4 m, a 0.1 mm displacement results from a 4 N 100 Hz force perturbation. This 0.1 mm displacement is within the resolution of the position sensor described below. Also, given the low frequency content of the PRBS perturbation stimulus it was found that a 4 N force rarely perturbs the arm more than 5 — 10 degrees (see Chapter 10). Thus, the small perturbations assumption in the analysis is probably not violated. Finally, a 4 N force applied at the wrist produces approximately the same torque as the maximum torque produced by the muscles in the task studied; see Section 11.1 for a discussion of this. Thus, the force is sufficiently large to provide relevant measurements to study normal speed movement formation.

9.3.2 Design

The details of the airjet design used in this thesis may be found in [150][151]. A brief summary of the design is included here.

The airjet is a device that is mounted on the subject's wrist. It consists of a nozzle to speed up the air velocity to about 200 m/s, and a switching mechanism to divert the air flow down one of two thin walled brass tubes that bend to point in opposite directions along the line of arm movement. See Figure 9-4. With the flow down one tube a 4 N reaction force is produced — due to the mass flow rate of air (30 cubic feet per minute). The force is switched 180 degrees to the other tube in 5 ms with a rise time of 1 ms. Figure 9-5 shows this switching response. The 5 ms delay is mostly due the solenoids used in the switching mechanism and could be lowered. The extremely rapid 1 ms rise time is realized because the switching is based on a fluidic property
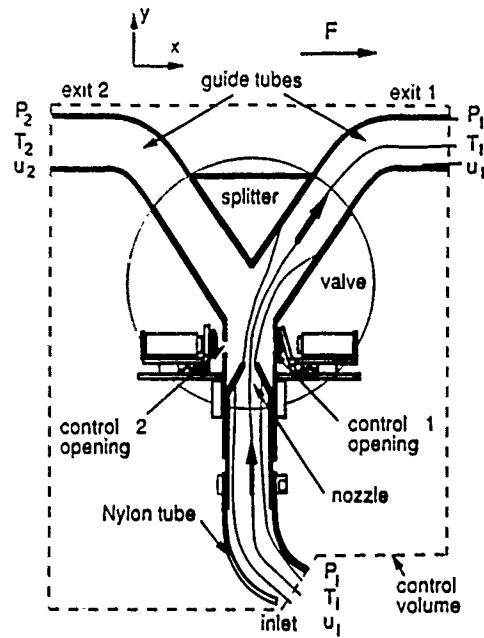
Figure 9-4: The wrist mounted airjet used in experiments. Figure reprinted from [150].
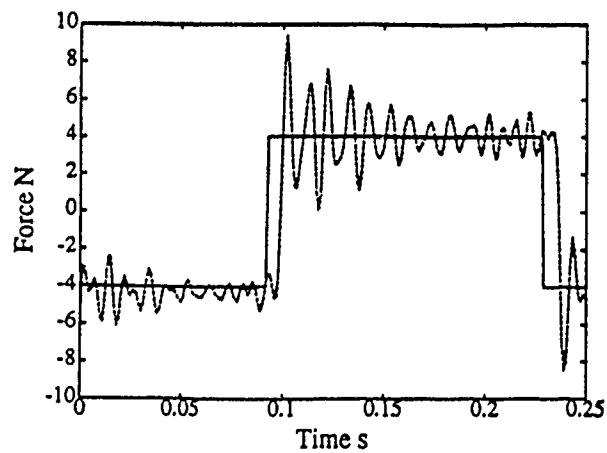
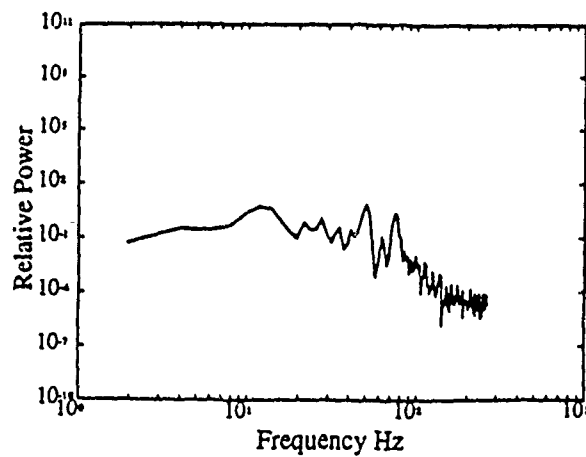Figure 9-5: Step response of airjet. Figure reprinted from [150].

Figure 9-6: Force power spectrum of airjet following a PRBS at the maximum switching rate. Note: this is *not* the force input used in the experiments. See Figure 9-3. Figure reprinted from [150].
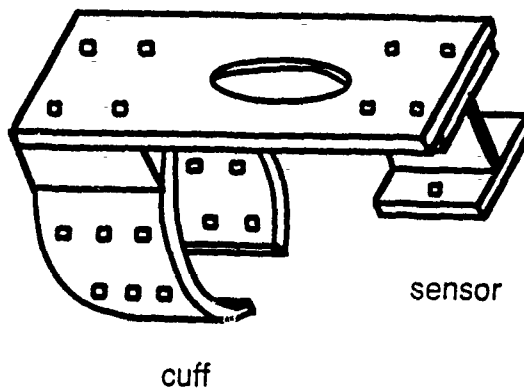

Figure 9-7: Cuff mounting. The wrist is placed in the circular section, and the airjet attaches to the I-beam force sensor. Figure reprinted from [150].

called the Coanda effect. Only the inertia of the air limits the theoretical switching speed. Figure 9-6 shows the device's bandwidth. The mass of the airjet is 400 g. The air flow produces substantial noise, requiring the subject and experimenter to wear ear protection.

9.3.3 Wrist-Cuff Attachment

The airjet is placed above the hand such that it produces force in the direction of elbow flexion/extension and is aligned with the long axis of the arm to avoid pronation/supination torques. It is attached to an aluminum frame which is clamped on the wrist. See Figure 9-7. The subject wears a custom molded cuff for ease of clamping and comfort. Cuff movement was found to be negligible (0.1 – 0.2 mm) for the perturbations used [150].

9.4 Sensing

9.4.1 Force Sensing

An I-beam with strain gauges connects the airjet to the cuff frame [150]. See Figure 9-7. The I-beam is sufficiently compliant to obtain good force sensitivity, but stiff enough to have a resonance (160 Hz) well above the arm's natural frequency. To avoid aliasing the force data were low pass filtered with a linear phase, $-80db$ stopband analog filter with a cut-off frequency of 200 Hz (i.e., an 8 pole, 6 zero *Frequency Devices DOW848* filter with a 4.2 ms pure delay).

9.4.2 Position Sensing

The position of an infrared light-emitting diode (IRED) on the cuff was measured with an Optotrak^{TM} system, a 3D motion measurement system with a 0.05 mm resolution [150]. Data was sampled at the maximum rate of 200 Hz, and interpolated to the 600 Hz force sampling rate with cubic splines.

Let (x, y) be any point in the plane of rotation of the elbow. The center of rotation

(x_c, y_c) and radius r_c to the IRED were estimated by finding the least squares best fit circle that goes through all the movement data. The angle with respect to vertical was then computed as:

$$\theta = tan^{-1} \frac{x - x_c}{y - y_c} \qquad (9.1)$$

The applied torque was computed as:

$$\tau = rF \qquad (9.2)$$

where F is the measured force, and $r = r_c + 0.18m$ ($0.18\ m$ is the distance from the IRED to the force sensor).

9.4.3 Pronation/Supination

To control for possible unmeasured wrist pronation/supination some trials were performed with the airjet and cuff directly connected to a revolute joint with the axis of rotation aligned with the subject's elbow. This eliminated possible wrist pronation/supination. In most subjects no difference was seen with and without the revolute joint support. Data with significant pronation/supination were thrown out. Ideally, additional IREDs should have been used to correct for non-planar motion, but the current Optotrak^{TM}'s limited bandwidth did not allow this.

9.4.4 Data Acquisition and Filtering

A real-time VME-based microprocessor system [156] was used to collect all data and also control the experimental stimuli. The sampled data were usually low pass filtered off line at 50 Hz. Additional filtering was applied as needed. All filtering was based on a recursive $12th$ order Butterworth filter with a normalized cutoff frequency of 0.1 [157, pg. 218]. Low pass, band pass and high pass filters of arbitrary frequencies were

obtained with the transformations in [157, pg. 238]. Phase distortion was eliminated by running the filter over the data twice: once in the normal manner, and then again with the data time reversed.

9.5 Perturbation Calculation

9.5.1 Alignment and Removing the Mean

For each subject and movement condition, joint angle position profiles were obtained by (1) chopping the data into single 'movements' $\theta_i(t)$ of one cycle each (where $i = 1$ to n, and n is the number of movements made), (2) initially aligning the movements by peak velocity, (3) computing a mean movement profile, (4) re-aligning each movement so as to minimize the root mean square, RMS, difference between the mean profile and the movement $\theta_i(t)$, and (5) re-computing a mean movement profile with the re-aligned data to give the final mean movement profile $\theta_0(t)$.

Steps (4) and (5) were sometimes repeated to improve the average RMS difference between the movements and the mean, but iteration was usually not necessary, and did not affect the final parameter estimates. Corresponding torque profiles were obtained by chopping torque data up at the alignments computed for the angle data, computing a mean torque profile, and removing this mean from each torque profile. The final result gives n single movement position and torque trajectory profiles $(\theta_i(t), \tau_i(t)$, where $i = 1$ to $n)$, a mean position profile and a mean torque profile $(\theta_0(t), \tau_0(t))$, and n movement perturbation position and torque profiles $(\Delta\theta_i(t), \Delta\tau_i(t)$, where $i = 1$ to $n)$. Figure 10-2 shows typical movement data before and after removing the mean.

9.5.2 Posture Perturbation Estimates

In the case where the subject was asked to maintain a fixed posture, the dynamics were linearized about the mean arm position, θ_0. Thus, $\Delta\theta(t) = \theta(t) - \theta_0$. Likewise, $\Delta\tau(t) = \tau(t) - \tau_0$.

9.6 Time-Varying System Identification

The perturbation dynamics (7.9) were identified by finding the best parameter estimates $I(t)$, $B(t)$, and $K(t)$ that satisfy the ensemble of measured perturbations at each fixed point in time. The method is summarized as follows: (1) (7.9) is discretized, (2) an optimization criteria is specified, (3) the discrete time parameters are optimally estimated, and (4) the continuous time parameters and parameter variances are estimated from the discrete time estimates.

9.6.1 Discretization

The sampled data collected in the experiment should satisfy a general discrete time auto-regressive moving average (ARMA) model:

$$
\begin{aligned}
0 = \ & a_0(t)\Delta\theta(t) + a_1(t)\Delta\theta(t-h) + a_2(t)\Delta\theta(t-2h)... \\
& +b_0(t)\Delta\tau(t) + b_1(t)\Delta\tau(t-h) + b_2(t)\Delta\tau(t-2h) + ...
\end{aligned}
\tag{9.3}
$$

where $h = 1.67ms$ is the sampling interval, the a_i are the auto-regressive parameters, and the b_i are the moving average parameters.

To relate the continuous time model (7.9) to (9.3) a simple method is to use the Euler approximation of a derivative:

$$
\dot{\theta}(t) = \frac{\theta(t+h) - \theta(t)}{h}
\tag{9.4}
$$

Substituting (9.4) into (7.9) gives:

$$
\Delta\tau(t) = a_0(t)\Delta\theta(t) + a_1\Delta\theta(t+h) + a_2(t)\Delta\theta(t+2h)
\tag{9.5}
$$

where the linear relationship between $(I(t),\ B(t),\ K(t))$ and $(a_1(t),\ a_2(t),\ a_3(t))$ is easily derived.

A more accurate method to discretize (7.9) is to view the data as coming from

a sampled data zero-order-hold (ZOH) process, and integrate (7.9) over each sample interval [158], giving:

$$0 = \Delta\theta(t-h) + a_1(t)\Delta\theta(t-h) + a_2(t)\Delta\theta(t-2h)$$
$$+ b_1(t)\Delta\tau(t-h) + b_2(t)\Delta\tau(t-2h) \qquad (9.6)$$

where the relation between $(I(t), B(t), K(t))$ and $(a_1(t), a_2(t), b_1(t), b_2(t))$ is non-linear (see page 52 in [158] for the inverse of the relation below):

$$K(t) = \frac{a_1(t) + a_2(t) + 1}{b_1(t) + b_2(t)}$$
$$B(t) = \frac{2zK(t)}{w_0} \qquad (9.7)$$
$$I(t) = \frac{K(t)}{w_0^2}$$

where $z = \sqrt{f/(1+f)}$, $w_0 = w\sqrt{1+f}$, $f = (1/ag - K(t)b_1(t)/ag - b/g)^2$, $g = sin(wh)$, $w = cos^{-1}(b)/h$, $b = -a_1(t)/2a$ and $a = \sqrt{a_2(t)}$.

Exogenous variables [158] for modeling the noise process were not used. Instead, the following parameter identification method was found to be adequate.

9.6.2 Parameter Identification with Input and Output Noise

At each fixed point in time t the ARMA parameters $(a_1(t), a_2(t), b_1(t), b_2(t))$ in (9.6) are constant for all n movements (where $n = 300$ for the 750 ms movements). These n linear equations in four unknowns may be solved in a number of ways.

A standard method is to assume that all of the error enters additively into the output $\Delta\theta(t)$, and find the parameters that minimize the mean squared error between the measured and predicted joint angles:

$$\sum_{i=1}^{n}(\Delta\theta_i(t) - \Delta\theta_i^{model}(t))^2 \qquad (9.8)$$

135

where for the model (9.6):

$$-\Delta\theta_i^{model}(t) = a_1(t)\Delta\theta_i(t-h) + a_2(t)\Delta\theta_i(t-2h)$$
$$+b_1(t)\Delta\tau_i(t-h) + b_2(t)\Delta\tau_i(t-2h)) \qquad (9.9)$$

and the subscripts i indicate the movement number. The problem with this linear least squares (LLS) method is that even if the measurements were corrupted only by ideal Gaussian white noise (GWN), the parameter estimates are biased because of (a) the auto-regressive terms (a_1 and a_2) and (b) input as well as output noise [158].

An improved method is developed by assuming that the input and output are corrupted by equal variance independent GWN [159]. Under these assumptions Koopman [159] developed a simple unbiased estimator of the ARMA parameters (though not optimal in the Maximum-Likelihood sense). The method is analogous to the procedure for fitting a multi-dimensional plane to data. Rewrite (9.6) for all movements as

$$\underline{0} = \begin{bmatrix} \Delta\theta_0(t) & \Delta\theta_0(t-h) & \Delta\theta_0(t-2h) & \Delta\tau_0(t-h) & \Delta\tau_0(t-2h) \\ \Delta\theta_1(t) & \Delta\theta_1(t-h) & \Delta\theta_1(t-2h) & \Delta\tau_1(t-h) & \Delta\tau_1(t-2h) \\ \cdot & \cdot & \cdot & \cdot & \cdot \\ \Delta\theta_n(t) & \Delta\theta_n(t-h) & \Delta\theta_n(t-2h) & \Delta\tau_n(t-h) & \Delta\tau_n(t-2h) \end{bmatrix} \begin{bmatrix} 1 \\ a_1 \\ a_2 \\ b_1 \\ b_2 \end{bmatrix}$$

$$(9.10)$$

or more compactly:

$$\underline{0} = J\underline{p} \qquad (9.11)$$

Thus, $\underline{p}$ may be considered to be the normal to a plane in 5-dimensional space. Let the mean squared normal distance λ from the data to the plane be:

$$\lambda = d^2 = \frac{\underline{p}^T J^T J \underline{p}}{\underline{p}^T \underline{p}} \tag{9.12}$$

The normal $\underline{p}$ that minimizes λ is:

$$\underline{p} = \text{the } jth \text{ eigenvector of } J^T J \tag{9.13}$$

where the jth eigenvalue is the smallest eigenvalue (which also happens to be λ, conveniently giving a measure of the model fit). The elements of $\underline{p}$ given by (9.13) provide the required ARMA parameter estimates. The eigenvector is readily obtained by singular value decomposition (SVD) of J without forming $J^T J$, thus avoiding numerical error accumulation associated with the $J^T J$ operation [58].

An estimate of the ratio of the input to output noise variance is necessary in order to scale the input measurements to achieve the assumed equal noise variance. For the data studied here, this ratio was typically set at 1.0, although changing it to any value between 0.01 and 100.0 did not appear to effect the results.

The assumption that GWN is acting on the measurements is not as restrictive as it appears. As the measurements for each trial come from movements separated by more than one second it is reasonable to assume that noise across trials is independent. Only the data within three samples on a particular movement may be correlated (i.e., there may be correlated noise acting on $\Delta\theta_i(t), \Delta\theta_i(t-h), \Delta\theta_i(t-2h), \Delta\tau_i(t-h)$, and $\Delta\tau_i(t-2h)$).

9.6.3 Time-Varying Impulse and Frequency Responses

The time-varying impulse response may be modeled using (9.3) with $a_0(t) = -1$, $a_l(t) = 0$ for $l > 0$, and $b_l(t)$ not necessarily zero for lags l up to several times the system response time. Parameter estimation may be carried out by an appropriately modified (9.10), or by the linear least squares (LLS) method. Here LLS is chosen as

there are no auto-regressive terms. In matrix form (9.3) is:

$$
\begin{bmatrix} \Delta\theta_0(t) \\ \Delta\theta_1(t) \\ \cdot \\ \cdot \end{bmatrix} = \begin{bmatrix} \Delta\tau_0(t) & \Delta\tau_0(t-h) & \Delta\tau_0(t-2h) & . & . & . \\ \Delta\tau_1(t) & \Delta\tau_1(t-h) & \Delta\tau_1(t-2h) & . & . & . \\ \cdot & \cdot & & \cdot & . & . & . \\ \cdot & \cdot & & \cdot & . & . & . \end{bmatrix} \begin{bmatrix} b_0(t) \\ b_1(t) \\ \cdot \\ \cdot \end{bmatrix} \quad (9.14)
$$

or more compactly:

$$
\underline{y} = J_l \underline{p_l} \quad (9.15)
$$

and the LLS solution is

$$
\underline{p_l} = (J_l^T J_l)^{-1} J_l^T \underline{y} \quad (9.16)
$$

Notice that $J_l^T J_l$ and $J_l^T \underline{y}$ are respectively the ensemble auto- and cross-correlations. The time-varying frequency response can be estimated by Fourier transforming the impulse response $\underline{p_l}$ at each fixed point in time.

The problem associated with this analysis is that at each time instant there are at least 180 parameters (i.e., $b_l(t)$ with $l = 0$ to 179 for a 300 ms long impulse response at the 600 Hz sampling rate), but only 200 to 300 equations (movements) to use in the estimation. Thus, as a result of noise, J_l typically is not of full rank and the solution (9.16) is undefined.

To generate more equations it is reasonable to assume that the dynamics are time-invariant within fixed time windows w ($w = 60ms$). Thus, within a window n equations of the form (9.14) hold at each of the wf_s (=37) sample times. Thus, there are $wf_s n$ (= 37n) equations with which to estimate the fixed ARMA parameters in a given window.

Even with the windowing technique described in the previous paragraph, it was found that for the data obtained in these experiments J_l was still not of full rank. To uniquely define a solution the squared Euclidean norm of $\underline{p_l}$ may be minimized

simultaneously to minimizing the mean squared modeling error:

$$(\underline{y} - J_l \underline{p}_l)^T (\underline{y} - J_l \underline{p}_l) + \lambda \underline{p}_l^T \underline{p}_l \qquad (9.17)$$

This minimization may be implemented by ridge regression [160], or equivalently with the singular value decomposition SVD approach described in [58]. (For the SVD method, any singular value less than 10^{-4} of the maximum singular value was zeroed.) As this solution is only of mathematical convenience and the real problem is one of having too many parameters to be estimated, the impulse response estimates are of questionable value and were only e¦imated for a few data sets (see Figure 10-7 in the results section). Perhaps a better solution would be to minimize the norm of the discrete first or second derivative of the impulse response $\underline{p}_l$ (rather than the norm of $\underline{p}_l$), thus enforcing a smoothness constraint on the impulse response.

9.6.4 Posture Impedance Estimates and Ergodicity

In the case of the perturbation data collected during posture, the above system identification technique must be modified as there is only one input/output pair. To do this it is assumed that the system parameters $I(t)$, $B(t)$, and $K(t)$ are const· · ., , B, and K respectively. An equation of the form (9.3) with constant param· · ⸱ is describes the data. Therefore, combining the equations across time, rather than down the movement ensemble, is valid. With $\Delta\theta_i(t) = \Delta\theta(t - i)$ and $\Delta\tau_i(t) = \Delta\tau(t - i)$ substituted into (9.10) the constant vector $\underline{p}$ may be estimated and I, B and K recovered using (9.7).

Inspecting the elements of $J^T J$ reveals time-averaged cross-correlations and autocorrelations of the input and output variables. Effectively, the substitution of $\Delta\theta_i(t) = \Delta\theta(t - i)$ and $\Delta\tau_i(t) = \Delta\tau(t - i)$ turns the ensemble averaged correlations into time-averaged correlations. Thus, in a statistical framework the justification for this substitution is ergodicity (i.e., time averages equal ensemble averages). No assumption about the stationarity of the input signal $\Delta\tau(t)$ is used, although its sta-

139

tionarity would make the autocorrelation matrix (a submatrix of $J^T J$) Toeplitz in structure, which could be exploited to simplify the computation.

Analogously to the previous section, the impulse response during posture may be modeled by assuming a time-invariant system with a structure of (9.3) with $a_0 = -1$, $a_l = 0$ for $l > 0$, and b_l not necessarily zero for lags l up to several times the system response time (typically, at least 300 ms, or $l = 0$ to 179 for the 600 Hz sampling rate). Parameter estimation may be carried out using an appropriately modified (9.10). Alternatively, as no autoregressive terms exist to introduce parameter bias, linear least squares LLS may also be used (assuming no input noise). The LLS solution is equivalent to the standard correlation solution. The frequency response may be estimated by Fourier transforming the estimated impulse response.

9.6.5 Simulations

A critical part of any system identification technique is verification with simulated data. To simulate the experimental setup the forearm was modeled as a cylinder (mass and center of mass m and r) with inertia $I = 0.075 kgm^2$, the muscles were modeled as linear with constant stiffness $K = 20 Nm/rad$ and damping $B = 1.0 Nm/rad/s$, and the arm was considered to move in the vertical plane against gravity. The airjet was assumed to have a mass of $m_a = 0.2 kg$ acting at $r_a = .4m$ radius, giving an inertia of $I_a = .032 kgm^2$. Thus, without the airjet running the unperturbed dynamics are:

$$0 = I\ddot{\theta}(t) + I_a\ddot{\theta}(t) + B\dot{\theta}(t) + K(\theta(t) - \theta_0(t)) \tag{9.18}$$

$$-mgr\sin\theta(t) - m_a g r_a \sin\theta(t) \tag{9.19}$$

The motor input $\theta_0(t)$ is calculated so that the unperturbed dynamics (9.19) produce an arm trajectory $\theta(t)$ that is a 0.5 Hz sinusoid with a peak-to-peak amplitude of 1 rad (similar to the 1000 ms movement condition, where each cycle is one movement), and 100 cycles long.
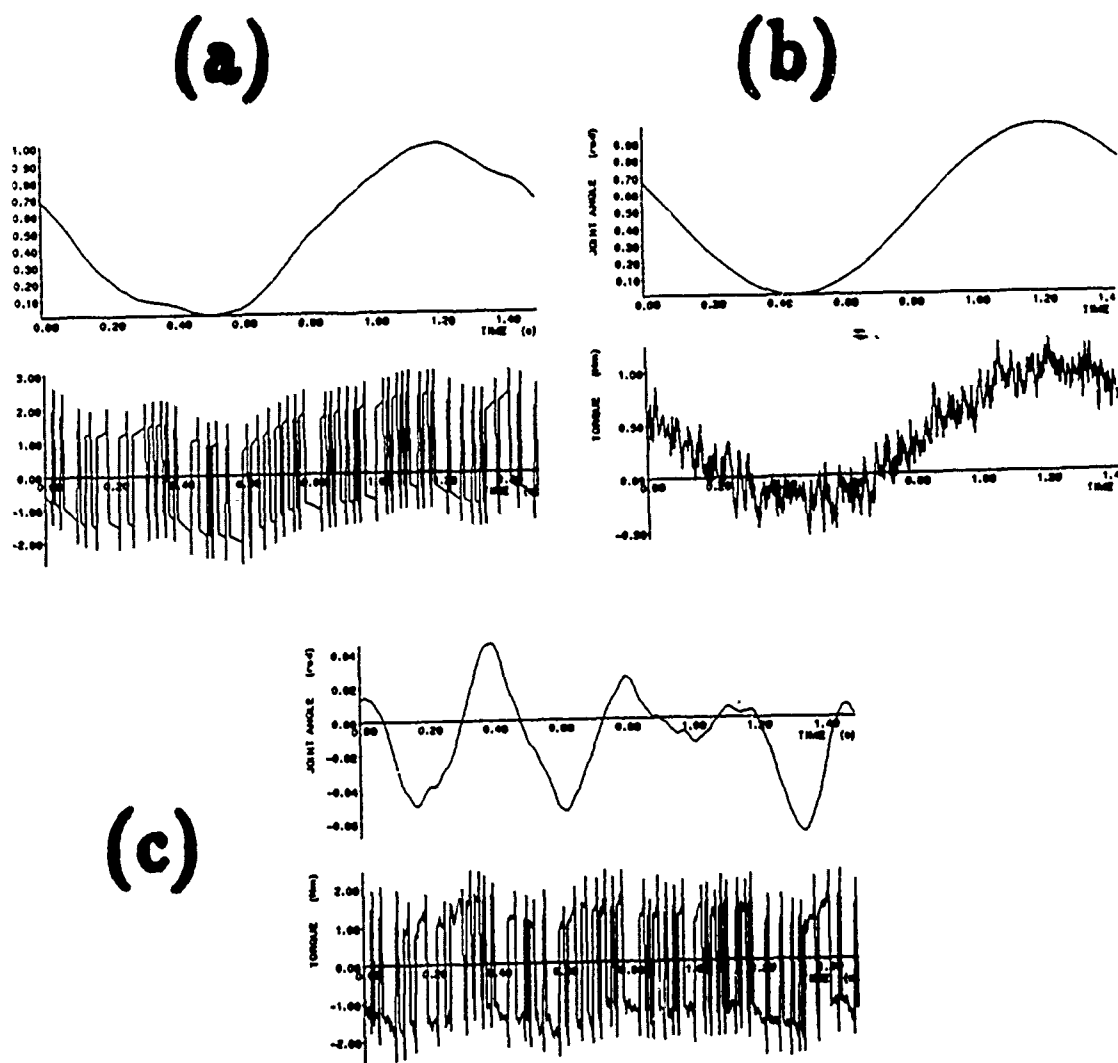
Figure 9-8: (a) Simulated perturbed movement profile, (b) mean movement profiles and (c) perturbations about the means.
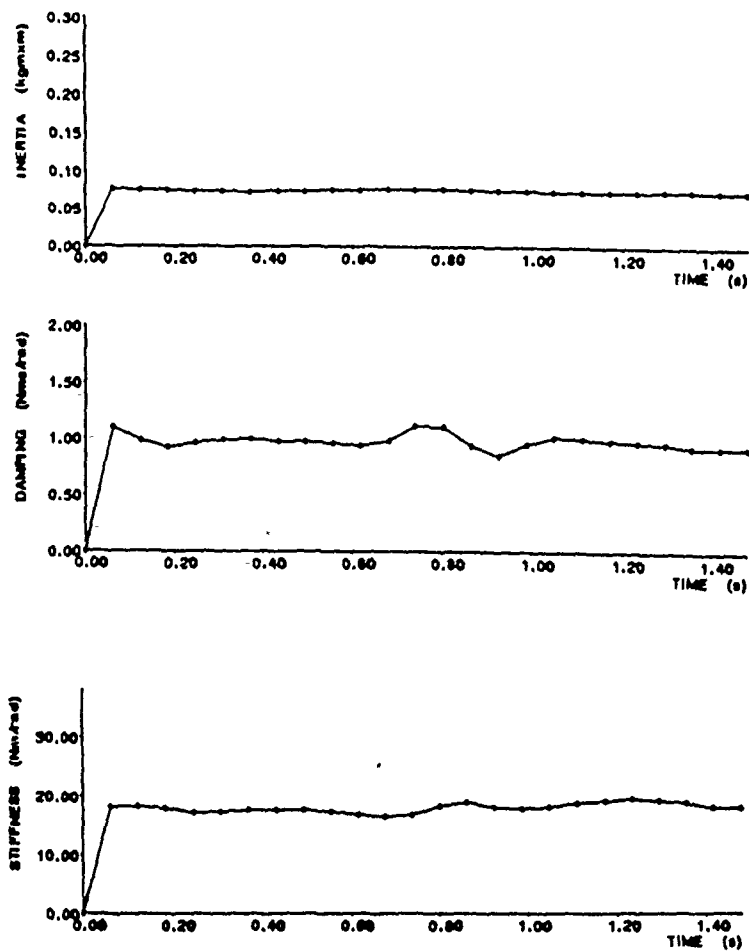
Figure 9-9: Estimated perturbation parameters from simulated data in Figure 9-8.

With the airjet running, the perturbed dynamics are:

$$\tau(t) = I\ddot{\theta}(t) + B\dot{\theta}(t) + K(\theta(t) - \theta_0(t)) - mgr\sin\theta(t) \qquad (9.20)$$

where $\tau(t) = \tau_{PRBS}(t) - I_a\ddot{\theta}(t) - m_a g r_a \sin\theta(t)$ is the force measured by the force sensor on the airjet mounting, and $\tau_{PRBS}(t)$ is a PRBS of ± 1.6 Nm. Using $\theta_0(t)$ and $\tau_{PRBS}(t)$ as input to a fourth order Runge-Kutta numerical integration [58] of (9.20), the perturbed joint trajectory $\theta(t)$ and perturbations measured by the force sensor $\tau(t)$ are computed.

The above procedure was used to generate simulated data. The data was then processed as in the experiments. That is, the simulated data $\theta(t)$ and $\tau(t)$ were chopped into single movements (one cycle each), and aligned with the technique described in Section 9.5.1. Mean movement profiles $\tau_0(t)$ and $\theta_0(t)$ and perturbations about the mean were computed. See Figures 9-8 (a), (b) and (c).

The perturbation parameters were then estimated using (9.13) (after introducing 5% GWN noise into the input and output data). See Figure 9-9. Notice that only the inertia of the arm I was estimated, not the total inertia of the airjet and arm. Also notice that the stiffness estimates are a little lower than $K = 20Nm/rad$, particularly near target 1 ($\theta = 0$). This is the effect of the negative gravity contribution to stiffness, as discussed after equation (7.9).

9.6.6 Apparatus Identification

The mass of the wrist cuff and the frame supporting the airjet contributes to the measured inertia. To estimate the inertial contribution of the whole apparatus it was supported on a light low friction revolute joint, such that the airjet was at the same distance and orientation relative to the joint that it typically is during the experiments. A PRBS input was applied by the airjet and measured as in Section 9.4. The acceleration was computed by 50 Hz low pass filtering the recorded joint angles and using the approximation (9.4) twice. The static relation $\tau = I_{cuff}\ddot{\theta}$ was then fit to the data to provide an apparatus inertia estimate of $I_{cuff} = 0.035kgm^2$.

9.6.7 Artificial Arm Identification

Using the same support joint for the airjet apparatus described in the previous section a simulated arm may be made by coupling the joint to a damper and/or spring. Using only a damper (see Appendix) a simulated experiment was performed where the airjet was switched with a PRBS with 20 ms elements. The method of section 9.7.2 was used with (9.13) to estimate the perturbation parameters, giving: $I = 0.04kgm^2$, $B = 1.20Nm/rad/s$ and $K = 0.91Nm/rad$. These estimates agree well with the inertia estimate of the previous section and the specification sheet provided by the manufacturer of the damper (see Appendix). In an independent test a 4 N step response also gave a similar damping estimate (1.3 $Nm/rad/s$). The small stiffness could be due to the restoring forces provided by the air supply lines.

Chapter 10

Results of Airjet Perturbation Experiments

10.1 Posture

The angle dependence of perturbation parameters estimated during posture (see Section 9.6.4) is shown in Figure 10-1. The plotted values show the mean and standard deviations of six estimates made from separate 5 s trails where subjects were instructed to point at a fixed target location. For the horizontal movements there is little dependence of these perturbation parameters on the joint angle. For the vertical movements the stiffness increases slightly with joint angle.

The torque variance accounted for (VAF) by the second order perturbation model was computed for each trial, and is consistently above 80% (where the VAR/100% is defined as one minus the ratio of the variance of the model's error in estimating torque to the variance of the torque data). Frequency responses and coherence functions were calculated for all subjects. The coherence was always above 95% up to 50 Hz.

10.2 Horizontal 750ms Movements

In this and following sections we now consider how the mechanical properties are modulated under various movement conditions. First we focus on the horizontal
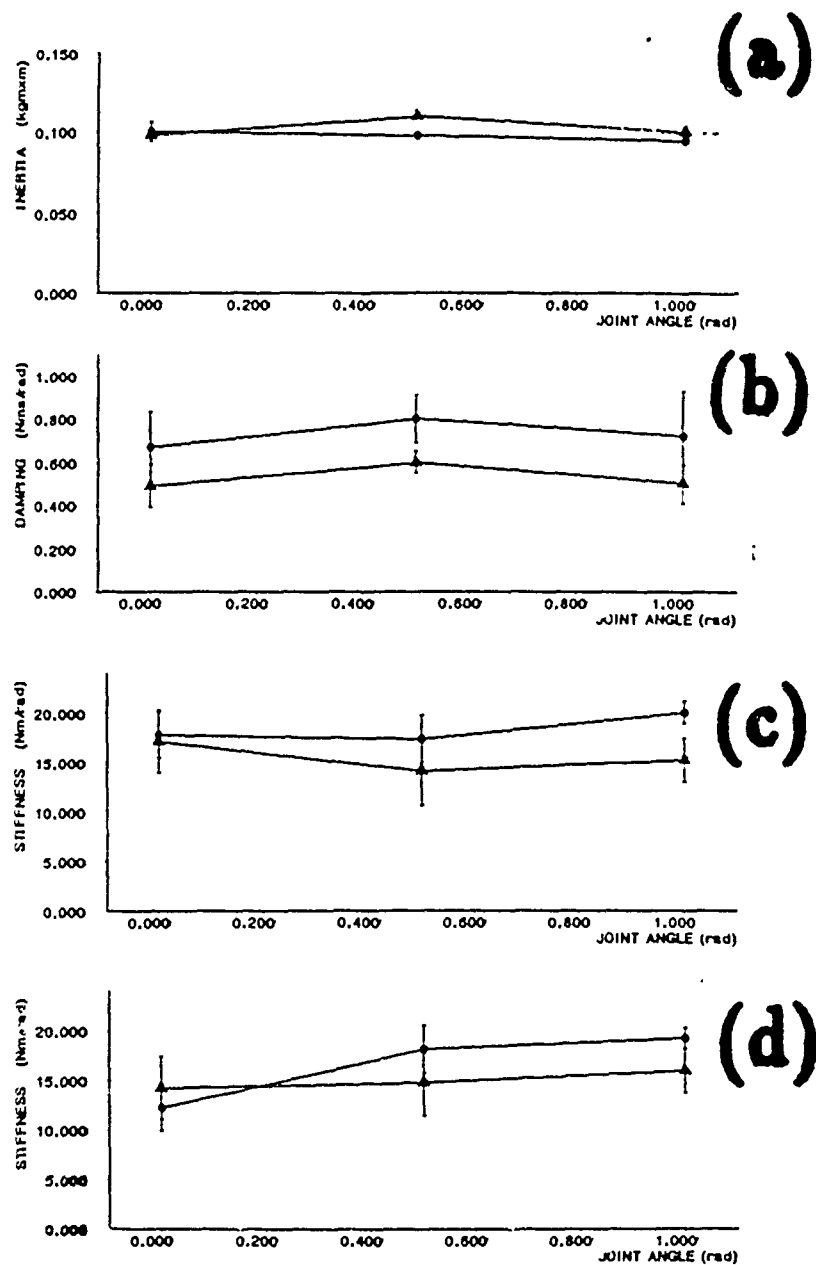
Figure 10-1: Joint angle versus mean (a) inertia, (b) viscosity and (c) stiffness for Subject S1 asked to maintain fixed postures in the vertical plane (marked with circles) and horizontal plane (marked with triangles). (d) Joint angle versus mean stiffness for Subject S2. Error bars show standard deviations about the means.

plane 750 *ms* movements.

10.2.1 Typical Movement Data

Typical angle and torque measurements are shown in Figure 10-2 for two subjects. Figure 10-3 shows the corresponding perturbations computed by removing the ensemble means (re Section 9.5.1).

10.2.2 Main Results

The time-varying parameter estimates made using the perturbations from 300 movements and (9.13) are shown in Figure 10-4 (See Figure 10-6 also). The mean parameter values and standard deviations computed over 60 *ms* windows are shown. The data are repeated for an extra cycle to emphasize that the estimates are periodic. The corresponding damping ratios $(B/(4KI)^{0.5})$ are shown in Figure 10-5. The features in Figures 10-4 and 10-5 that are typical across all subjects and conditions are:

1. *The stiffness is modulated with the movement. It reaches a peak value just before the arm comes to rest at a target and drops to a minimum value before the peak velocity of movement is reached.*

2. *The stiffnesses are low, lower than the smallest values measured during posture.*

3. *The stiffness values at the two targets are sometimes unequal (usually higher at target 2 when gravity is present).*

4. *There is a tendency for the damping to drop slightly while the arm is at a target. The damping estimates have considerable variation across subjects though.*

5. *The damping ratio is not constant, ranging from 0.2 to 0.6 during the movement.*

6. *The inertia estimates are constant and agree with previous estimates of forearm inertia. The values shown include the apparatus inertia of $0.035 kgm^2$.*

147
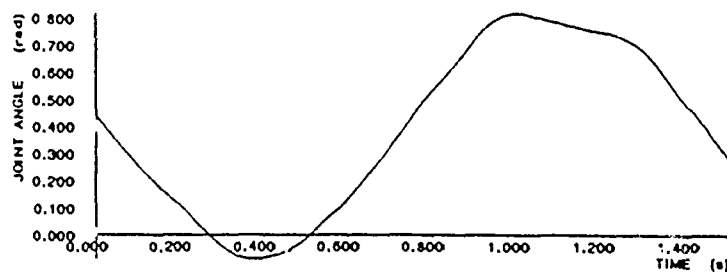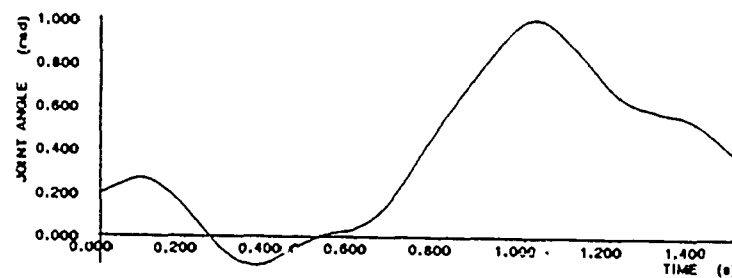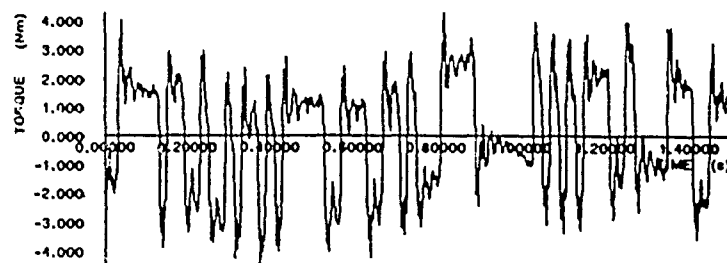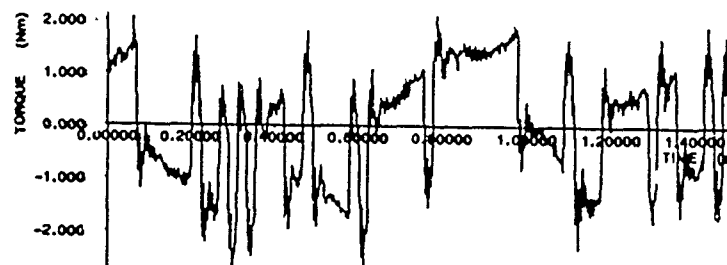
Figure 10-2: Typical horizontal plane elbow angle and torque profiles for subject S1 and subject S2. Each plot represents a full cycle taken from a rhythmic oscillation of the forearm in time to a periodic auditory stimulus (period 750 *ms* and duration 30 *s*). Targets to oe hit were at 0.0 *rad* and 1.0 *rad*.
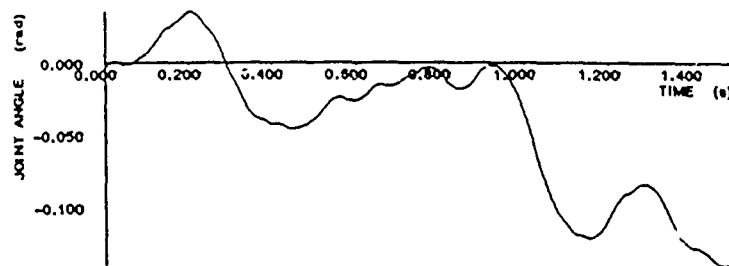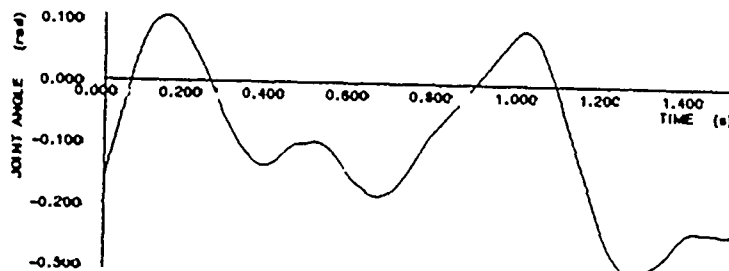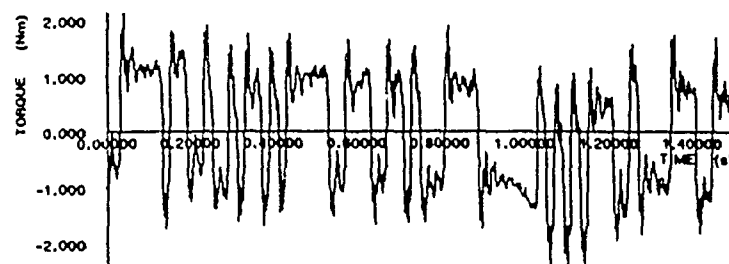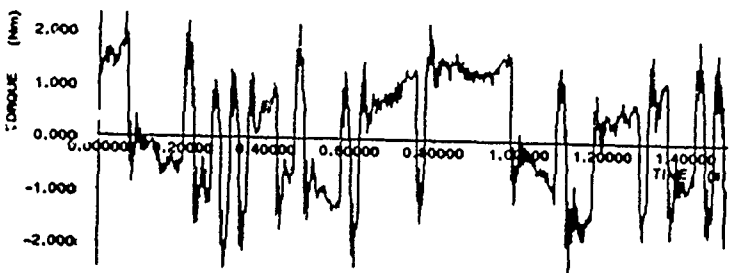
Figure 10-3: Typical horizontal plane elbow joint perturbations about the ensemble means for subject S1 and subject S2. Perturbations were computed by subtracting the mean of 300 movements from the trajectories in Figure 10-2.
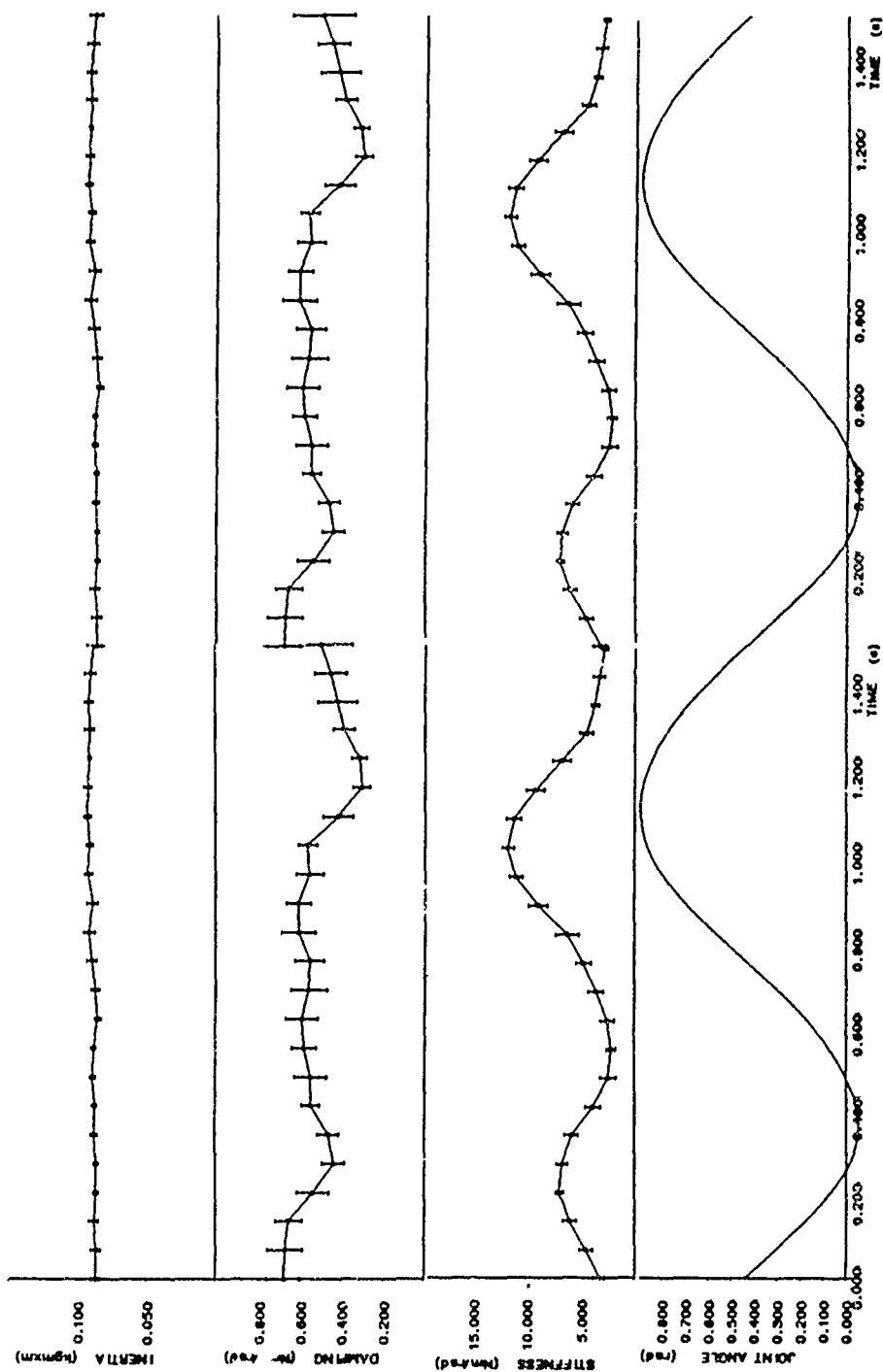
Figure 10-4: The estimated time-varying perturbation model for subject S1 moving in the horizontal plane in time to a 750 ms auditory stimulus. The mean parameter values and standard deviations computed over 60 ms windows are shown. The data are repeated for an extra cycle to emphasize that the estimates are periodic.
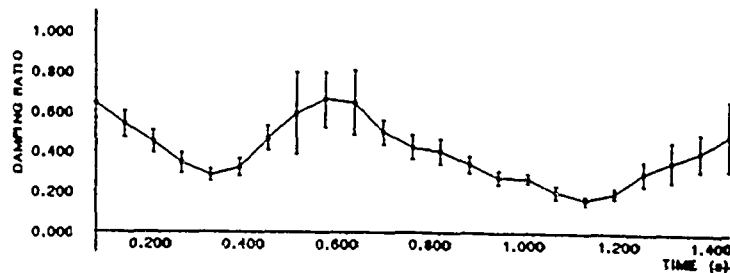
Figure 10-5: Figure 10-4 continued. Damping ratio profile.

The stiffness variations mentioned above cannot be simply due to passive connective tissue or skeletal moment arm changes, as the stiffness values measured during posture do not vary with joint angle (over the range studied).

10.2.3 VAF

The torque variance accounted for (VAF) by the model parameters in Figure 10-4 is 76%. Across all conditions and subjects the VAF by the time-varying second order system parameters exceeds 70%. Most of this error is due to voluntary variation in the trajectory from movement to movement, which effectively introduces low frequency noise into the data.

10.2.4 Frequency Responses and Natural Frequencies

Three samples of the time-varying frequency response (at (a) $\theta = 0.0\ rad$, (b) $\theta = 0.5\ rad$ on the extension movement, and (c) $\theta = 1.0rad$) are shown in Figure 10-7. These were estimated with the SVD method of Section 9.6.3 with a 60 ms window, and a Fourier transformation. The natural frequencies, as defined by the point at
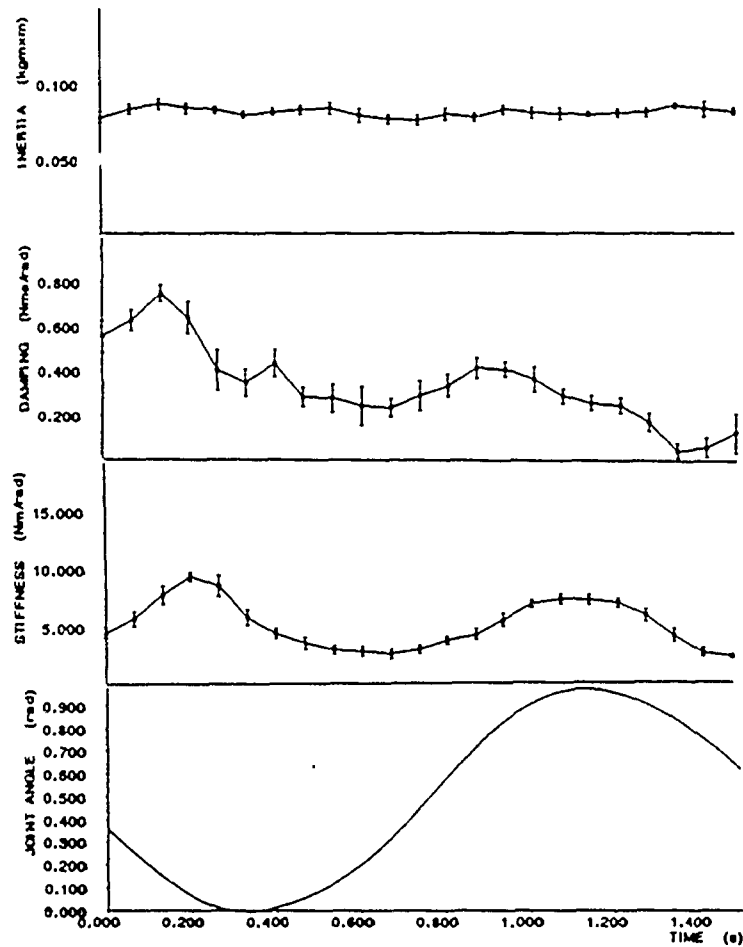
Figure 10-6: Same as Figure 10-4, except for subject S2.

152

which the phase angle crosses -90 degrees, are respectively (a) 1.77 Hz, (b) 0.63 Hz, and (c) 2.51 Hz. The corresponding natural frequencies computed from the second order system parameters are respectively (a) 1.50 Hz, (b) 1.06 Hz, and (c) 2.05 Hz (where the natural frequency f_n is defined as $2\pi f_n = (K/I)^{0.5}$). This second method of natural frequency estimation is superior in view of the problems mentioned earlier in connection with estimating the time-varying impulse response. By all measures, the natural frequency is always below 3 Hz.

10.2.5 Dominance of Inertia Above 5 Hz

To demonstrate the dominance of inertia above 5 Hz the data were filtered with a high pass filter with a 5 Hz cutoff frequency (see Section 9.4.4), and a static inertia model $\Delta\tau = I\Delta\ddot{\theta}$ was estimated. Figure 10-8 shows the measured torque (thin line) and the estimated torque $I\Delta\ddot{\theta}$ (dotted line) for a segment of the data. Both angle and torque data were also low pass filtered at 30 Hz in order to differentiate the angle data to get acceleration — thus the smoothness of the curves. The variance accounted for (VAF) by this constant inertia model was 95%, verifying that the system's natural frequency is below 5 Hz, and indicating that the inertia dominates the dynamics above 5 Hz.

10.2.6 Effect of Airjet Perturbation Frequency

Figure 10-9 shows results of an experiment in which subject S2 moved in the horizontal plane and was perturbed with the airjet switched at twice the usual frequency (10 ms elements in the PRBS). With this stimulus rate the input was white up to 50 Hz, but there was only half the power that there usually is between 0 and 25 Hz. Comparing Figures 10-6 and 10-9 shows that this increase in bandwidth and decrease in low frequency amplitude does not qualitatively affect the results. Quantitatively, the VAF in Figure 10-6 is 72% and the VAF in Figure 10-9 is 76%.
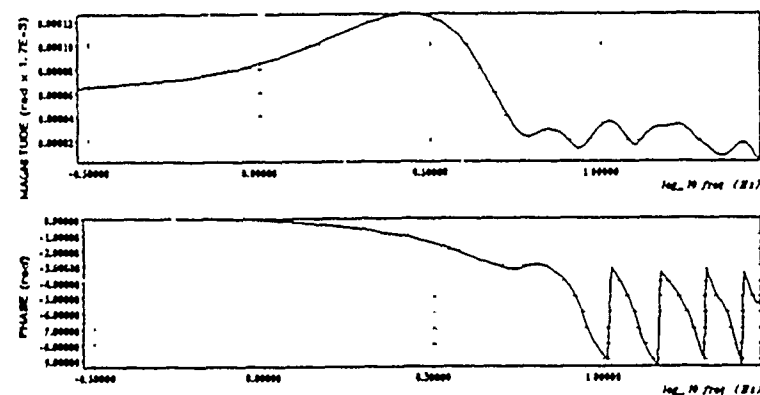
153
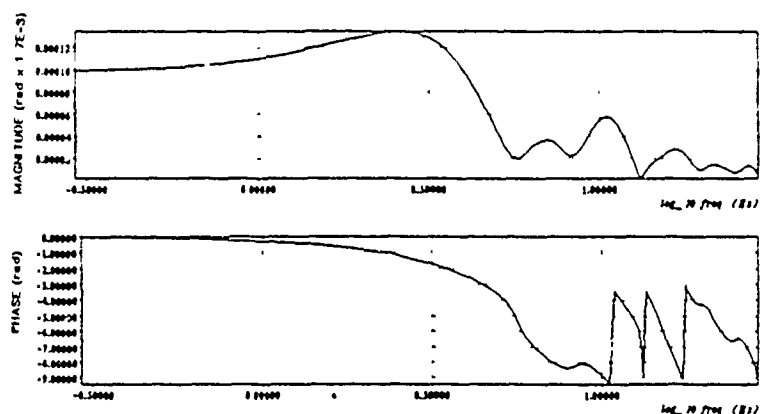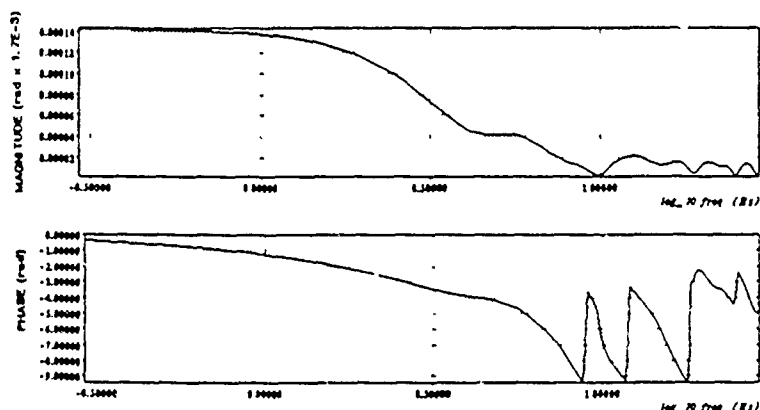
Figure 10-7: Time-varying frequency responses at (a) $\theta = 0.0rad$ (target 1), (b) $\theta = 0.5rad$ (on the extension movement), and (c) $\theta = 1.0rad$ (target 2). The natural frequencies, given by the point at which phase angle crosses -90 degrees, are respectively (a) 1.77 Hz, (b) 0.63 Hz, and (c) 2.51 Hz. Data are for subject S2 moving at the 750 ms rate in the vertical plane.
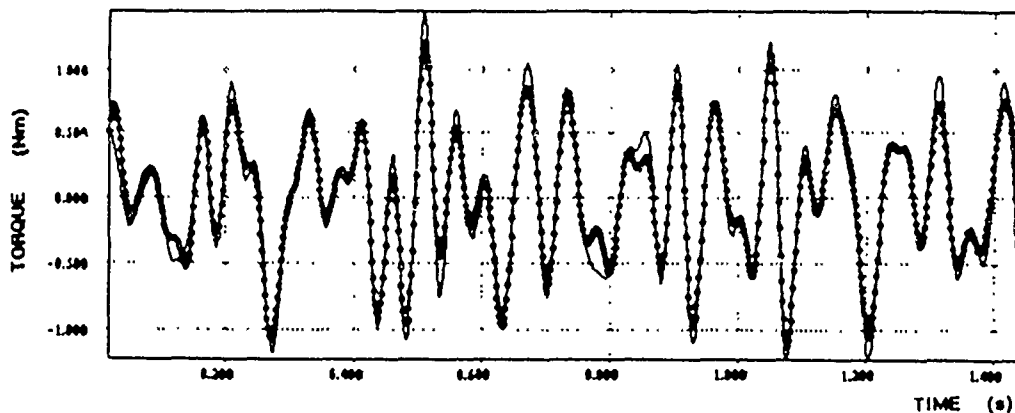
Figure 10-8: The data from Subject S1's horizontal movements (750 ms stimulus) were filtered at 5 Hz with a high pass filter, and a static inertia model $\Delta\tau = I\Delta\ddot{\theta}$ was estimated. Plotted above are the torques (thin line) and the estimated torques $I\Delta\ddot{\theta}$ (dotted line) for a segment of the data. The variance accounted for (VAF) by this constant inertia model is 95%, indicating that the inertia dominates the dynamics above 5 Hz.

10.3 Effect of Speed Change

The stiffness estimates increase slightly with a speed increase. Figure 10-10 shows typical results when moving between targets in the horizontal plane at the 0.5 Hz rate (1000 ms stimulus). Comparing this to the equivalent but faster 0.67 Hz movements in Figure 10-4 it is seen that the stiffness profiles are similar. The stiffness does not scale up by a factor equal to the square of the speed-up factor, which is $\times 1.78$. Figure 10-11 (also see Figures 10-15 and 10-17) compares the stiffness profiles for the two speeds for subjects S1 and S2.

10.4 Effect of a Viscous Damping Load

Figure 10-12 shows the results of attaching a damper to the arm during movement. Comparing these results to Figure 10-4 reveals that the damper more than doubles the damping that is normally measured in the unloaded joint (note that the damper
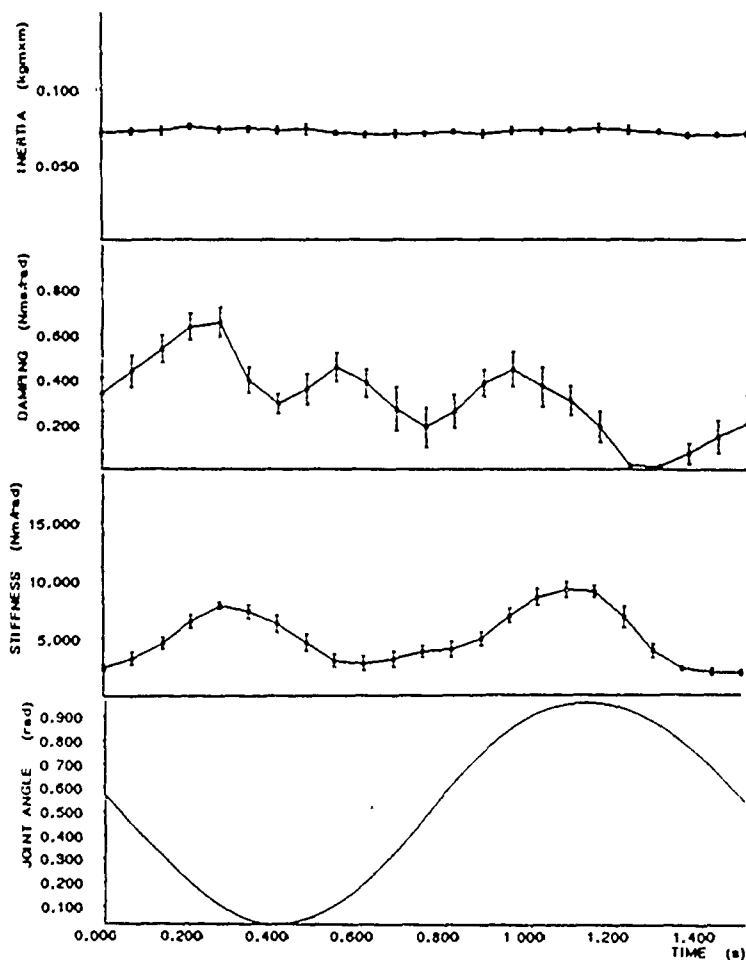
155

Figure 10-9: Same as Figure 10-6, except that the airjet was switched at twice the usual rate (10 *ms* elements in the PRBS). Data are for Subject S2.
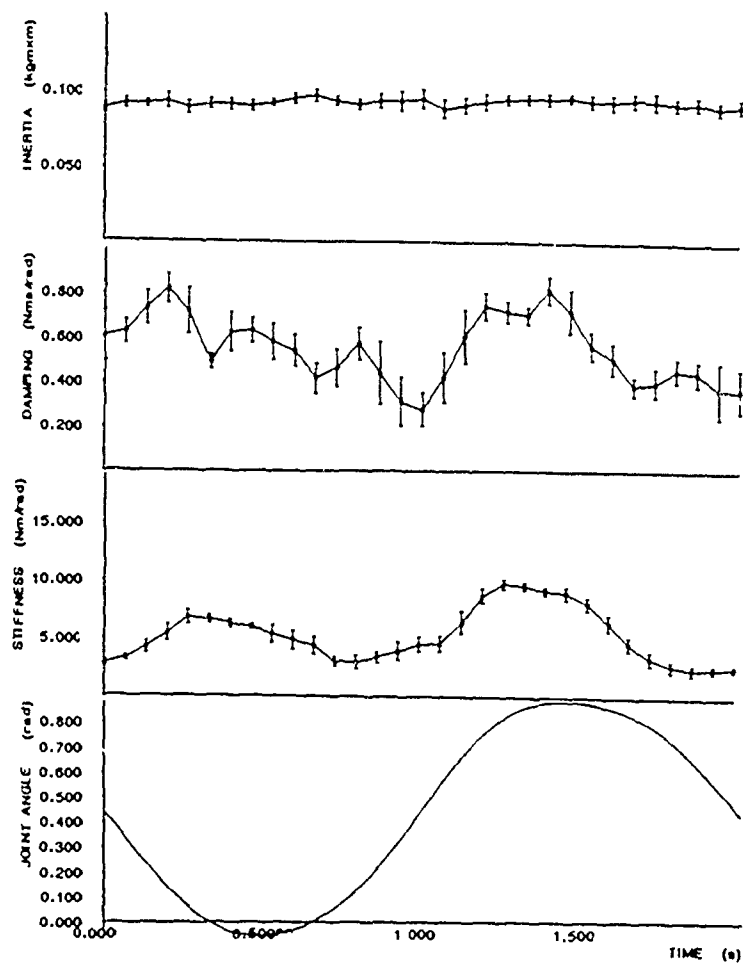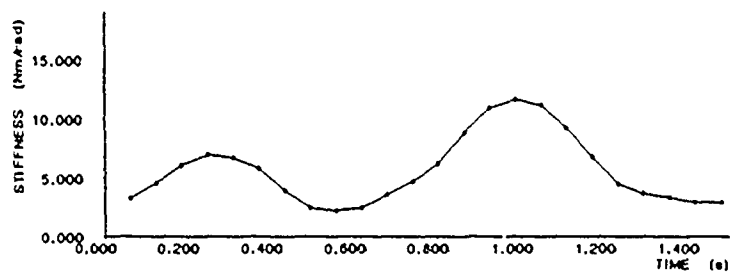
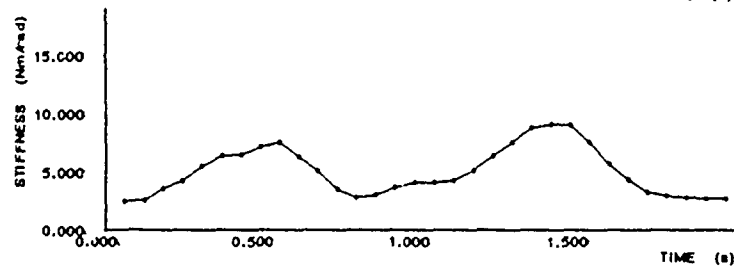Figure 10-10: Same as Figure 10-4, except with a 1000 *ms* period auditory stimulus. Data are for Subject S1.
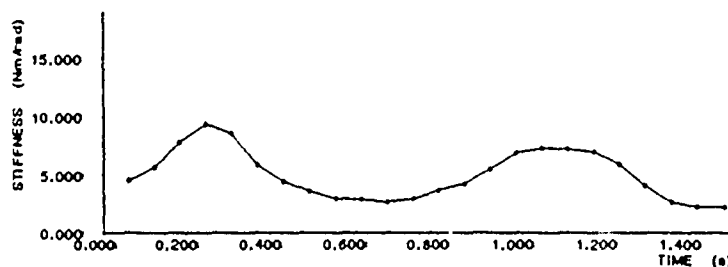
Figure 10-11: Stiffness profiles for two speed conditions for subjects S1 and S2 moving in the horizontal plane.

158

has a non-linear force-velocity relation shown in the Appendix — thus the higher damping at the targets). In spite of this increase in damping, the peaks in the stiffness profile are only increased by 20 percent, and the minimum stiffness during movement is unchanged. Effectively, the system's damping ratio is doubled, and there is no attempt to compensate.

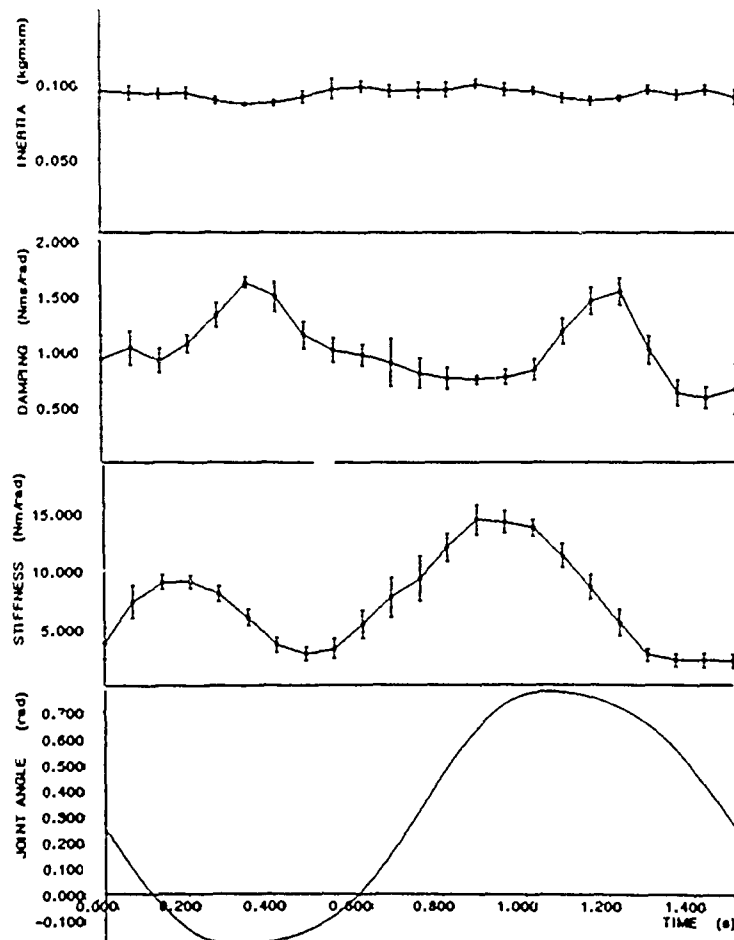Figure 10-12: Same as Figure 10-4, except with a viscous damper loading the arm. Notice that the scale on the damping is different. The damper load is non-linear (the damping drops slightly with increased velocity. See Appendix). Note that the stiffness profile is very similar to Figure 10-4. The inertia is a little larger than in Figure 10-4 because of the damper attachment. Data are for Subject S1.

10.5 Effect of Gravity

10.5.1 Stiffness Increases Due to Gravity

To observe the affect of gravity, analogous experiments to the horizontal plane experiments just described were performed in the vertical plane. Figures 10-13 and 10-14 show the results from subjects S1 and S2 moving in the vertical plane in time to the 750 ms auditory stimulus. Comparing these to the horizontal movements in Figures 10-4 and 10-6 reveals that the stiffness is higher at target 2 in the vertical plane movements. Note that the inertia estimates in the vertical movements are still constant, but are slightly higher in both subjects. This difference can be attributed to the cuff being mounted slightly further down the arm. This shift in mounting should not affect the stiffness or damping estimates.

To see the stiffness profile differences more clearly, the stiffness profiles from two subjects and speed conditions were plotted together in Figure 10-15. Comparing these results to the corresponding horizontal plane plots in Figure 10-11 reveals that there is a significant asymmetry in the vertical plane stiffness profiles. Unlike the horizontal plane movements the stiffness at target 2 (1.0 rad) is two to three times higher than at target 1 (0.0 rad). Notice that at target 2 the subject must resist the larger gravity force. This will be elaborated further in the next chapter.

As mentioned in Section 7.3 there is a small contribution to the measured stiffness that is due to gravity ($-mgc\cos\theta$). At vertical ($\theta = 0.0rad$) this contribution is highest. To see the size of this contribution it was computed for each angle and subtracted from the measured joint stiffnesses. The required mass and center of mass of the arm were estimated from the measured inertia using an assumption that the arm could be modeled by a cylinder. Figure 10-16 shows the stiffness profiles (a) before and (b) after making this gravity correction. Note that the difference does not account for the asymmetry in the stiffness peaks. As the difference between these two profiles is small, this gravity contribution will not be considered further.
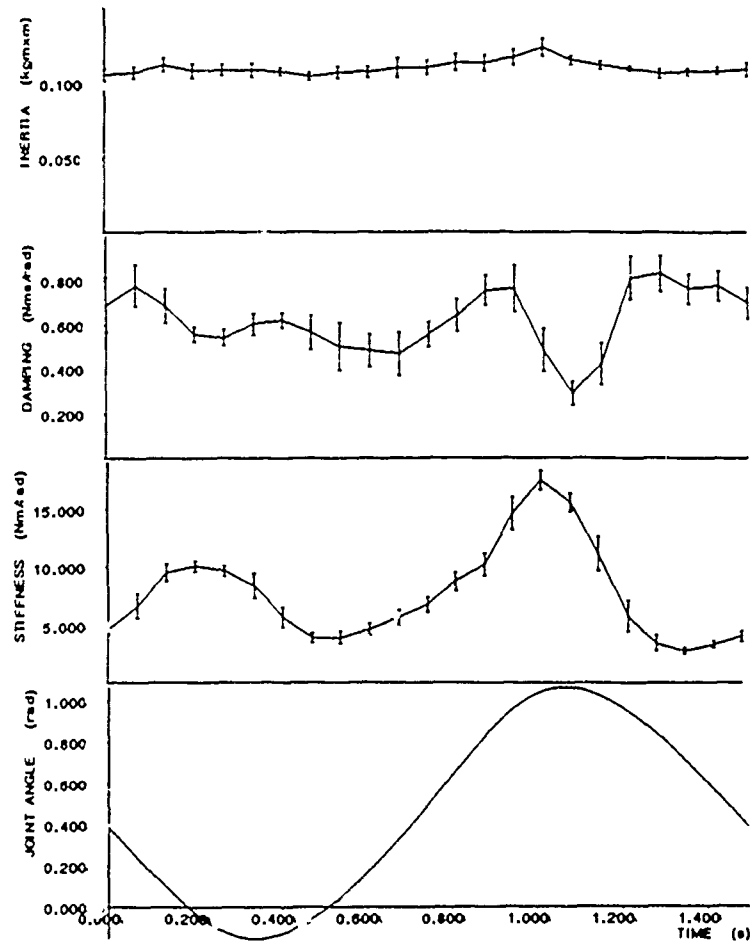
Figure 10-13: Same as Figure 10-4, except that the movement occurred in the vertical plane. Data are for Subject S1.
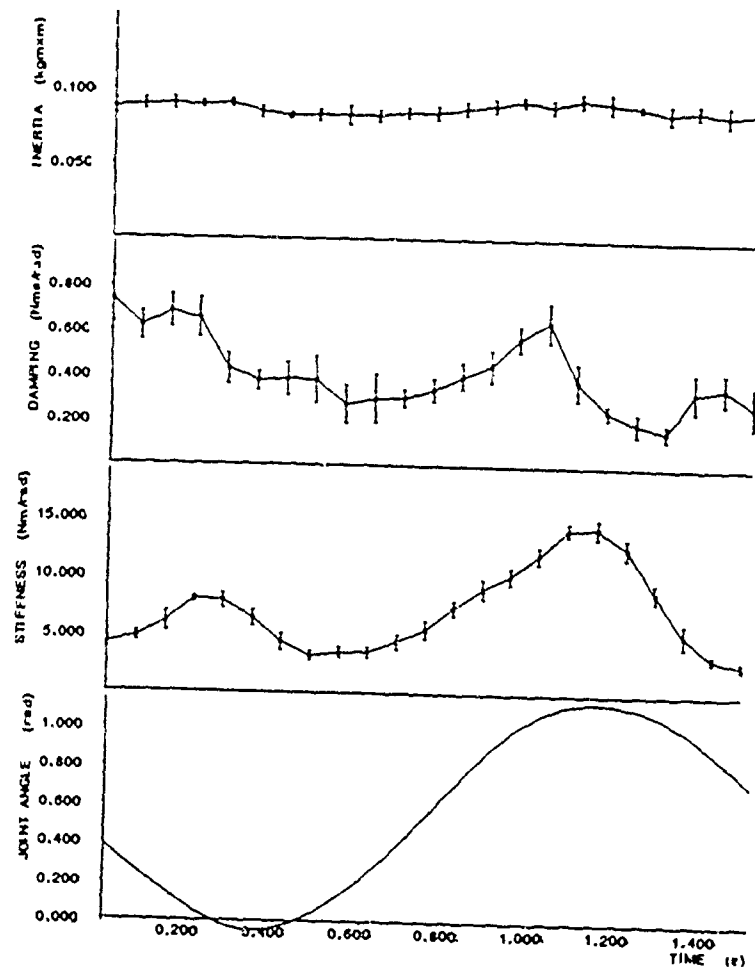
Figure 10-14: Same as Figure 10-6, except that the movement occurred in the vertical plane. Data are for Subject S2.
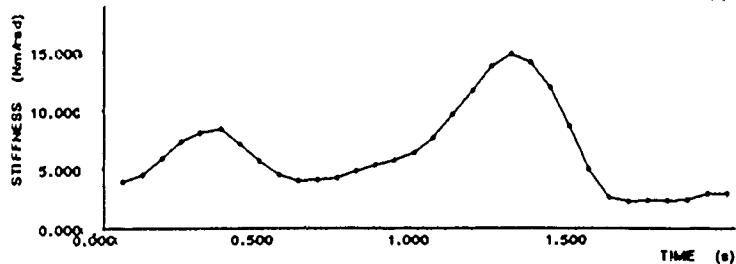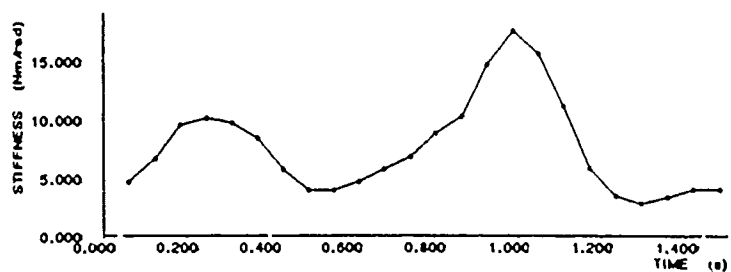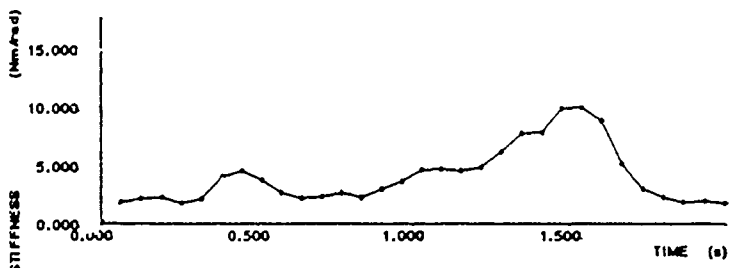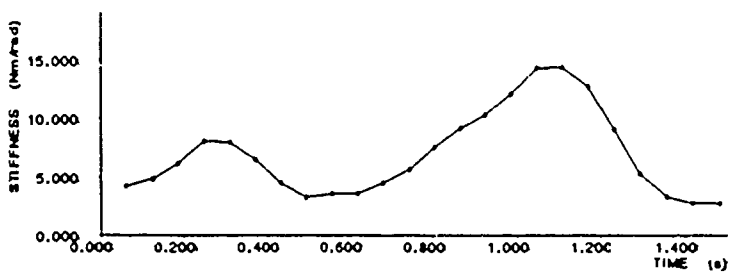
Figure 10 15: Same as Figure 10-11, except that the movement occurred in the vertical plane.
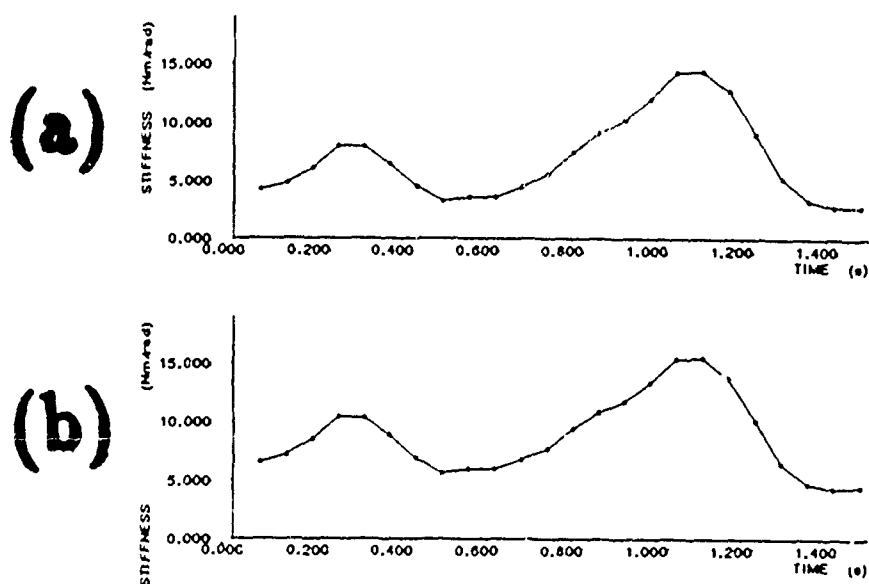
Figure 10-16: The negative gravity contribution to stiffness is small. Plot (a) shows the measured stiffness profile for the subject moving in the vertical plane and (b) shows the same profile with the gravity contribution to stiffness ($-mgc \cos \theta$) removed. Data are for Subject S2.

164

10.5.2 Effect of Speed Change Under Gravity

As with the horizontal movements, there is only a marginal increase in stiffness with an increased speed of movement in the vertical plane. Figure 10-17 shows the stiffness profiles for four subjects moving in the vertical plane at the two speeds.
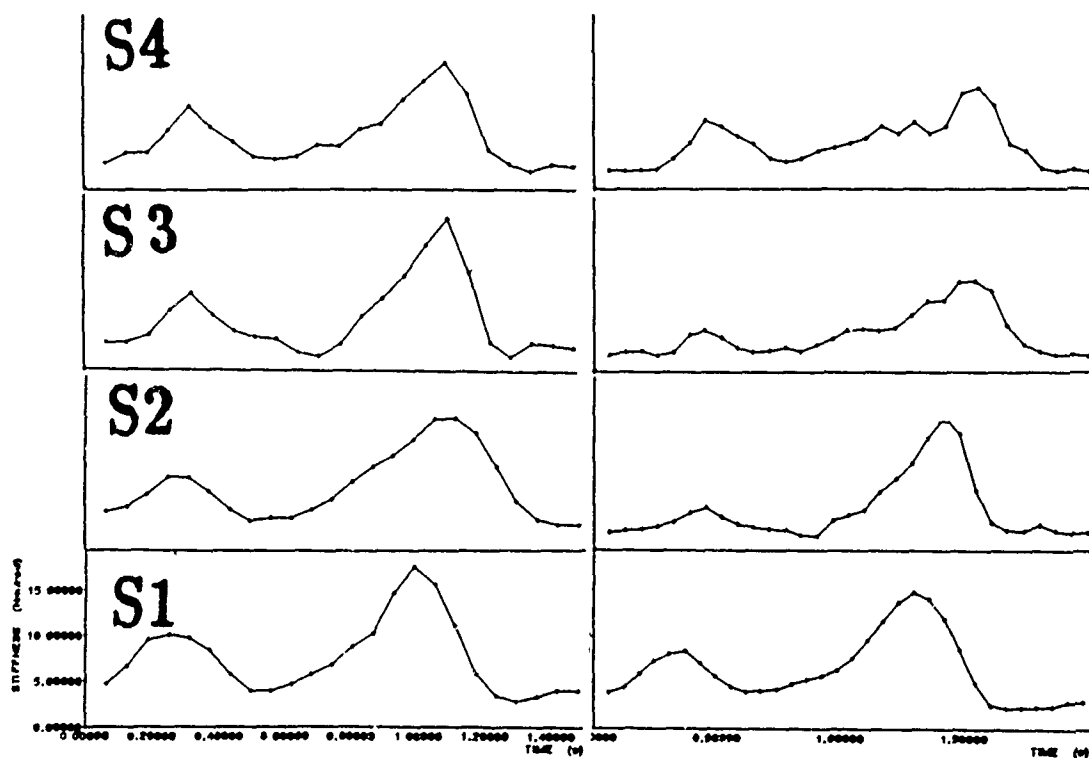
Figure 10-17: Stiffness profiles measured in the vertical plane at the two speeds. Subjects as indicated.

Chapter 11

Discussion

11.1 Relevance of Perturbation Estimates

An important issue that must be cleared up before proceeding is whether or not the mechanical impedance estimates are relevant to the formation of normal speed movement.

11.1.1 Short Range Stiffness

It might be argued that the low amplitude, high frequency input of the airjet only excites higher order dynamics that are not normally relevant to unconstrained movement (e.g., short range stiffness [105]). This argument is wrong for several reasons.

First, care was taken to use a sufficiently large perturbation force. In fact, the 1.6 Nm torque produced by the 4 N airjet thrust is comparable to the maximum net torque that the muscles produce in the movements studied, see Figure 11-1. Thus, for the segments of the PRBS in which the airjet is on in one direction for an appreciable portion of the movement time (say >100 ms) the arm effectively receives a step torque change comparable to the maximum net muscle torque.

Second, after the initial experiments that indicated that the arm's natural frequency was below 3 Hz, the airjet's minimum switching time was raised to 20 ms, providing more power at the low frequencies. Figure 9-3 shows that the majority of

the input power is evenly distributed between 0 and 25 Hz. As a qualitative indication of the low frequency power, it is mentioned that the airjet regularly perturbed the arm 5 to 10 degrees, and on occasion, for the arms of smaller subjects, displaced the arm the entire 60 degrees between targets (in these few cases the subject would abandon that movement).

Finally, the stiffnesses and corresponding natural frequencies measured in this thesis are much too low to be of only short range stiffness origin. As mentioned, the stiffness estimates give values for the system's natural frequency below 3 Hz. A separate corroboration of this low natural frequency comes from noticing that 95% of the variance may be accounted for by a pure mass model, if the input and output are high pass filtered above 5 Hz (Figure 10-8). If the airjet was probing only the short range stiffness, much higher natural frequencies estimates (stiffness estimates) would be expected. For example, the short range forearm stiffness estimates made by Lanman [130] (with high frequency 20-30 Hz sinusoidal inputs) are 5 to 10 times the values estimated in this thesis.

11.1.2 Spindle Reflex Sensitivity with Vibrations

The presence of the low amplitude high frequency content in the input PRBS may alter the muscle spindle sensitivity. The spindle response may be saturated (or clamped) by the vibrations, making them insensitive to larger, lower frequency stretch [161]. Perhaps there is a connection between this and the observation made in Chapter 8 that the damping ratios measured with PRBS inputs are lower (0.3 to 0.6) than those measured with single pulse inputs (0.8 to 1.0). There is no simple method to control for this problem, as the apparatus used can only produce binary force sequences. As much of the following analysis relates to relative stiffness changes with movement, these possible spindle sensitivity changes do not affect the conclusions.

11.2   Testing of Control Theories

The predictions (P1) to (P5) of Chapter 7 are now tested with the perturbation parameter measurements from Chapter 10.

11.2.1   Compliant Feedforward Control

First consider prediction (P1). It is clear from the horizontal movements in Figure 10-1 (and others like it) that, as predicted, the joint stiffness is low and only rises as the targets are approached. As discussed earlier, the finding that the stiffness is low suggests that feedforward control dominates. Further, joint stiffness rises exactly when it is required to reject disturbances in attaining the target; that is, it reaches a peak just before the target is attained. Once at the target no further accuracy is needed and the stiffness can drop immediately.

11.2.2   Stiffness and Force Modulation

As the arguments behind the compliant feedforward control hypothesis are purely functional, it is interesting to inquire into the mechanism behind the stiffness modulation. This will be attempted in the next section, but to start toward this goal we make the hypothesis that the stiffness changes are approximately proportional to muscle forces changes.

First, consider the horizontal movements. Assuming little co-contraction, the torque from the agonist muscles can be calculated to be the torque needed to accelerate the arm. As the acceleration is a maximum at the targets, the muscle torque is also at a maximum. Figure 11-1(a) shows the muscle torque required to accelerate the arm inertia (computed from the estimated inertia and average acceleration). Notice that indeed the stiffness goes up where the muscle torque is highest.

Further, comparing the two speed movements it is found that the stiffness is only higher in the faster movements near the targets. This is also true for the comparison between the computed net muscle torques at the two speeds; the difference is largest near the targets. In the middle of the movement the acceleration is zero, irrespective

168

of the speed. See Figure 11-1(a-b). The stiffness increase is not sufficient to conclude a strict proportionality with force, nevertheless t e stiffness does go up with muscle force increase.

Likewise, the muscle torque in the vertical movements can be calculated. In this case gravity also contributes to the torque. Figure 11-1(c) shows the computed net muscle torque (where tne computation uses the estimated inertia, a cylinder model of the arm to estimate the mass an center of mass from inertia, and the average trajectory). Notice that the stiffness is again highest where the muscle torques are highest. The muscle torques at the two targets are asymmetric, just as the stiffnesses are.

Unfortunately, this simple explanation for muscle stiffness changes is not complete. Consider the damper experiment. This experiment was specifically designed to test this force-stiffness explanation. The damper produces its largest torque in the middle cf the movement (at the peak velocity). Figure 11-1(d) shows the computed net muscle torques to oppose inertial acceleration and the damper load. But Figure 10-12 shows that the stiffness does not go up during movement, despite the large increase in torque during the movement. The stiffness does go up slightly, but only near the targets. Thus, the mechanism for stiffness modulation must be more complex than this simple monotonic force-stiffness relation. This may have been expected, as it was mentioned earlier that muscle force is velocity dependent. Also, reflex induced stiffness changes and co-contraction were ignored in the above arguments.

11.2.3   Speed Scaling and Feedforward Control

To further test the hypothesis that feedforward control dominates, consider the different speed movements again. If there was no feedforward compensation (other than perhaps static feedforward gravity compensation) then the effective feedback gains (as measured by the stiffness) would have to increase with the square of the speed increase (i.e., $\times 1.78$) to produce the same time scaled movement trajectory (i.e., prediction (P2)). In actuality, time scaled movement trajectories at the two speeds are the same (e.g., Figure 11-2(b-c)), and yet for the faster movement the peak stiffness

169
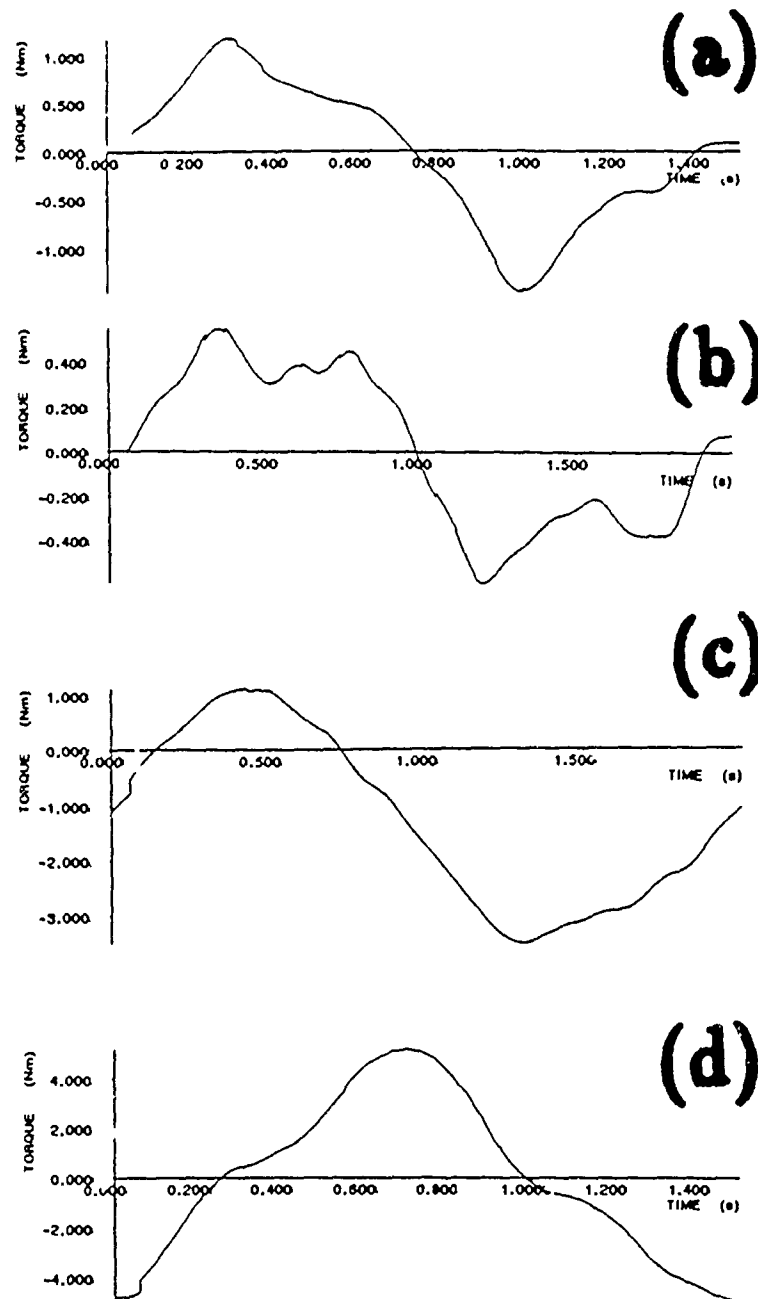
Figure 11-1: Torques that the muscles/tendons produce in subject S1 during (a) an average horizontal 750 *ms* movements, (b) an average horizontal 1000 *ms* movements, (c) an average vertical 1000 *ms* movement, and (d) an average horizontal 750 *ms* movement with a damping load.
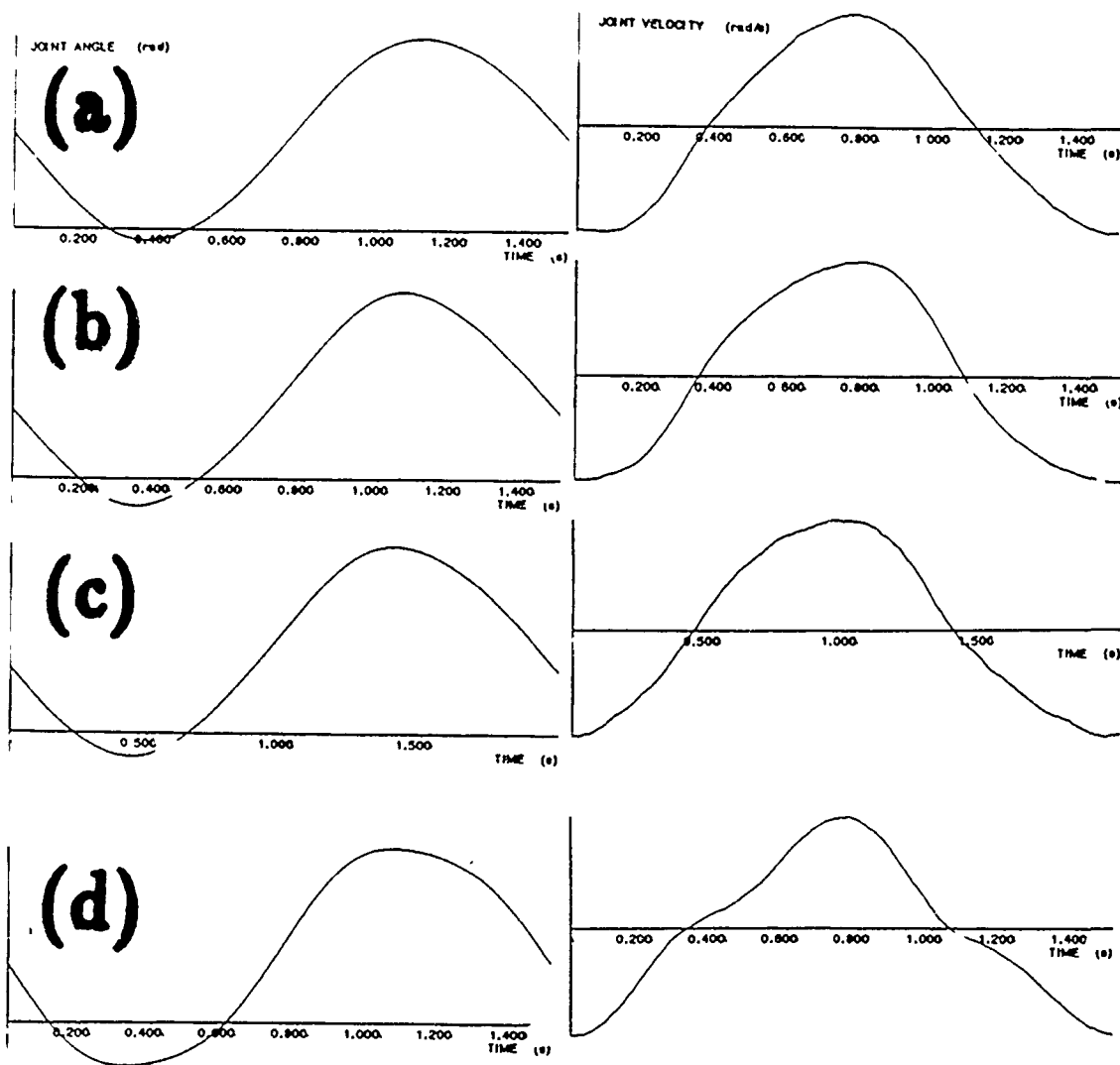
Figure 11-2: Mean trajectories (position and velocities) for subject S1 during the (a) horizontal 750 ms movements, (b) vertical 750 ms movements, (c) vertical 1000 ms movements, and (d) horizontal 750 ms movements with a damping load. All amplitudes are normalized. For reference, the 1000 ms and 750 ms peak velocities are respectively 1.6 rad/s and 2.0 rad/s, and the peak to peak displacement are approximately 1 rad (see previous figures).

is on average only a factor of 1.18 larger, and the mean stiffness across the movement is on average only a factor of 1.05 larger. These stiffness changes are significantly different from the predicted factor of 1.78. Thus, prediction (**P2**) is incorrect and a feedforward speed compensation is necessary.

The dynamic feedforward compensation is not complete though. As predicted in (**P4**) the trajectories loaded with a 1 $Nm/rad/s$ damper are different from the trajectories in all other conditions. Figure 11-2 shows this difference and also shows the similarity between the trajectories of all other conditions (gravity and speed). Particularly notice how different the velocity profile is for the damping loaded movement. It is perhaps not surprising that the arm does not maintain the same trajectory, as the task only requires reaching the targets.

Finally, as stiffness and viscosity do not scale up appropriately with speed, the possibility that the feedforward compensation is simplified by dynamic scaling is disproved. That is, prediction (**P5**) is incorrect. The stiffness and damping are *not* scaled so as to allow simple scaling of the feedforward torque command to produce faster movements.

11.2.4   Static Feedforward Gravity Compensation

Though the feedforward compensation is not merely static, it is still possible that gravity compensation occurs, giving the prediction (**P3**). Comparing the vertical movements to the horizontal movements (e.g., Figures 11-2, 10-15 and 10-11) it is found that there is little difference in either of the trajectories and the only difference in the dynamics is a less than 5 Nm/rad mean stiffness increase. Thus, unless this stiffness difference is significant, it is probable that gravity compensation is being used.

To further investigate the affect of these stiffness differences between the vertical and horizontal movements consider the arm to be driven by a linearized model of the form (7.15). In the absence of gravity compensation the computed desired trajectory θ_0 is shown in Figure 11-3(a). This was computed from (7.15) using the average actual trajectory, the estimated parameters, and a cylinder model of the arm (to estimate

the mass and center of mass from the inertia). This is the trajectory that the the equilibrium trajectory hypothesis [136][28] predicts. With gravity compensation the effect of the last term in (7.15) is zeroed, and the computed desired trajectory is shown in Figure 11-3(b). Notice that without gravity compensation the desired trajectory must take on a complex shape. Of course, these plots must be treated with care because they presume linearity of the arm dynamics, or at least that the identified parameters approximate the non-linear dynamics adequately (see Section 7.4). In any event, it appears that feedforward gravity compensation is required. That is, the stiffness increase in the vertical movements is not enough to compensate for gravity without explicitly providing a feedforward term to cancel out the static effect of gravity.

11.3   Mechanisms for Stiffness Modulation

As mentioned before, the perturbation stiffness measurements are a function of passive joint properties, muscle, and reflexes. Though it is difficult to distinguish these factors there are certain muscle properties that may well aid in explaining the *changes* in stiffness with velocity.

11.3.1   Intrinsic Velocity Dependent Compliance

Consider the repeated horizontal movements studied here. In this task the arm executes roughly a sinusoidal 0.5–0.7 Hz trajectory by exerting reciprocal biceps and triceps activity. A given muscle, when activated, can be considered to be driven by a sinusoidal position drive (i.e., the drive resulting from arm inertia and the other muscles). Thus, the isolated whole muscle oscillation studies of Rack and Westbury [105] are relevant to the present study. They oscillated tetanized cat soleus muscle at 0.9 Hz, and plotted the instantaneous length versus tension curves for complete cycles of the inr ·· sinusoid (the cycles were non-conservative: encircling a non-zero area in the length-tension plane, requiring work). Starting from zero velocity, the initial stretching of the muscle produces a sharp increase in tension until the stretch
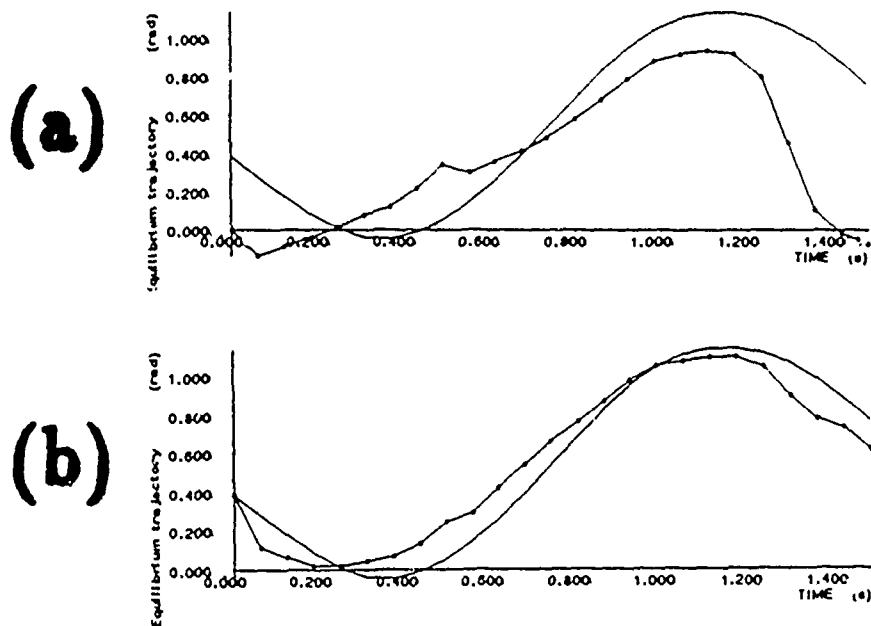
Figure 11-3: (a) Actual trajectory (solid line) and desired trajectory computed under the equilibrium trajectory hypothesis (dotted line). (b) Same as in (a) but gravity compensation is assumed in addition to the equilibrium trajectory hypothesis. Data shown are for subject S2. Desired trajectories were computed with equation (7.15) as described in the text.

exceeds 1 *mm*, and then the muscle continues to stretch with little increase in tension. On the reverse part of the cycle exactly the same thing happens: starting from zero velocity, the initial shortening produces a symmetrical sharp drop in tension until the shortening exceeds 1 *mm*, and then the muscle shortens with little decrease in tension. In effect, the muscle has a short range high stiffness acting only when starting from zero velocity, and only lasting for 1 *mm* stretches (5 percent of muscle length, or 4^0 of ankle rotation [122]). In the rest of the cycle (that is, during movement) the muscle is very compliant, resisting length changes with little force.

This phenomena was also observed in their earlier studies [121][122][123]. Figure 7-8 (the solid lines) shows their results for ramp stretches starting from various lengths and tensions. The ramp inputs cause an initial sharp rise in tension, which lasts only for about 1 *mm* (4^0 of ankle rotation). The tension then only rises slowly, or in some cases drops off, as the lengthening continues.

It can thus be speculated that the airjet perturbations are met with high short range stiffness only when the arm is near rest, that is, within a few degrees ($\approx \pm 4^0$) of the target. This short range stiffness is only probed by segments of the PRBS that switch fast enough to maintain the arm displacements within a few degrees. The low frequency segments of the PRBS perturb the arm outside of this short range stiffness zone, and would thus tend to lower the stiffness estimates.

Further, it may be speculated that during movement the airjet PRBS induced displacements should meet with much more muscle compliance than when at rest. That is, the tension from shortening active agonist muscles should drop relatively little in response to the displacements in the direction of movement (i.e., additional small displacements in the direction of the already shortening agonist should affect the muscle force similarly to the plots in [121][122][123]). Likewise, the tension in the lengthening antagonist muscles should rise relatively little in response to perturbation displacements in the direction of movement. Figure 7-8 indicates that it might even be possible for the tension to drop (for a lengthening muscle just beginning to move) in response to stretch. The muscle responses to PRBS induced displacements in the opposite direction to movement are probably similar if the displacements are small

enough not to reverse the direction of movement.

Lanman [130] (see review in Chapter 8) probed the human arm with high frequency sinusoidal perturbations during movement, and also found that the muscle stiffness drops during movement (the frequencies he used are too high to allow reflex activity). He attempted to link these results to a molecular level description of muscle, arguing that perhaps for displacements above a certain threshold the actin-myosin bond breaking rate is increased in proportion to the velocity. Thus, as the velocity increases the number of bonds should decrease, and the stiffness provided by the sum of all bonds should decrease.

Lanman also demonstrated that if the arm is loaded with a viscous damper during movement, then the stiffness no longer dropped. He likewise explained this result with a crossbridge model. He argued that the increased load requires more crossbridges to be formed, offsetting the effect of the crossbridges being broken by the muscle length changing. Lanman's result (and explanation) is hard to reconcile with the experiments of [105][122] described above, but is probably related to the fact that he only probed the arm with single high frequency (15-30 Hz) sinusoids. Also, as mentioned in Chapter 7 the distributed sarcomere force generation mechanisms are not generalized easily to whole muscle.

Generalizing Lanman's explanation to explain the data collected with PRBS perturbations with significant low frequency content must proceed with caution. As mentioned at the beginning of this chapter, below 5 Hz the airjet produces perturbation length changes beyond the short range stiffness of muscle (e.g., short range stiffness is attributed to the elastic limit of crossbridges in [130]). Although the measured stiffnesses do tend to drop with velocity, they do not increase much with a damping load. Thus, there must be other mechanisms than short range stiffness that maintain the stiffness profiles across these experimental conditions.

In summary, known muscle properties could qualitatively account for some of the features of the data collected in this thesis. Muscle can be viewed to have long time constant (> 50 ms) elastic properties (re length-tension curves) if allowed to come to rest (see review of muscle properties in Chapt. ~` Further, at rest muscle can

provide pure high stiffness if not stretched beyond the limit of its short range stiffness (e.g., elastic limit of the crossbridges). Both of these stiffnesses contribute to the measured stiffness near the targets. Also, as more force is required in the vicinity of the target (e.g., due to acceleration gravity changes) more parallel force generating elements have to be recruited (either by increased firing frequency or increased muscle fiber recruitment), and thus the stiffness should go up. On the other hand, during movement muscle behaves more like a pure force source with only damping, (that is, not necessarily resisting length changes to external force perturbations). Thus, even though there may still be force being generated during the movement (e.g., to oppose the external damping load in the experiments) the stiffness should still drop. Of course, these are rough characterizations of the true complex behavior of muscle. Many of the finer details in the data are still hard to understand. For example, why do the stiffness changes slightly lead the muscle force changes (rising before the target is reached, that is, before peak acceleration)? This brings us to a consideration of the influence of reflexes.

11.3.2   Reflex Contribution to Stiffness

As the measured stiffnesses are low (giving natural frequencies below 3 Hz), it is possible that they are maintained by reflexes — in spite of feedback delays. That is, muscle forces during movement may be driven by reflexes to augment the effective mechanical stiffness of the arm (see Section 7.3).

The contribution of reflexes can be assessed by measuring EMG activity (also see Section 7.6). An estimation of the transfer function between EMG and perturbation torques gives an indication of the reflex onset and magnitude. Fortunately, Soechting et al. [143] have measured such reflex transfer functions during ballistic forearm movements when applying PRBS force inputs with exactly the same frequency content as in this thesis (see Review Section 8.2). Their time-varying reflex impulse responses indicate that the reflex activity due to the perturbations is significant throughout the movement, with initial magnitudes and onset times similar to those of the same responses measured while maintaining a fixed posture. The movement reflex responses

differ from the posture reflex responses in that they have significant activity at lags of up to 300 ms, indicating that proprioceptive information from as much as 300 ms in the past is used to control the movement — even information from before the onset of movement is used (re feedforward control). The reflex onset delays are of about 50 ms, implying that the reflex loop gain can be significantly above unity for frequencies below 10 Hz (above 10 Hz the reflex gains must be below unity to ensure stability, see Section 1.1.1). Thus, it is possible that the reflexes can contribute to maintaining the stiffness values (<3 Hz natural frequency) measured in this thesis.

11.4 Summary

The contribution of this work has been to provide estimates of the time-varying mechanical compliance of the arm during movement. The arm stiffness is modulated with the movement, dropping relatively low during motion. Such control of the mechanical compliance could be advantageous from the standpoint of avoiding excessive contact forces in unexpected collisions, or more generally for producing constrained motions (see remarks in Chapter 12).

The finding that the stiffness is low during movement is not inconsistent with an equilibrium trajectory hypothesis (i.e., static feedforward compensation). Simulations using the estimated stiffnesses show that, provided gravity is compensated for, the equilibrium trajectories reflect the actual trajectories closely (see Figure 7.15(b)). The reason for this is that, in spite of the equilibrium potential field being negligible during movement, the inertia of the arm continues the motion.

The additional finding that dynamic scaling does not occur to compensate for a movement speed increase is inconsistent with the equilibrium trajectory hypothesis. McIntyre [162] anticipated this discrepancy, but argues that augmenting the equilibrium trajectory theory with a velocity referenced reflex feedback loop (including reasonable physiological delays) is sufficient to produce similar time scaled movements at different speeds. This solution preserves the simplicity of the theory, and properly stresses the importance of velocity sensory information in the motor system (see

Section 6.2.1).

Chapter 12

Future Research

12.1 Kinematic Calibration

12.1.1 Use of Force and Velocity Sensing

In contrast to joint angle measurements, joint torque measurements enter linearly into the relation describing the endpoint force. Thus, kinematic calibration may be simplified by using force sensing. Specifically, it is possible to estimate the linearly occurring elements of the joint Jacobian matrix relating tip forces to joint torques. The kinematic parameters can then be analytically recovered from the Jacobian matrix elements. This analytic parameter estimation is possible because of the simple structure of the Jacobian matrix derived in Chapter 3. Similarly, as the joint angle Jacobian also relates joint velocities to endpoint velocities, it should likewise be possible to analytically estimate the kinematic parameters from velocity information.

While analytic techniques may not give accurate parameter estimates when noise is present, they are important to develop, as a major difficulty in kinematic calibration is the estimation of initial parameter estimates.

Finally, the use of velocity and force information in calibration is attractive from a biological point of view, as these quantities appear more readily available in the human motor system (re Chapter 6).

12.1.2 Global Uniqueness

In Chapter 3 results pertaining to the uniqueness of the kinematic parameters were derived. It was shown that there are multiple solutions to the non-linear calibration equations, and that the equations become singular for certain parameter sets. As calibration must proceed iteratively, the following question should be addressed in the future. Is it possible to follow a continuous path in parameter space (by any iterative algorithm) from any initial point to a solution without crossing a singularity? It is reasonable to conjecture that the answer to this question is yes. At least for calibrating open kinematic chains, it is possible to show that the singularities divide up the parameter space into disjoint manifolds, each of which contains one of the 2^{n-1} solutions (provided the length parameters are suitably bounded). There may be additional solutions on each manifold, but there can only be a finite number of them. The manifolds provide a multiple covering of the output (endpoint) space. Thus, in the open-loop calibration case a solution can always be reached without crossing a singularity (i.e., without leaving a manifold). This needs to be elaborated and the full conjecture should be tested.

12.1.3 Motor Psychophysics

The relevance of model-based robotics control methods to human motor control requires further psychophysical experimentation. For example, experiments similar to the teleoperator adaption experiments described in Chapter 6 may help develop an understanding of how constrained our internal representations of sensorimotor transformations are. As well, simple experiments to characterize the accuracy of whole arm 3-dimensional movement are necessary, before any strong conclusions can be drawn about how important calibration is to the motor system.

12.2 Airjet Experiments

12.2.1 Compliance During Performance of Difficult Tasks

Future airjet experiments should include characterizing the forearm's compliance while performing more interesting tasks — such as catching a ball. The role of compliance in these tasks is more critical, and an understanding of how it is modulated may aid in building robots that can perform similar complex tasks.

12.2.2 Role of Reflexes

As mentioned in Chapter 7 the role of reflexes can be studied by estimating models with sufficiently time lagged parameters — to account for delays. This can be done with the existing data. Alternatively, time-varying impulse responses can be estimated. As discussed in Chapter 9, this requires the development of an identification technique that incorporates a smoothness constraint on the impulse response. Finally, future experiments will record EMG during movement, and EMG-torque impulse responses will be identified.

12.2.3 Whole Arm Compliance

The main goal of the airjet project was (and still is) to characterize the 3-dimensional compliance of the arm during unconstrained movement. Generalization of the airjet perturbation device to a 3-dimensional version should be straight forward. Three-dimensional system identification techniques must also be developed.

12.3 Role of Compliance in Constrained Arm Movements

In previous work, not reported in this thesis, we performed a series of experiments to study the contact forces during constrained whole arm movement [163]. We found that a hypothesized strategy of relying on the compliance of the arm and ignoring

the specific surface constraint shape was consistent with experimental measurements. This work will be continued and integrated with the compliance estimation studies reported in this thesis.

Appendix

The damper torque load used in the airjet experiments has a torque-velocity characteristic given by Figure 12-1. In all cases the damper was set at 75 percent of maximum damping.
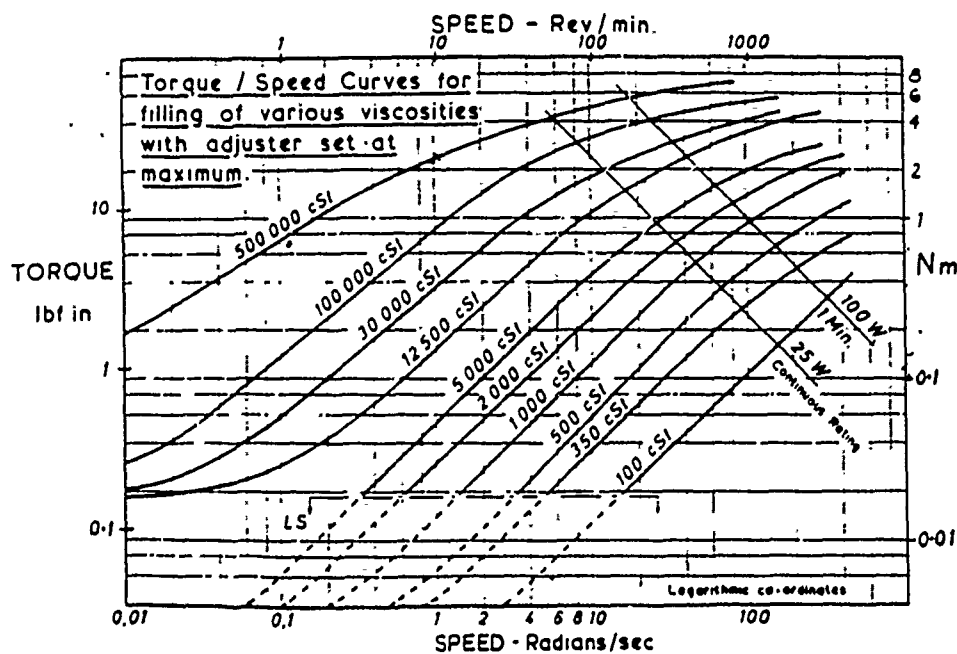

Figure 12-1: Torque-velocity relation for the damper used to load the arm. The model used has the 500,000 *cSt* filling. At all times the viscosity was set at 75 percent of the maximum adjustable value. Damper manufactured by Kinetrol.

References

1. Hollerbach, J.M., June, 1982, "Computers, brains and the control of movement," *Trends in Neurosciences*, 5 no. 6, pp. 189-204.

2. Hildreth, E.C., and Hollerbach, J.M., 1987, "Artificial intelligence: computational approach to vision and motor control," *Handbook of Physiology, Section 1: The Nervous System, Volume V: Higher Functions of the Brain, Part II*, edited by F. Plum, Bethesda, Maryland, American Physiological Society, pp. 605-642.

3. Hollerbach, J.M., 1990, "Fundamentals of motor behavior," *An Invitation to Cognitive Science, Visual Cognition and Action, Vol. 2*, Cambridge, MA, MIT Press, pp. 151-182.

4. Loeb, G.E., 1984, "The control and responses of mammalian muscle spindles during normally executed motor tasks," *Exercise and Sport Sciences Reviews*, edited by Terjung, R.L., Lexington, MA, Collamore Press, pp. 157-204.

5. Sheridan, T.B., and Ferrell, W.R., 1974, *Man-Machine Systems: Information. Control, and Decision Models of Human Performance*, Cambridge, MA, MIT Press.

6. Novas, M.F., 1963, Sampling or Quantization in Human Tracking Systems, S.M. Thesis, MIT, M.E..

7. Bekey, G.A., 1962, "The human operator as a sampled data system," *IRE Trans. Human Factors in Electronics*, HFE-3, pp. 43-51.

8. Crossman, E.R.F.W, and Goodeve, P.J., 1983 (1963), "Feedback control of hand-movement and Fitts' law," *Quarterly J. Expt. Psych.*, 35A, pp. 251-278.

9. Carlton, L.G., 1981, "Processing of visual feedback information for movement control," *J. Expt. Psych.: Percep. and Perfom.* , 7 no. 5, pp. 1019-1030.

10. Desoer, C. A., and Vidyasagar, M., 1975, *Feedback Systems: Input-Output Properties*, New York, Academic Press.

11. Colgate, J.E., 1988, The Control of Dynamically Interacting Systems, Ph.D. Thesis, MIT, Dept. Mechanical Eng., August.

12. Joyce, G.C., and Rack, P.M.H., 1974, "The forces generated at the human elbow joint in response to imposed sinusoidal movements of the forearm," *J. Physiol*, 240, pp. 351-374.

13. Joyce, G.C., and Rack, P.M.H., 1974, "The effects of load and force on tremor at the normal human elbow joint," *J. Physiol*, 240, pp. 375-396.

14. Albus, J.S., 1975, "A new approach to manipulator control: the cerebellar model articulation controller (CMAC)," *J. Dynamic Syst., Meas., and Control*, 97, pp. 220-233.

15. Raibert, M.H., 1978, "A model for sensorimotor control and learning," *Biol. Cybernetics*, 29, pp. 29-36.

16. An, C.H., Atkeson, C.G., and Hollerbach, J. M., 1988, *Model-based Control of a Robot Manipulator*, Cambridge, MIT Press.

17. Atkeson, C.G., and Reinkensmeyer, D.J., 1989, "Using associative content-addressable memories to control robots," *Proc. IEEE Int. Conf. Robotics and Automation*, Scottsdale, Arizona, May 14-19, pp. 1859-1864.

18. Astrom, K.J., and Wittenmark, B., 1989, *Adaptive Control*, Reading, MA, Addison-Wesley Publishing Co..

19. Robinson, D.A., Sept. 1976, "Adaptive gain control of vestibular reflex by the cerebellum," *J. of Neurophysiology*, 38 no. 5, pp. 954-969.

20. Galiana, H.L., 1990, "Oculomotor control," *An Invitation to Cognitive Science, Visual Cognition and Action, Vol. 2*, Cambridge, MA, MIT Press, pp. 243-316.

21. Hollerbach, J.M., and Flash, T., 1982, "Dynamics interactions between limb segments during planar arm movement," *Biol. Cybern.*, 44, pp. 67-77.

22. McGeer, T., 1990, "Passive dynamic walking," *Int. J. Robotics Research*, 9 no. 2, pp. 62-82.

23. Hollerbach, J.M., 1985, "Optimum kinematic design for a seven degree of freedom manipulator," *Robotics Research: The Second International Symposium*, Cambridge, MA, pp. 215-222.

24. Mason, M.J., and Salisbury, J.K., 1985, *Robot Hands and the Mechanics of Manipulation*, Cambridge, MA, MIT Press.

25. Raibert, M.H., 1986, *Legged Robots that Balance*, Cambridge, MA, MIT Press.

26. Feldman, A.G., 1986, "Once more on the equilibrium-point hypothesis (λ model) for motor control," *J. Motor Behav.*, 18 no. 1, pp. 17-54.

27. Bizzi, E., and Abend, W.K., 1985, "Control of multijoint movement," *Comparative Neurobiology: Modes of Communication in the Nervous System*, edited by Strumwasser, F., and Cohen, M., New York, Wiley and Sons, pp. 255-277.

28. Hogan, N., 1988, "Planning and execution of multijoint movements," *Can. J. Physiol. and Pharm.*, 66 no. 4, pp. 508-517.

29. Held, R., Nov. 1965, "Plasticity in sensory-motor systems," *Sci. American*, pp. 84-94.

30. Shamma, J.S., and Whitney, D.E., 1987, "A method of inveres robot calibration," *ASME J. Dynamic Systems, Meas., Control*, 109, pp. 36-43.

31. Abdel-Aziz, Y. I., and Karara, H. M., 1971, "Direct linear transformation into object space coordinates in close-range photogrammetry," *Symposium on Close-Range Photogrammetry*, University of Illinois at Urbana-Champaign, Urbana, Il, January 26-29, pp. 1-18.

32. Bernstein, N., 1967, *The Co-ordination and Regulation of Movements*, Oxford, Permagon Press.

33. Hollerbach, J.M. and Bennett, D.J., 1988, "Automatic kinematic calibration using a motion tracking system," *Robotics Research: The Fourth International Symposium*, edited by R. Boiles and B. Roth, Cambridge, Mass., MIT Press, pp. 191-198.

34. Hollerbach, J.M., 1989, "A review of kinematic calibration," *The Robotics Review 1*, edited by O. Khatib, J.J. Craig, and T. Lozano-Perez, Cambridge, MA, MIT Press, pp. 207-242.

35. Hartenberg, R.S. and Denavit, J., 1964, *Kinematic Synthesis of Linkages*, New York NY, McGraw-Hill Book Co..

36. Lee, H. and Liang, C., 1988, "Displacement analysis of the general spatial 7-link 7R mechanism," *Mech. Mach. Theory*, 23, pp. 219-226.

37. Bennett, D.J., and Hollerbach, J.M., 1988, "Self-calibration of single-loop, closed kinematic chains formed by dual or redundant manipulators," *Proc. 27th IEEE Conf. Decision and Control*, Austin, Texas, Dec. 7-9.

38. Bennett, D.J., and Hollerbach, J.M., 1989, "Identifying the kinematics of robots and their tasks," *Proc. IEEE Int. Conf. Robotics and Automation*, Scottsdale, Arizona, May 14 - 19.

39. Bennett, D.J., and Hollerbach, J.M., 1989, "Identifying the kinematics of non-redundant serial chain manipulators by a closed-loop approach," *Proc. Fourth International Conference on Advanced Robotics*, Columbus, Ohio, June 13-15, in press.

40. Denavit, J. and Hartenberg, R.S., 1955, "A kinematic notation for lower pair mechanisms based on matrices," *J. Applied Mechanics*, 22, pp. 215-221.

41. Roth, B., 1984, "Screws, motors, and wrenches that cannot be bought in a hardware store," *Robotics Research: The First International Symposium*, edited by Brady, M., and Paul, R., Cambridge, Mass., MIT Press, pp. 679-693.

42. Sugimoto, K. and Okada, T., 1985, "Compensation of positioning errors caused by geometric deviations in robot system," *Robotics Research: The Second International Symposium*, edited by H. Hanafusa and H. Inoue, Cambridge, Mass., MIT Press, pp. 231-236.

43. Whitney, D.E., 1972, "The mathematics of coordinated control of prosthetic arms and manipulators," *J. Dynamic Systems, Meas., Control*, pp. 303-309.

44. Guilleman, V. and Pollack, A., 1974, *Differential Topology*, Englewood Cliff., NJ, Prentice Hall, Inc..

45. Spivak, M., 1965, *Calculus on Manifolds*, New York, W. A. Benjamin, Inc..

46. Hayati, S.A., 1983, "Robot arm geometric link parameter estimation," *Proc. 22nd IEEE Conf. Decision and Control*, San Antonio, Dec. 14-16, pp. 1477-1483.

47. Armstrong, B., 1987, "On finding 'exciting' trajectories for identification involving systems with non-linear dynamics," *Proc. IEEE Intl. Conf. Robotics and Automation*, Raleigh, NC, Mar. 31-Apr. 3, pp. 1131-39.

48. Sinha, N. K., and Kuszta, B., 1983, *Modeling and Identification of Dynamic Systems*, New York, NY, Van Nostrand Reinhold Co..

49. Nakamura, Y. and Hanafusa, H., 1986, "Inverse kinematic solutions with singularity robustness for robot manipulator control," *J. Dynamic Sys., Meas., Contr.*, 108, pp. 163-171.

50. Norton, J.P., 1986, *An Introduction to Identification*, Orlando, Florida, Academic Press.

51. Strang, G., 1980, *Linear Algebra and Its Applications*, New York, Academic Press.

52. Burdick, J.W., March 1988, *Kinematic analysis and design of redundant manipulators*, Stanford University, Ph.D. Thesis.

53. Whitney, D.E., Lozinski, C.A., and Rourke, J.M., 1986, "Industrial robot forward calibration method and results," *J. Dynamic Systems, Meas., Control*, 108, pp. 1-8.

54. Bennett, D.J., and Hollerbach, J.M., 1989, "Closed-loop kinematic calibration of the Utah-MIT Hand," *1st Intl. Symp. Experimental Robotics*, Montreal, June 19-21, in press.

55. Bennett, D.J., Hollerbach, J.M. and Geiger, D., 1989, "Autonomous robot calibration for hand-eye coordination," *Preprints 5th Intl. Symp. Robotics Research*, Tokyo, Aug. 28-31, pp. 148-155.

56. Jacobsen, S.C., Iversen, E.K., Knutti, D.F., Johnson, R.T., and Biggers, K.B., 1986, "Design of the Utah-MIT Dextrous Hand," *Proc. IEEE Int. Conf. Robotics and Automation*, San Francisco, April 7-10, pp. 1017-1023.

57. Narasimham, S., 1988, *Dextrous Robotic Hands: Kinematics and Control*, M.I.T., Masters Thesis.

58. Press, W.P., Flannery, B.P., Teukolsky, S.A., and Vettering, W.T., 1988, *Numerical Recipes in C*, New York, Cambridge University Press.

59 Niemeyer, G., and Slotine, J-J. E., 1988, "Performance in adaptive manipulator control," *Proc. 27th IEEE Conf. Decision and Control*, Austin, Texas, Dec. 7-9, pp. 1585-1591.

60. Tsai, R.Y., 1989, "Synopsis of recent progress on camera calibration for 3D machine vision," *Robotics Review 19??*, edited by O. Khatib, J.J. Craig, and T. Lozano-Perez, Cambridge, MA, MIT Press.

61. Martins, H. A., Birk, J. R., and Kelley, R. B., 1981, "Camera models based on data from two calibrated planes," *Computer Graphics and Image Processing*, 17, pp. 173-180.

62. Gremban, K. D., Thorpe, C. E., and Kanade, T., 1988, "Geometric camera calibration using systems of linear equations," *Proc. IEEE Int. Conf. Robotics and Automation*, Philadelphia, Penn, April 24-29, pp. 562-567.

63. Sobel, I., 1974, "On calibrating computer controlled cameras for perceiving 3-D scenes," *Artificial Intelligence*, 5, pp. 185-198.

64. Yakimovsky, Y., and Cunningham, R., 1978, "A system for extracting three dimensional measurements from a stereo pair of TV cameras," *Computer Graphics and Image Processing*, 7, pp. 195-210.

65. Duda, R. O., and Hart, P. E., 1973, *Pattern Recognition and Scene Analysis*, New York, Wiley.

66. Horn, B.K.P., 1986, *Robot Vision*, Cambridge, MA, MIT Press.

67. Moffitt, F., and Mikhail, E., 1980, *Photogrammetry*, New York, NY, Harper and Row.

68. Ziemann, H., 1985, "A mathematical model for camera calibration," *Technical Papers, 51st Annual American Society of Photogrammetry Meeting*, Washington, D.C., March 10-15, pp. 725-735.

69. Tsai, R. Y., 1986, "An efficient and accurate camera calibration technique for 3-D machine vision," *Proc. IEEE Conference on Computer Vision and Pattern Recognition*, Miami, FL, pp. 364-374.

70. Ganapathy, S., 1984, "Decomposition of transformation matrices for robot vision," *Proc. IEEE Int. Conf. Robotics and Automation*, pp. 130-139.

71. Isaguirre, A, Pu, P., and Summers, J., 1985, "A new development in camera calibration: calibration of a pair of mobile cameras," *IEEE Int. Conf. Robotics and Automation*, St. Louis, March 25-28, pp. 74-79.

72. Kenefick, J.F., Gyer, M.S., and Harp B.F., 1972, "Analytic self-calibration," *Photogrammetric Engineering*, 38, pp. 1117 - 26.

73. Brooks, R. A., Flynn, A. M., and Marill, T., 1988, "Self calibration of motion and stereo for mobile robots," *Robotics Research: The Fourth International Symposium*, edited by Bolles. R, and Roth, B., Cambridge, Mass., MIT Press, pp. 277-286.

74. Puskorius, G.V., and Feldkamp, L.A., 1987, "Global calibration of a robot/vision system," *Proc. IEEE Int. Conf. Robotics and Automation*, Raleigh, NC, March 31-April 3, pp. 190-195.

75. Haralick, R. M., 1980, "Using perspective transformations in scene analysis," *Computer Graphics and Image Processing*, 13, pp. 191-221.

76. Torre, V., Verri, A., and Fiumicelli, A., 1986, "Stereo accuracy for robotics," *Robotics Research: The Third International Symposium*, edited by Faugeras, O., and Giralt, G., Cambridge, Mass., MIT Press, pp. 5-10.

77. Descartes, R., 1985, "Optics," *The Philosophical Writings of Descartes, Vol. 1*, edited by J. Cottingham et al., New York, NY, Cambridge Univ. Press.

78. Woodworth R.S., July, 1899, "The accuracy of voluntary movement," *Psychological Review: Series of Monograph Supplements*, Suppl 3 no. 3, .

79. Fitts, P.M., 1947, "A study of location discrimination ability," *Psych. Research in Equipment Design*, edited by Fitts, P.M., Washington, DC, pp. 207-217.

80. Georgopoulos, A.P., 1986, "On Reaching," *Ann. Rev. Neurosci.*, 9, pp. 147-170.

81. Biguer, B., Prablanc, C., and Jeanerod, M., 1984, "The contribution of coordinated eye and head movements in hand pointing accuracy," *Exp. Brain Res.*, 55, pp. 462-469.

82. Loomis, J.M., and Lederman, S.J., 1986, "Tactile Perception," *Handbook of Perception and Human Performance, vol1*, edited by K.R. Boff, L. Kaufman, J.P. Thomas, New York, Wiley and Sons.

83. Clark, F.J. and Horch, K.W., 1986, "Kinesthesia," *Handbook of Perception and Human Performance, vol1*, edited by K.R. Boff, L. Kaufman, J.P. Thomas, New York, Wiley and Sons.

84. Tardy-Gervet, M., Gilhodees, J., and Roll, J., 1989, "Induction of illusory limb movement as a means of studying sensorimotor interactions in the eye-arm system," *Brain Behav. Evol.*, 33, pp. 165-170.

85. Howard, I.P., and Templeton, W.B., 1966, *Human spatial orientation*, New York, Wiley and Sons.

86. Howard, I.P., 1973, "Orientation and motion in space: Chapter 14," *Handbook of Perception, vol. 3*, edited by Carterette, E.C and Friedman, M.P., pp. 291-313.

87. Wallace, B., and Redding, G.M., 1979, "Additivity in prism adaption as manifested in intermanual and interocular transfer," *Perception and Psychophysics*, 25 no. 2, pp. 133-136.

88. Redding, G.M., and Wallace, B., 1988, "Components of prism adaption in terminal and concurrent exposure: organization of the hand-eye coordination loop," *Perception and Psychophysics*, 44 no. 1, pp. 59-68.

89. Bedford, F.L., 1989, "Constraints on learning new mappings between perceptual dimensions," *J. Expt. Psych.: Percep. and Perfom.*, 15 no. 2, pp. 232-248.

90. Vertut, J., 1977, "Control of master slave manipulators and force feedback," *Joint Automatic Control Conf.*, pp. 172-184.

91. Bejczy, A.K., June 1980, "Sensors, controls, and man-machine interface for advanced teleoperation," *Science*, 208 no. 4450, pp. 1327-1335.

92. Goertz, R.C., 1963, *Human Factors in Technology*, edited by E.M. Bennett, New York, McGraw-Hill.

93. Brooks, T.L., 1979, Superman: A System for Supervisory Manipulation and the Study of Human/Computer Interactions, M.S. Thesis, MIT, M.E..

94. Shepard, R.N., and Cooper, L.A., 1982, *Mental Images and their Transformations*, Cambridge, MA, MIT Press.

95. Lozano-Perez, T., 1983, "Spatial planning: a configuration space approach," *IEEE Trans. Comp.*, C-32, pp. 108-120.

96. Parsons, L.M., 1987, "Imagined spatial transformations of one's hands and feet," *Cognitive Psychology*, 19, pp. 178-241.

97. Parsons, L.M. and Shimojo, S., 1987, "Perceived spatial organization of cutaneous patterns on the surfaces of the human body in various positions," *J. Expt. Psych.: Percep. and Perfom.* , 13 no. 3, pp. 488-504.

98. Wallach, H., and O'Connell, D.N., "The kinetic depth effect," *J. of Expt. Psych.*, 45 no. 4, pp. 205-17.

99. Ullman, S., May 1977, The Interpretation of Visual Motion, Ph.D. Thesis, MIT, E.E..

100. Georgopoulos, A.P., 1988, "Spatial coding of visually guided arm movements in the primate cortex," *Can. J. Physiol. and Pharm.*, 66 no. 4, pp. 518-526.

101. Kalaska J.F., 1988, "The representation of arm movements in the postcentral and parietal cortex," *Can. J. Physiol. and Pharm.*, 66 no. 4, pp. 455-463.

102. Ebenholtz, S.M., and Fisher, S.K., 1982, "Distance adaption depends upon plasticity in the oculomotor control system," *Perception and Psychophysics* , 31 no. 6, pp. 551-560.

194

103. Bizzi, E., Dev, P., Morasso, P., and Polit, A., May 1978, "Effects of load disturbances during centrally initiated movements," *J. of Neurophysiology*, 41 no. 3, pp. 542-556.

104. Pringle, J.W.S., 1967, "The contractile mechanism of insect fibrillar muscle," *Prog. Biophys. & Mol. Bio.*, 17, pp. 1-60.

105. Rack, P.M.H., and Westbury, D.R., 1974, "The short range stiffness of active mammalian muscle and its effect on mechanical properties," *J. Physiol*, 240, pp. 331-350.

106. Zames, G., 1961, "Nonlinear Operators for System Analysis," *MIT Res. Lab of Electronics*, Tech. Rept. 370,.

107. Atkeson, C.G., and Hollerbach, J.M., 198?, "Kinematics features of unrestrained vertical arm movements," *J. Neuroscience*, 5, pp. 2318-2330.

108. Bennett, D.J, and Hollerbach, J.M., 1987, "Joint velocity profiles during vertical arm motion," *Society for Neuroscience Conference Abstracts*, pp. 714.

109. Ghez, C., and Martin, J.H., 1982, "The control of rapid limb movement in the cat III. Agonist-antagonist coupling," *Exp. Brain Res.*, 45, pp. 115-125.

110. Desmedt, J.E., and Godaux, E., 1978, "Ballistic skilled movements: load compensation and pattering of motor commands," *Prog. Clin. Neurophysiology*, 4, pp. 21-55.

111. Nichols, T.R., and Houk, J.C., 1976, "Improvement in linearity and regulation of stiffness that results from actions of the stretch reflex," *J. Neurophys.*, 39, pp. 119-142.

112. Capaday, C., and Stein, R.B., 1987, "Difference in the amplitude of the human soleus H reflex during walking and running," *J. Physiol.*, 392, pp. 513-522.

113. Hollerbach, J.M., 1984, "Dynamic scaling of manipulator trajectories," *J. Dyn. Syst., Measmnt., and Control*, 106, pp. 102-106.

114. Ruitenbeek, 1984, "Invariants in loaded goal directed movements," *Biol. Cybern,* 51, pp. 11-20.

115. Bennett, D.J, Xu, Y., Hollerbach, J.M., and Hunter, I.W., 1989, "Identifying the mechnical impedance of the elbow joint during posture and movement," *Society for Neuroscience Conference Abstracts,* Pheonix, Arizona, pp. 396.

116. Xu, Y., Bennett, D.J, Hollerbach, J.M., and Hunter, I.W., 1989, "Wrist-airjet system for identification of the joint mechanical properties of the unconstrained human arm," *Society for Neuroscience Conference Abstracts,* Pheonix, Arizona, pp. 396.

117. Huxley, A.F., 1957, "Muscle structure and theories of contraction," *Prog. Biophys. and Biophys. Chem.,* 7, pp. 255-318.

118. Ford, L.E., Huxley, A.F., and Simmons, R.M., 1977, "Tension responses to sudden length change in stimulated frog muscle fibers near slack length," *J. Physiol.,* 269, pp. 441-515.

119. McMahon, T.A., 1984, *Muscles, Reflexes, and Locomotion,* Princeton, NJ, Princeton University Press.

120. Gordon, A.M., Huxley, A.F., and Julian, F.J., 1966, "The variation in isometric tension with sarcomere length in vertebrate muscle fibers," *J. Physiol.,* 189, pp. 170-192.

121. Rack, P.M.H., and Westbury, D.R., 1969, "The effects of length and stimulus rate on the tension in the isolated cat soleus muscle," *J. Physiol.,* 204, pp. 443-460.

122. Joyce, G.C., Rack, P.M.H., and Westbury, D.R., 1969, "The mechanical properties of cat soleus muscle during controlled lengthening and shortening movements," *J. Physiol.,* 204, pp. 461-474.

123. Joyce, G.C., and Rack, P.M.H., 1969, "Isotonic lengthening and shortening movements of the cat soleus muscle," *J. Physiol.,* 204, pp. 475-491.

124. Hoffer, J.A., Caputi, A.A., Pose, I.E., and Griffiths, R.I., 1989, "Roles of muscle activity and load on the relationship between muscle spindle length and whole muscle length in the freely walking cat," *Progress in Brain Research*, 80, pp. 75-85.

125. Henneman, E., Somjen, G., and Carpenter, D.O., 1965, "Functional significance of the cell size in spinal motorneurons," *J. Neurophysiol.*, 28, pp. 560-580.

126. Windhorst, O., Hamm, T.M. and Stuart, D.G., 1989, "On the function of muscle and reflex partitioning," *Behavioral and Brain Sciences*, 12, pp. 625-681.

127. Houk, J.C, and Rymer, W.Z., 1981, "Neural control of muscle length and tension," *Handbook of Physiology – the Nervous System II*, pp. 257-321.

128. Hoffer, J.A., and Loeb, G.E., 1983, "A reversible fusimotor blockade during chronic recording from spindle afferents in walking cats," *Exp. Brain Res., Suppl.*, 7, pp. 272-279.

129. Hoffer, J.A., "Techniques to study spinal cord, periferal nerve and muscle activity in freely moving animals," *Neuromethods Series, Vol. 14: Neurophysiology*, edited by A.A. Boulton et al., Clifton, NJ, USA, Humana Press, in press.

130. Lanman, J.M., 1980, Movement and the Mechanical Properties of the Intact Human Elbow Joint, Ph.D. Thesis, MIT, Dept. Psychology.

131. Cannon, S.T., and Zahalak, G.I., 1982, "The mechanical behavior of active human skeletal muscle in small oscillations," *J. Biomechanics*, 15 no. 2, pp. 111-121.

132. Lacquaniti, F., Licata, F., and Soechting, J.F., 1982, "The mechanical behavior of the human forearm in response to transient perturbations," *Biol. Cybern.*, 44, pp. 35-46.

133. Bizzi, E., Polit, A., and Morasso, P., March 1976, "Mechanisms underlying achievement of final head position," *J. Neurophysiology*, 39 no. 2, pp. 435-444.

134. Polit, A., and Bizzi, E., January 1979, "Characteristics of motor programs underlying arm movements in monkeys," *J. Neurophysiology*, 42 no. 1, pp. 183-194.

135. Bizzi, E., Chapple, W., and Hogan, N., 1982, "Mechanical properties of muscles; implications for motor control," *TINS*, 5 no. 11, pp. 395-398.

136. Bizzi, E., Accornero, N., Chapple, W., and Hogan, N., 1984, "Postural control and trajectory formation during arm movement," *J. of Neuroscience*, 4 no. 11, pp. 2738-2744.

137. Agarwal, G.C., and Gottlieb, G.L., 1977, "Oscillation of the human ankle joint in response to applied sinusoidal torque on the foot," *J. Physiology*, 268, pp. 151-176.

138. Mussa-Ivaldi, F.A., Hogan, N., and Bizzi, E., 1985, "Neural, mechanical and geometric factors subserving arm posture in humans," *J. Neuroscience*, 5, pp. 2732-2743.

139. Sinkjaer, T., Toft, E., Andreassen, S., and Hornemann, B.C., "Muscle stiffness in the human ankle dorsiflexors: intrinsic and reflex components," *Ints. of Elect. Syst.*,.

140. Gottlieb, G.L., and Agarwal, G.C., 1978, "Dependence of human ankle compliance on joint angle," *J. Biomechanics*, 11, pp. 177-181.

141. Weiss, P.L., Hunter, I.W., and Kearney, R.E., 1988, "Human ankle joint stiffness over the full range of muscle activation levels," *J. Biomechanics*, 21 no. 7, pp. 539-544.

142. Yosef, V.A., and Inbar, G.F., March 1986, "Parameter estimation of the mechanical impedance of the forearm of the human-operator using Gaussian torque input," *EE PUB.*, 582,.

143. Soechting, J.F., Dufresne, J.R., and Lacquaniti, F., Dec. 1981, "Time-varying properties of the myotatic response in man during some simple motor tasks," *J. of Neurophysiol.*, 46 no. 6, pp. 1226-1243.

144. Dufresne, J.R., Soechting, J.F., and Terzuolo, C.A., 1978, "Electromyographic response to pseudo-random torque disturbances of human forarm position," *Neuroscience*, 3, pp. 1213-1226.

145. Soechting, J.F., and Lacquaniti, F., April 1988, "Quantitative evaluation of the electromyographic responses to multidirectional load perturbations of the human arm," *J. of Neurophysiol.*, 59 no. 4, pp. 1296-1313.

146. Hunter, I.W., and Kearney, R.E., 1982, "Dynamics of human ankle stiffness: variation with mean ankle torque," *J. Biomechanics*, 15, pp. 747-752.

147. Kearney, R.E., and Hunter, I.W., 1982, "Dynamics of human ankle stiffness: variation with displacement amplitude," *J. Biomechanics*, 15, pp. 753-756.

148. Weiss, P.L., Kearney, R.E., and Hunter, I.W., 1986, "Position dependence of ankle joint dynamics — I. Passive mechanics," *J. Biomechanics*, 19, pp. 727-736.

149. Weiss, P.L., Kearney, R.E., and Hunter, I.W., 1986, "Position dependence of ankle joint dynamics — II. Active mechanics," *J. Biomechanics*, 19, pp. 737-751.

150. Xu, Y., Hunter, I.W., Hollerbach, J.M., and Bennett, D.J,, "An airjet system for identification of the human arm joint mechanical properties," *IEEE Trans. Biomcd. Engrg.*, submitted.

151. Xu, Y., Bennett, D.J, Hollerbach, J.M., and Hunter, I.W., June 9-12, 1990, "A wrist-mounted airjet for studying human arm joint mechanical properties," *Canadian medical and Biomedical Engineering Society Conference*, Winnipeg, Canada, in press.

152. Colgate, J.E., 1986, The Design of a Dynamics Measuring Device, M.S. Thesis, MIT, Dept. Mechanical Eng., January.

153. Murray, W.R., 1988, Essential Factors in Modeling the Modulation of Impedance about the Human Elbow, Ph.D. Thesis, MIT, Dept. Mechanical Eng..

154. Hunter, I.W., and Kearney, R.E, 1983, "Generation of random sequences with jointly specified probability density and autocorrelation functions," *Biol. Cybern.*, 47, pp. 141-146.

155. Vleck, J.G., and Middleton, D., 1966, "The spectrum of clipped noise," *Proc. IEEE*, 54, pp. 2-19.

156. Narasimhan, S., Siegel, D.M., and Hollerbach, J.M., 1989, "Condor: an architecture for controlling the Utah-MIT Dextrous Hand," *IEEE Transactions on Robotics and Automation*, 5, pp. 616-627.

157. Oppenheim, A.V., Schafer, R.W., 1975, *Digital Signal Processing*, Englewood Cliffs, NJ, Prentice Hall.

158. Astrom, K.J., and Wittenmanrk, B., 1984, *Computer Controlled Systems: Theory and Design*, Englewood Cliffs, NJ, Prentice Hall.

159. Aoki, M., and Yue, P.C., 1970, "On a priori error estimates of some identification methods," *IEEE Transactions on Automatic Control*, AC-15, pp. 541-548.

160. Marquardt, D.W., and Snee, R.D., 1975, "Ridge regresssion in practice ," *American Statistician*, 29, pp. 3-20.

161. Houk, J.C., Rymer, W.Z., and Craigo, P.E., "Nature of the dynamic response and its relation to the high sensativity of muscle spindles to small changes in muscle length.," *Muscle Receptors and Movement*, edited by A. Taylor and A. Prachazka, London, Macmillam.

162. McIntyre, J., 1990, Utilizing Elastic System Properties for the Control of Movement and Posture, Ph.D. Thesis, MIT, Dept. Brain and Cognitive Sciences, June.

163. Bennett, D.J., and Hellerbach, J.M., 1988, "The role of compliance in constrained ballistic arm trajectory formation," *Society for Neuroscience Conference Abstracts*, Toronto, Canada, pp. 950.